October 2018

INCREASING ORGANIC SEMICONDUCTOR PERFORMANCE THROUGH CHEMICAL AND PROCESSING MODIFICATIONS

Edmund Burnett

INCREASING ORGANIC SEMICONDUCTOR PERFORMANCE THROUGH CHEMICAL AND PROCESSING MODIFICATIONS

A Dissertation Presented

by

EDMUND K. BURNETT

Submitted to the Graduate School of the
University of Massachusetts Amherst in partial fulfillment
of the requirements for the degree of

DOCTOR OF PHILOSOPHY

September 2018

Polymer Science & Engineering

INCREASING ORGANIC SEMICONDUCTOR PERFORMANCE THROUGH CHEMICAL AND PROCESSING MODIFICATIONS

A Dissertation Presented

by

EDMUND K. BURNETT

Approved as to style and content by:

_____
Alejandro L. Briseno, Chair

_____
Samuel P. Gido, Member

_____
Michael D. Barnes, Member

_____
E. Bryan Coughlin, Department Head
Polymer Science & Engineering

DEDICATION

To all my friends and family for helping and supporting through this journey,
and my late uncle and godfather, Peter, a true PhD at heart on a never-ending task for knowledge

ACKNOWLEDGMENTS

I would first like to thank my advisor Prof. Briseno for his help along the way and the passion that he shows for science. That passion is what drew me to this group and it is something that I hope to carry with me beyond UMass.

I would also like to thank my committee members, Prof. Gido and Prof. Barnes. I enjoyed having a wide range of strengths to poke holes or raise questions that I may not have noticed. I thank you both for that and I believe my research greatly benefited from it.

I need to thank all the Briseno group members that I have had the pleasure of working with during this journey. The old guard of Marcos, Nick, and Feng taught me the characterization tools that I would finetune during my time here. Hyunbok, Lei, and Yue showed me that success is not a given in academia, it is earned through a combination of intelligence and hard work, but hard work is a necessity for success.

To Jack and Ben, who were with me for almost the entire journey. It was a pleasure to work with you both. I do not know if any of us would have made it without the help of the others. I believe this tight group is the pinnacle of group dynamics, and I think our work and sanity greatly benefited from our friendship and collaboration.

To the new postdocs, Leo and JJ, thank you for your help and collaborative enthusiasm, it was a pleasure to work with each of you.

To my many collaborators, Prof. Mannsfeld, Prof. Amassian, Prof. Parkin, Prof. Risko, Prof. Carter, Dr. Smilgies, Prof. Schiffman, Prof. Banerji, Prof. Stingelin, Prof. Marder, Prof. Silva, and their individual students, it has been an honor to work with such brilliant scientists. In my opinion, collaboration is the best part of science, attacking large problems as a team is a true thrill, and I am proud of the team that I have been able to work with.

Many thanks to my UMass friends, especially Lauren, Stephan, and Kris. You kept me sane in times when nothing seemed to work and expanded my scientific viewpoint.

Special thanks to Sualyneth, who was an escape, a helping hand, and a partner through the later stages of this journey.

To my parents and sister, you guys started it all, allowing my curiosity to grow at an early age and giving me the support to follow through with these aspirations.

ABSTRACT

INCREASING ORGANIC SEMICONDUCTOR PERFORMANCE THROUGH CHEMICAL AND PROCESSING MODIFICATIONS

SEPTEMBER 2018

EDMUND KINGSLAND BURNETT

B.S., CLARKSON UNIVERSITY

M.Sc., UNIVERSITY OF MASSACHUSETTS AMHERST

Ph.D., UNIVERSITY OF MASSACHUSETTS AMHERST

Directed by: Professor Alejandro L. Briseno

Charge transport in organic semiconductor is greatly affected by small variations in microstructure or molecular packing. Even sub-angstrom changes to molecular packing can alter the electronic coupling and thus influence charge carrier mobilities in transistor devices. This thesis focuses on tuning molecular packing of organic semiconductors through processing or chemical modifications to increase performance and establish structure-property relationships. Chapter 2 utilizes differing processing techniques to alter the molecular packing of bistetracene in the thin film and thorough polymorph characterization to relate the modification of molecular packing to the increase in charge mobility and mechanism. Chapter 3 introduces the oligomer as a model system to resolve issues that would be difficult or impossible using polymeric systems, due to their monodispersity and increased crystallinity allows for more detailed structural characterization. In this chapter we determine a crystal packing and melting point alternation in BTTT monomers, a trend well documented within organic small molecules, yet largely ignored within the organic semiconductor community. A series of BTTT dimers with various side chains lengths were synthesized in Chapter 4 to quantify the effect of side chain length on bimolecular crystal formation with PCBM using smaller side chains, outside the solubility limit of the parent

polymer, and discovered and characterized a phase transition from a bimolecular crystal to amorphous blend upon decreasing side chain length, greatly influencing the electronic properties of the blends. Chapter 5 expands on the knowledge of the previous chapter, designing BTTT dimers with variable side chains using side chains that fall on both sides of the phase transition to investigate the influence of side chain position and size on molecular packing and blended morphology. In Chapter 6, using the benchmark BTTT dimer, we explore the effect of dopant chemical structure on morphology and conductivity of blended films. Surprisingly, the doping mechanism differs from that of the parent polymer, and by tuning the dimer/dopant interactions, demonstrate a differing morphology and large variation in conductivity dependent on dopant choice.

TABLE OF CONTENTS

Page

LIST OF TABLES

Table Page

LIST OF SCHEMES

Scheme Page

LIST OF FIGURES

Figure Page

CHAPTER 1

INTRODUCTION & BACKGROUND

1.1 Traditional Inorganic Semiconductors

Silicon-based inorganic semiconductors have ushered in an unprecedent rise in computational power since the first discovery of Si-based transistors and could be regarded as the largest technological breakthrough of the past century. Yet, despite their exponential increase in speed and power, our society has an increased appetite for the development of electronic devices that require flexibility and simplified processing techniques to tackle biomedical, energetic, and consumer problems that cannot be integrated with these brittle materials.

1.2 Organic Semiconductors

The discovery of a new class of materials, organic semiconductors, that due to conjugation, alternating single and double carbon bonds that allow the transport of charge, are a promising alternative to inorganic semiconductors. Their noncovalent nature opens the possibility to circumvent inorganics drawbacks due to their solution processability and mechanical flexibility. Organic light-emitting diodes[1] (OLEDs) have already shown commercial success and devices ranging from field-effect transistors[2-4] (FETs), solar cells[5-7], sensors[8], and radio-frequency identification tags[9] (RFIDs) demonstrating promising results utilizing organic semiconductors.

1.3 Charge Transport in Organic Semiconductors

Although the devices mentioned above have a wide variety of applications, their performance is dependent on the efficiency in which charge carriers (holes and/or electrons) move through the material.[3,10-12] In OFETs or OLEDs, charge carriers are injected into the organic semiconductor from a metal or conducting metal oxide[13,14], while in the case of organic

photovoltaics, charges are generated[15,16] within the material via photon-induced charge separation at the interface between electron-donor and electron-acceptor components and then must travel to respective contacts.[17,18] The key quantity that characterizes charge transport is carrier mobility. In the absence of any external potential, transport is purely diffusive and is generally described with a simple diffusion equation:

$$< x^2 > = nDt \tag{1}$$

where $<x^2>$ denotes the mean-square displacement of the charges, D is the diffusion coefficient, t is the time, and n represents an integer number equal to 2, 4, or 6 for one-, two-, and three-dimensional systems. In the case of hopping transport between neighboring molecules the charge mobility μ is related to the diffusion coefficient via the Einstein-Smoluchowski equation:

$$\mu = \frac{eD}{k_B T} \tag{2}$$

where k_B is the Boltzmann constant and e is the electron charge. For a 1D system, $D = a^2 k_{ET}$, where *a* is defined as the molecular spacing and k_{ET} represents the hopping rate between sites. According to the small polaron theory[19,20], the hopping rate follows an Arrhenius type equation and can be expressed as:

$$k_{ET} = \frac{t^2}{\hbar}\left[\frac{\pi}{2E_{pol}k_B T}\right]^{1/2} exp\left(\frac{-E_{pol}}{2k_B T}\right) \tag{3}$$

where *t* is the charge transfer integral and E_{pol} the polaron binding energy. This hopping rate is identical to Marcus theory's equation for electron transfer rate[21] when substituting reorganization energy $\lambda_{reorg}/2$ for polaron binding energy. From the substitution of the hopping rate into the diffusion equation, we can express the hopping mobility:

$$\mu_{hop} = \frac{ea^2 t^2}{k_B T \hbar}\left[\frac{\pi}{2E_{pol}k_B T}\right]^{1/2} exp\left(\frac{-E_{pol}}{2k_B T}\right) \tag{4}$$

Demonstrating the two major variables effecting charge carrier mobility. The transfer integral (*t*) and reorganization energy (λ_{reorg}), the former defining the electronic coupling between adjacent

molecules and the latter summarizing the changes in molecular geometry during charge transfer.[11] Thus, to increase charge carrier mobility, the transfer integral must be maximized, and reorganization energy minimized, or the electronic coupling between molecules must be increased without molecular geometric modifications during charge transport.

The application of an external field induces a drift of the charge carriers; the mobility can then be alternatively defined as the ratio between velocity, v, of the charges and the amplitude of the applied electronic field, F:

$$\mu = v/F \tag{5}$$

and is usually expressed in $cm^2/V{\cdot}s$.

In metals and inorganic semiconductors, charge transport occurs in delocalized states, and is limited by the scattering of the carriers, mainly on phonons, which are thermally induced lattice deformations.[4] This model of transport is not fully applicable to organic semiconductors, yet signatures of this transport method have been demonstrated in ultrapure organic single crystal materials.[22-24] Transport usually occurs by the hopping of charges between localized states. In a localized transport it is no longer hindered by phonon scattering, but assisted.[25,26] Charge mobility decreases with temperature in conventional semiconductors, yet with classical organic semiconductors, mobility increases with temperature. A comparison of the temperature-dependent mobility of each mechanism is shown in **Figure 1**. In state-of-the-art organic semiconductor materials, with mobilities now on par with amorphous Si, there is controversy to describe the conductivity within the materials as localized or delocalized transport with signatures of both methods simultaneously present.[27,28]

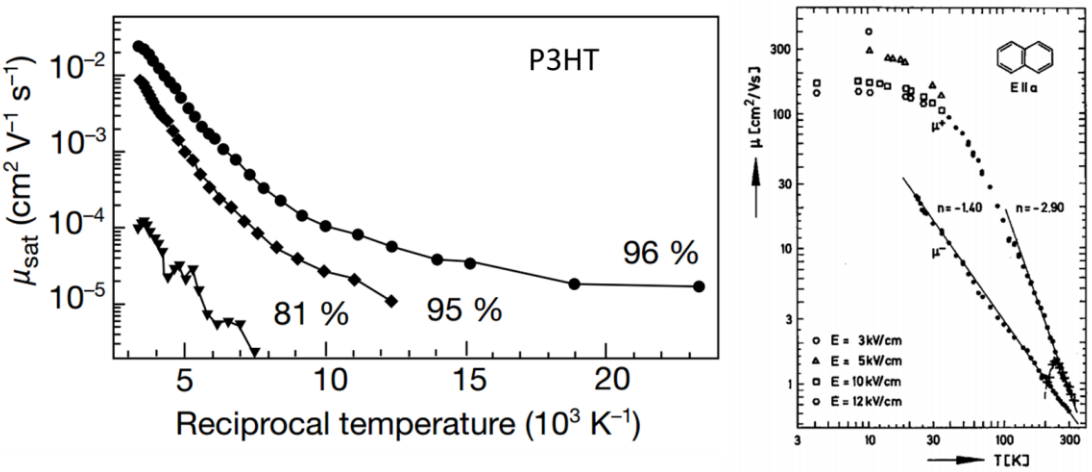

Figure 1 Temperature-dependent mobility of (a) P3HT as a function of regioregularity representing the hopping mechanism of charge transport, and (b) single crystals of naphthalene demonstrating the mobility behavior of band transport. Reprinted from ref. 25 and 22.

1.4 Molecular Packing in Organic Semiconductors

Quantum-chemical calculations have allowed a deeper understanding of the relationship between molecular packing and charge transport.[29] A seminal work by Bredas et al. used simulation of two cofacial dimers of sexithiophene to examine the effect of intermolecular separation and coplanar displacement on charge transport (**Figure 2**).[10] By tracking the HOMO and LUMO level splitting as a function of intermolecular distance, an exponential decay in splitting was observed as the intermolecular distance was increased. The intermolecular distance was then fixed between the sexithiophene molecules and laterally displaced while simulating the HOMO/LUMO splitting. This experiment showed large oscillations in splitting. These results highlight the sensitivity of the transfer integral and thus charge carrier mobility to variation in molecular packing, with a large amount of research have investigated decreasing the

pi-pi stacking distance to maximize the transfer integral.

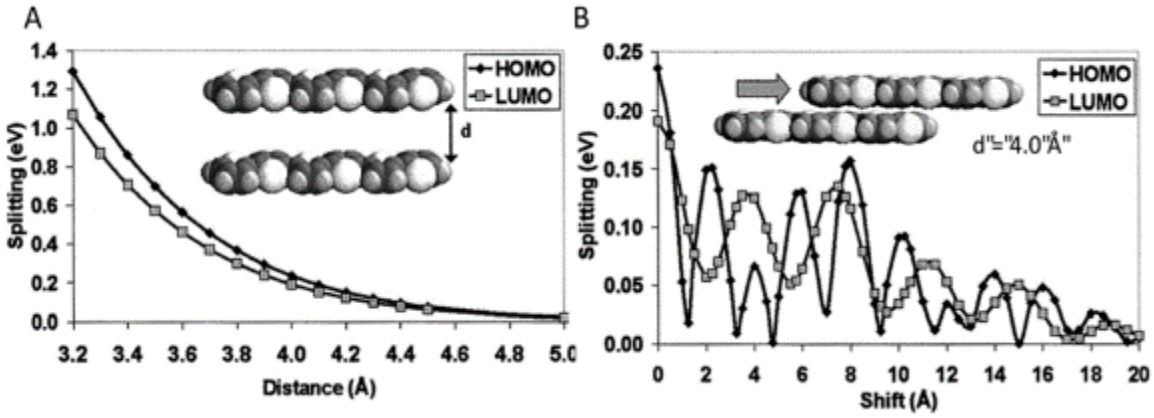

Figure 2 Quantum chemical investigation on energy level splitting and sexithiophene molecular displacements. (a) HOMO and LUMO electronic splitting as a function of intermolecular distance. (b) HOMO and LUMO electronic splitting with fixed intermolecular distance of 4 Å as a function of the horizontal shift of the top molecule along the long molecular axis. Adopted from ref. 10.

1.5 Organic Field Effect Transistors

Field-effect transistors (FETs) represent the logical component within integrated circuits that govern all modern electronic devices.[30] FETs are also used as the main experimental tool for the extraction of charge-carrier mobilities of semiconducting materials. A schematic diagram is shown in **Figure 3**.

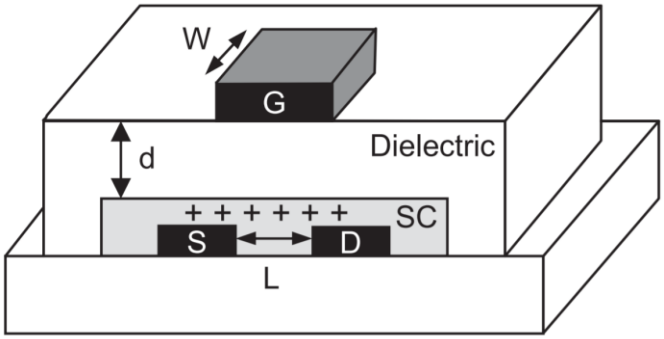

Figure 3 Schematic diagram of a standard OFET device architecture. Reprint from ref. 3.

Transistors consist of three electrodes: the gate (G), source (S) and drain (D). The active semiconductor material connects the source-drain, and a dielectric layer insulates the gate electrode from other device components. When a voltage is applied to the gate (V_G), charge-carriers are induced at the dielectric-semiconductor interface[31], creating a conducting channel. By applying a bias to the drain electrode, a current across the source and drain is generated. The distance between the source and drain is referred to as the channel length (L), while the electrode width is known as the channel width (W). Charge transport in field-effect transistors occurs at the surface of the semiconductor film, flowing from the source to drain electrodes upon the application of a voltage (V_{SD}). Upon small voltage application in which V_{SD} is much lower than V_G, the current increases linearly with V_{SD} and the relation between current (I_{SD}) and voltage can be expressed as:

$$I_{SD} = \frac{W}{L}\mu C(V_G - V_T)V_{SD} \quad (6)$$

where C is the gate dielectric capacitance and V_T is defined as the threshold voltage. Further increase in V_{SD} to values equal or greater to V_G results in the saturation regime in which current/voltage relationship is:

$$I_{SD} = \frac{W}{2L}\mu C(V_G - V_T)^2 \quad (7)$$

1.6 Doping of Organic Semiconductors

The doping of organic semiconductors initially attempted to mimic that of doping inorganic semiconductors[32,33] in which impurity atoms are introduced into the lattice, resulting in large conductivity increases at ultralow doping ratios, as typically every covalent bound dopant atom donates one mobile charge to the highly crystalline and ultra-pure semiconductor matrix. Early organic semiconductors doping experiments used strongly oxidizing gases, iodine or bromine[34], or small atoms like lithium or cesium.[35,36] These dopants were very effective at

increasing conductivity, but due to their small size and lack of covalent bonds, they would readily diffuse, limiting their device application.

Molecular dopants have now been used instead, which employ strong molecular acceptors for p-type doping and donors for n-type doping.[37-40] These dopants are designed such that, for p-type doping, their electron affinity (EA) is in the range of the ionization energy (IE) of the semiconductor and conversely for n-type doping. Inorganic semiconductor doping physics were adopted and the mechanism of doping organic semiconductors involved an integer charge transfer from the highest occupied molecular orbital (HOMO) of the organic semiconductor to the lowest unoccupied molecular orbital (LUMO) of the p-dopant and this was experimental demonstrated for numerous materials.[41-46] This process leads to a localized charge on the dopant and a mobile hole within the semiconductor (**Figure 4**). The energetic offset was thought to be the limiting factor to reach high conductivities, as was demonstrated in one of the first solution processable doping studies that used a set of polymers with various HOMO energy levels and blended with F4TCNQ and found that lower IP polymers were easier to dope and reached higher conductivity values.[47] This led to dopant design revolving around increasing the EA as high as possible to increase doping efficiency.

Yet, a differing model has been proposed and experimentally verified for certain organic semiconductor/dopant blends, more prevalent in systems using small molecule organic semiconductors. In these arrangements, a frontier molecular orbital hybridization between the organic semiconductor HOMO and the dopant LUMO has been suggested, leading to the formation of a ground-state charge-transfer complex (**Figure 4**).[48-52]

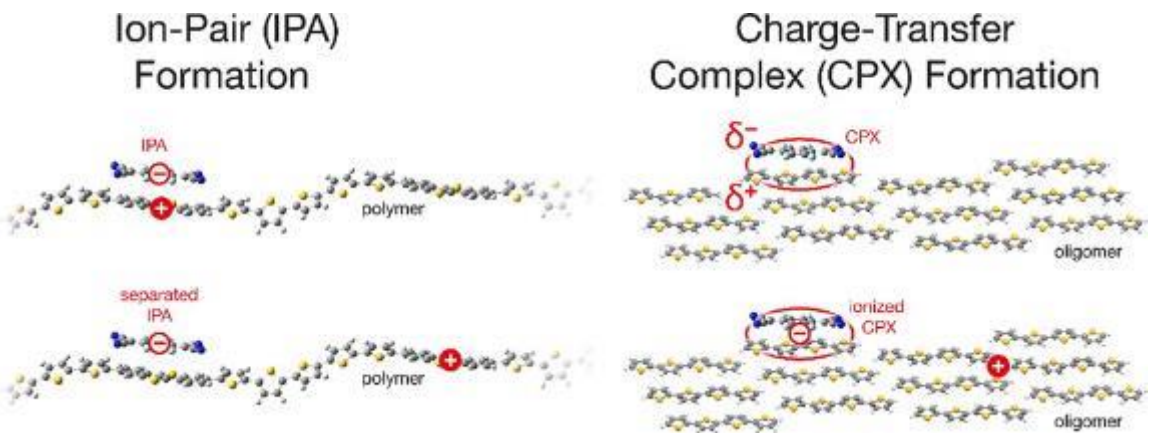

Figure 4 Cartoon representation of differing mechanisms of molecular doping organic semiconductors. Reprint from ref. 39.

To date, there is not a detailed understanding of what dictates which mechanism, yet no system has demonstrated signatures of both mechanisms, and outside of an unpublished, metastable system using P3HT/F4CTNQ, processing variation has not influenced the mechanism. A seminal study comparing P3HT to its small molecule analog demonstrated the effect of each mechanism on various doping characterization techniques, with a large difference in conductivity behavior as a function of F4TCNQ loading is presented in **Figure 5**.

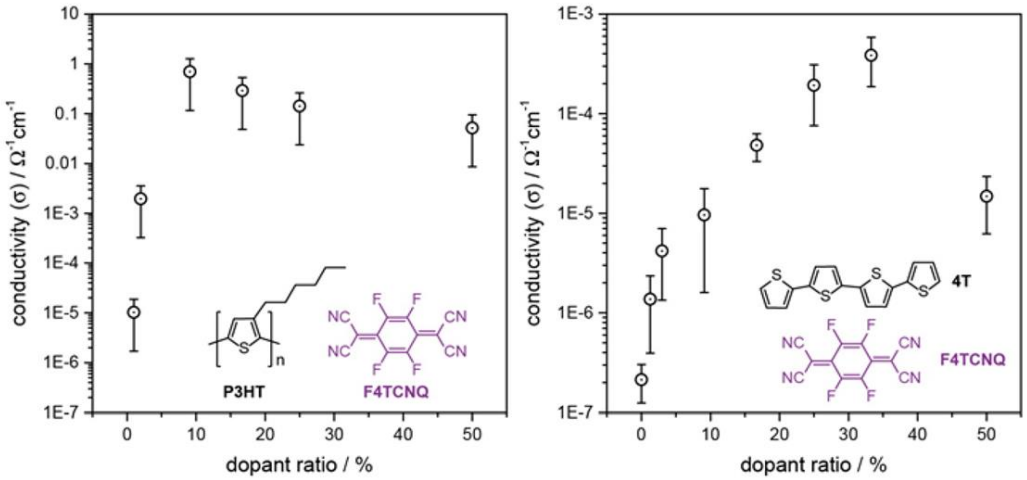

Figure 5 Sheet conductivities (σ) of poly(3-hexylthiophene) (P3HT) and quaterthiophene (4T) thin films upon p-doping with the strong electron acceptor 7,7,8,8-tetracyano-2,3,5,6-tetrafluoroquinodimethane (F4TCNQ); dopant ratio refers to the number of dopant molecules divided by the sum of monomer units and dopant molecules (P3HT) or divided by total number of all molecules (4T). Reprint from ref. 49.

With the use of the benchmark, molecular p-dopant, F4TCNQ, identification of the dopant mechanism predominately relies on UV-Vis-NIR and FTIR measurements. **Figure 6** highlights the mechanism-dependent feature differences for each characterization technique. UV-Vis-NIR can be used upon dopant introduction to track the formation of new absorption features and their relationship to each doping mechanism.[39,48,49] As ion-pair formation will give rise to previously characterized F4TCNQ anion peaks and semiconductor polaron peaks, while a charge-transfer complex will not show these peaks and instead give rise to a broad peak in the NIR associated with the absorption of the hybrid complex. FTIR specta of neat and doped films can monitor the shift in the cyano vibration of the F4TCNQ to quantify the degree of charge transfer.[53,54]

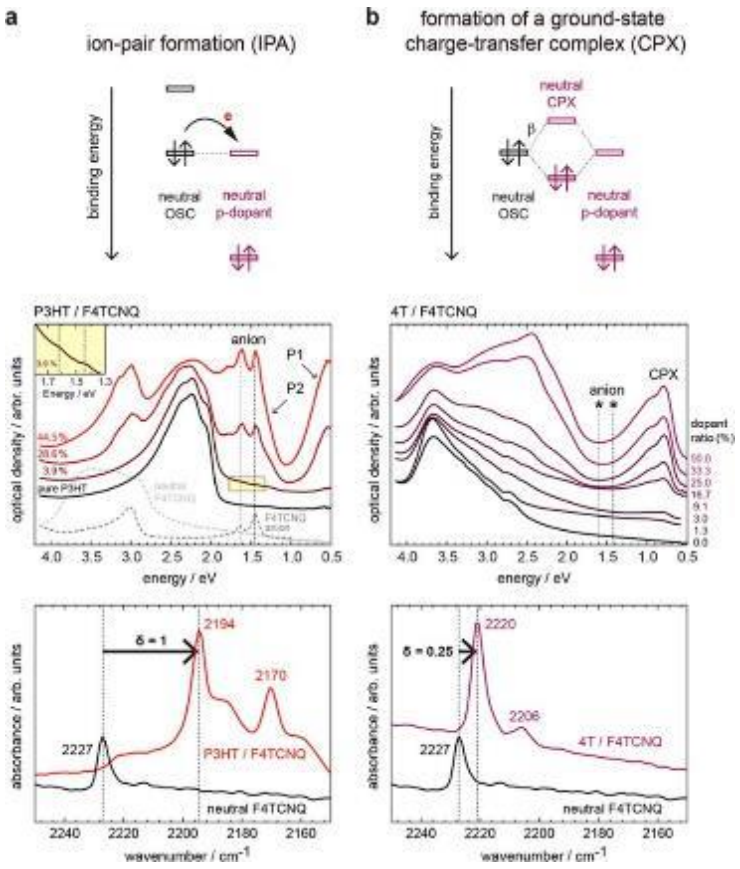

Figure 6 (top) (a) Ion-pair formation (IPA) and (b) the formation of a ground-state charge transfer complex (CPX). (middle) Spectral signatures of IPA and CPX in UV/vis/NIR for (a) P3HT/F4TCNQ and (b) 4T/F4TCNQ; P1 and P2 denote transitions of the positive polaron in P3HT. (bottom) Spectral signatures of IPA and CPX in FTIR for (a) P3HT/F4TCNQ and (b) 4T/F4TCNQ; charge transfer δ is deduced from the shifts of the cyano vibrations.

1.7 Thesis Organization

This thesis focuses on tuning molecular packing of organic semiconductors through processing or chemical modifications to increase performance and establish structure-property relationships. Chapter 2 utilizes differing processing techniques to alter the molecular packing of bistetracene in the thin film and thorough polymorph characterization to relate the modification of molecular packing to the increase in charge mobility and mechanism with results coming from publication in Advanced Materials Interfaces (Burnett, E. K.; Ly, J.; Niazi, M. R.; Zhang, L.; McCuskey, S. R.; Amassian, A.; Smilgies, D. M.; Mannsfeld, S. C. B.; Briseno, A. L. Bistetracene Thin

Film Polymorphic Control to Unravel the Effect of Molecular Packing on Charge Transport. *Adv. Mater. Interfaces* **2018,** 1701607).[55] Chapter 3 introduces the oligomer as a model system to resolve issues that would be difficult or impossible using polymeric systems, due to their monodispersity and increased crystallinity allows for more detailed structural characterization. In this chapter we determine a crystal packing and melting point alternation in BTTT monomers, a trend well documented within organic small molecules, yet largely ignored within the organic semiconductor community. A series of BTTT dimers with various side chains lengths were synthesized in Chapter 4 to quantify the effect of side chain length on bimolecular crystal formation with PCBM using smaller side chains, outside the solubility limit of the parent polymer, and discovered and characterized a phase transition from a bimolecular crystal to amorphous blend upon decreasing side chain length, greatly influencing the electronic properties of the blends, with results coming my publication in Chemistry of Materials (Burnett, E. K.; Cherniawski, B.; Rosa, S. J.; Smilgies, D. M.; Parkin, S.; Briseno, A. L. Breaking the Bimolecular Crystal: The Effect of Side Chain Length on Oligothiophene/Fullerene Intercalation. *Chem. Mater.* **2018**, In Press).[56] Chapter 5 expands on the knowledge of the previous chapter, designing BTTT dimers with variable side chains using side chains that fall on both sides of the phase transition to investigate the influence of side chain position and size on molecular packing and blended morphology. In Chapter 6, using the benchmark BTTT dimer, we explore the effect of dopant chemical structure on morphology and conductivity of blended films. Surprisingly, the doping mechanism differs from that of the parent polymer, and by tuning the dimer/dopant interactions, demonstrate a differing morphology and large variation in conductivity dependent on dopant choice.

CHAPTER 2

POLYMORPHIC CONTROL OF BISTETRACENE THIN FILMS

2.1 Introduction

Charge transport in organic semiconductor thin films is greatly affected by small variations in microstructure or molecular packing.[12,57] Even sub-angstrom changes to molecular packing can alter the electronic coupling and thus influence charge carrier mobilities in transistor devices.[11,58,59] Tuning the molecular packing is normally done through chemical modifications.[60] This is apparent in pentacene and its functionalized derivatives (**Figure 7**).[61] Pentacene arranges in an edge-to-face herringbone manner. Yet, when functionalized with TIPS groups at the 6, 13 positions, the material adopts a face-to-face "brick-like" motif, and if the position of the TIPS substitution is slightly varied to 5, 14 positions, the material arranges in a sandwich herringbone.

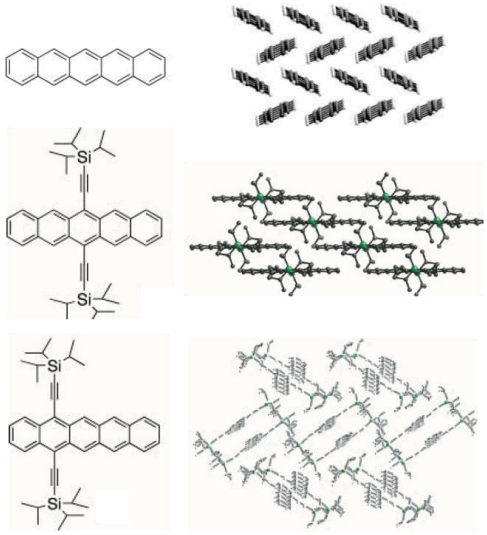

Figure 7 Demonstrating the effect of chemical modification on molecular packing with pentacene (top) arranges in an edge-to-face herringbone manner. Functionalized with TIPS groups at the 6, 13 positions (middle), the material adopts a face-to-face "brick-like" motif, and if the position of the TIPS substitution is slightly varied to 5, 14 positions (bottom), the material arranges in a sandwich herringbone. Adopted from ref. 59.

These chemical changes can also affect the optoelectronic and physical properties of the material, making fundamental structure-property relations more difficult to quantify and correlate.

Alternatively, adjusting processing conditions provides another approach to altering molecular packing.[62-68] Specific to small molecule systems, processing can be used to access certain thin film polymorphs.[69-71] Polymorphism, the ability for the same compound to adopt different crystalline packing states, is prevalent in organic semiconductors as the dominant interactions are van der Waals and weak electrostatic interactions.[29] Thus, the fine-tuning of crystal packing and isolation of high mobility polymorphs may be realized through a variety of processing techniques, such as blade or shear coating, thermal annealing, or solvent vapor annealing.[69,70,72[16-18]] For example, pentacene has four polymorphs, yet only accessible in thin films through careful control of film thickness, substrate choice, and substrate temperature during deposition.[67,73-75] TIPS-pentacene exhibits metastable polymorphs (**Figure 8**), but only accessible using a specialized micropillared-blade solution shearing deposition method.[62]

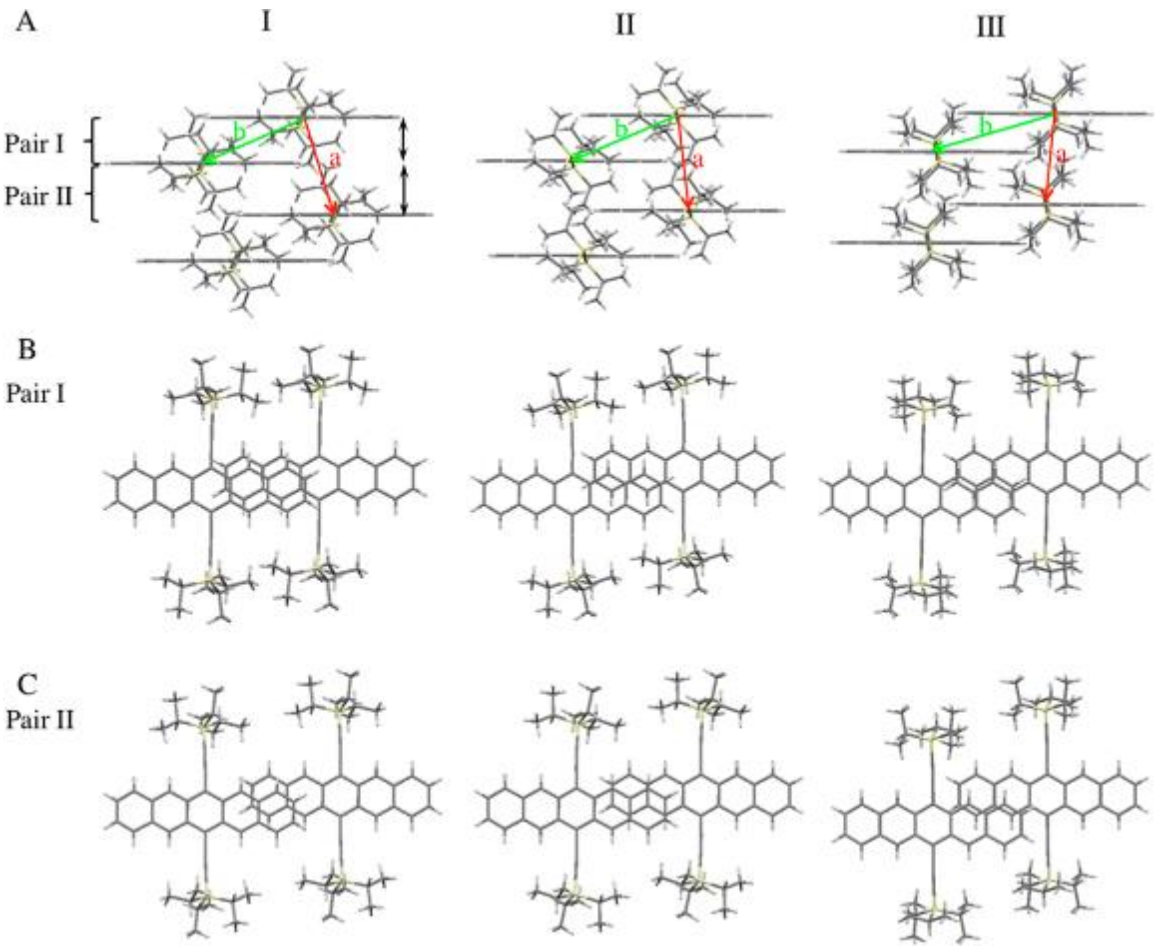

Figure 8 Comparison of the three major polymorphs of TIPS-pentacene in their π–π stacking (A) and molecular offset along the conjugated backbone (B,C) as obtained from the crystallographic refinement calculations. Reprint from ref. 66.

Other polymorphic work, **Figure 9**, focused on utilizing simplified post-deposition processing techniques and demonstrated the ability to access three different polymorphs of contorted hexabenzocoronone[70] without substrate, deposition, or film thickness modification. Expansion of this work using an NDI derivative to look into the stability/reversibility of these thin film polymorphs and confirmed through solvent and thermal annealing cycling the reversibility of this polymorph access.[69]

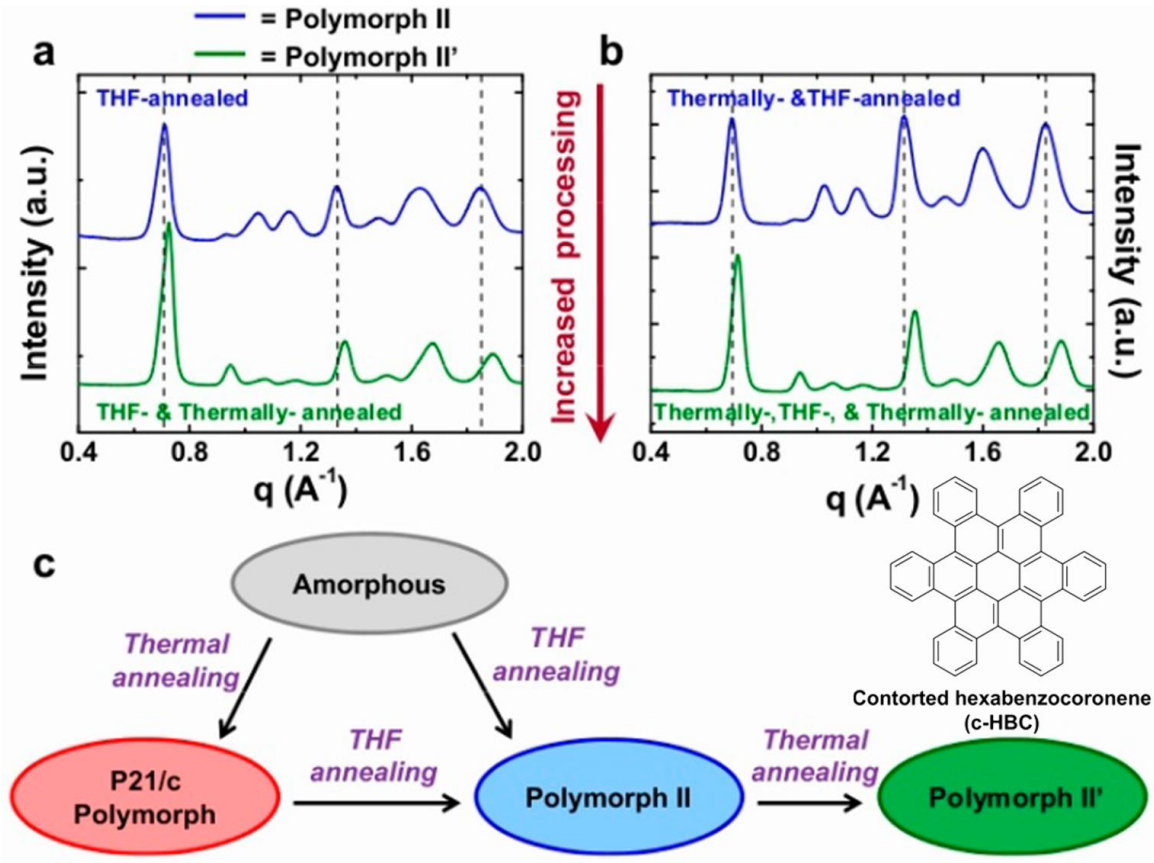

Figure 9. "Powder" diffraction patterns generated from azimuthally integrating 2D-GIXD images of c-HBC films that were first either (a) THF-annealed or (b) thermally annealed and then THF-annealed, resulting in the films adopting polymorph II (blue traces). Subjecting each of these films to an additional thermal annealing step results in their transformation to polymorph II' (green traces). The dashed vertical lines are provided as a guide for the eye to better discern differences between polymorph II and II'. (c) A schematic summarizing the processing techniques applied and crystal structures accessed as a result. Reprint from ref. 68.

Furthermore, polymorphism provides an excellent platform in organic semiconductors for examining the fundamental relationship between charge transport and molecular packing as the molecular packing can be varied without the need for chemical modification.[68,72]

Yet, these high performance acenes suffer from instability due to their reactivity with light and oxygen. This can be improved by modifying the acene molecular arrangement from the common linear array to an angular analogue.[76,77] The increased stability can be attributed to the increase of benzenoid sextets, which increase the overall aromatic stabilization energy, as these

compounds have at least two sextets in comparison to the linear analogues, which can only possess one sextet. Our group synthesized a solution processable, acene derivative with two fused tetracene cores and either TIPS or N-octyldiisopropylsilyl acetylene (NODIPSA) side chains for solubility.[78] Exploration of the material in the single crystal form revealed that the NODIPSA-bistetracene (BT) had a very high mobility (6.1 cm^2/Vs) due to its 2D pi-pi stacking arrangement, and device-stability over months in air. Yet, these stable acene derivatives are much larger molecules then the benchmark TIPS-pentacene, and call for even bulkier side chains for solubility. When the NODIPSA group was attached to a pentacene core, the material exhibited no field effect. Thus, understanding how these larger stable polycyclic aromatic hydrocarbons assemble in the thin film and the processing techniques necessary for achieving high mobility is paramount for the further development and implementation of this class of materials. In this study, we report a new "thin film" polymorph of BT accessed via spin coating. Solvent vapor annealing[79-81] transforms this polymorph to the "bulk" triclinic crystal packing of BT (chemical structure is shown in **Figure 10a**), also observed in single crystals and responsible for the excellent charge carrier mobility in single crystal transistors, thanks to the 2D “brick-layer” molecular packing.[78] Static and *in-situ* grazing-incidence X-ray diffraction (GIXD) are employed to track the molecular changes within the BT films during exposure to solvent vapors, and through a combination of simulation and crystallographic refinement calculation, we estimate the molecular packing of the thin film polymorph to adopt a slipped 1D π-stacking motif. Organic thin film transistors prepared after solvent vapor annealing result in a remarkable three orders of magnitude increase in carrier mobility. We investigate the transport anisotropy as well as the temperature-dependent mobility. We find the thermally activated transport behavior gives way to one where carrier mobility increases upon decreasing the temperature after phase transformation.

2.2 Experimental

N-octyldiisoproplsilyl acetylene bistetracene (BT) was synthesized according to literature.[78] All solvents were purchased from Sigma Aldrich and used as received.

Thin films for structural analysis as well as electronic characterization were fabricated by dissolving BT in chloroform (10 mg/ml) followed by spin coating at 2000 rpm for 60 seconds. Solvent annealed samples were placed in a petri dish with a well of 500 µl of chlorobenzene and allowed to crystallize for 8 hours.

Differential scanning calorimetry (DSC) measurements were conducted under N_2 atmosphere at a scan rate of 10˚C/min. Standard aluminum crucibles were used. Thin film sample was prepared by drop-casting chloroform BT solution directly into crucible. Solvent-annealed sample was prepared by exposing sample after drop-casting solution to chlorobenzene vapors for eight hours. The sample weight was 4 mg.

In-situ grazing incidence wide-angle x-ray scattering (GIWAXS) measurements were carried out at D-line (Cornell High Energy Synchrotron Source). A 0.5 × 0.1 mm beam with a wavelength of 1.23 Å and wide band pass (1.47%) was generated from double-bounce multilayer monochromator. The incidence angle was 0.15° with respect to the substrate plane. During X-ray scattering experiments samples were kept in a chamber with vapor pressure control and Kapton windows to allow X-ray scattering through the chamber: liquid solvent was injected into a reservoir at the bottom of the cell. Scattering x-ray photons were detected with a Pilatus 200k pixel array detector (Dectris). Additional GIWAXS experiment were carried out at Stanford Synchrotron Radiation Lightsource (SSRL) on beamline 11-3 (two-dimensional scattering with an area detector, MAR345 image plate, at grazing incidence). The incident energy was 12.7 keV.

Device Fabrication and Characterization: Bottom-contact, bottom gate devices were fabricated using Si wafers with thermally grown SiO2 (300 nm thick) were used as the gate and

dielectric, respectively, prepatterned with 50 nm Au bottom contacts with a 5 nm Ti adhesion layer. Device channel dimensions of 300 μm and 50 μm for the width and length, respectively, were used. The substrates were sonicated in deionized water and soap, acetone, isopropanol, and deionized water and dried with nitrogen. Substrates were then exposed to UV-ozone treatment for 15 minutes. Electrical device characterization at room temperature was carried out under ambient conditions. Mobility was evaluated in the saturation regime, at a drain voltage Vd = -60 V. Low temperature measurements were carried out under vacuum, at temperatures ranging from 100 to 300 K.

2.3 Results and Discussion

Figure 10b shows a polarized optical image of a spin-coated film of BT from chloroform on a silicon wafer that exibits little to no birefringence. Upon exposure to chlorobenzene vapors in a closed petri dish, large crystalline domains grow on the order of millimeters from the edge of the substrate and grow inward, indicating nucleation and growth from the thicker edges[82] (**Figure 10c**). Grazing-incidence X-ray diffraction (GIXD) measurements were performed on the BT film before and after chlorobenzene vapor exposure to help assess the microstructural changes induced by solvent vapor annealing (SVA). The diffraction pattern of the spin-coated BT film is shown in **Figure 10d**, and despite the absence of birefringence in the optical micrographs, the

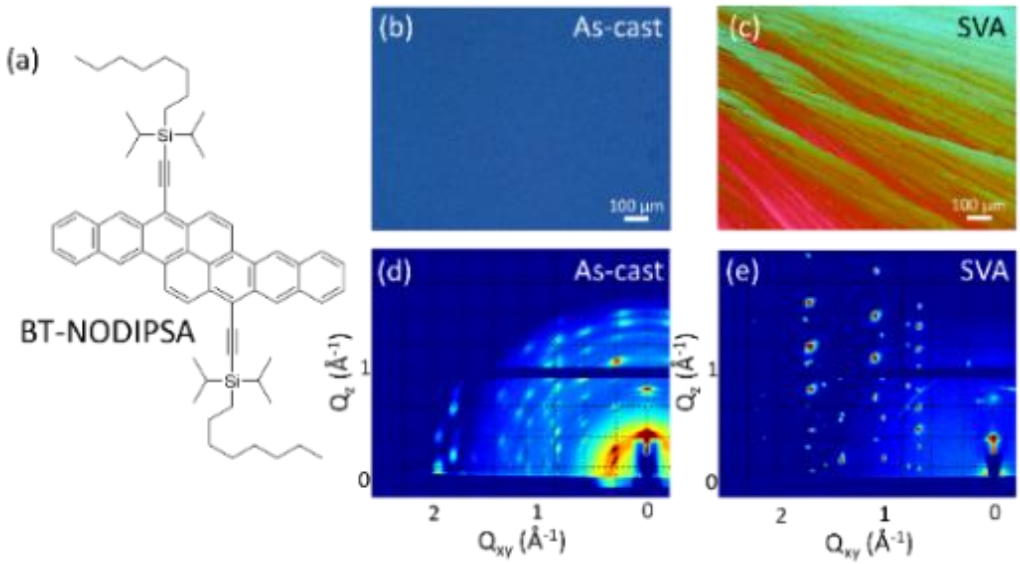

Figure 10 a) Chemical structure of BT, (b) optical image of a spin-coated film of BT, and (c) polarized optical image of BT film after solvent vapor annealing. (d) 2D-GIXD patterns of the as-cast BT and (e) SVA films.

film appears to be highly crystalline and has the characteristics of a 2D powder, where grains are highly oriented out-of-plane, yet randomly oriented in the plane of the film. These diffraction peaks show slight arcing, indicative of an imperfect 2D powder, with the film having some mosaicity. From the measurement of the diffraction peak position, the unit cell parameters were extracted using a least-square fitting procedure (**Table 1)**.[74,83] The triclinic unit cell of as-cast BT—a=22.80 Å, b=8.03 Å, c=18.24 Å, α=95.6°, β=119.9°, γ= 78.8°—did not match to that of the bulk single crystal, indicating that the film exhibits a new substrate-induced polymorph. These as-cast films even show evidence of additional, competing polymorphs present, with multiple sharp reflections along the q_z axis at q_{xy} ~ 0. However, the number of peak positions that could be extracted was not sufficient to index these additional structures.

Table 1 Lattice constants of as-cast and solvent annealed unit cells with bulk crystal structure included for reference.

Processing Condition	a (Å)	b (Å)	c (Å)	α (˚)	β (˚)	γ (˚)
As-cast	22.80	8.03	18.20	95.6˚	119.9˚	78.8˚
Solvent annealed	11.76	12.89	18.75	97.6˚	106.4˚	95.7˚
Bulk single crystal	11.76	12.89	18.75	97.6˚	106.4˚	95.7˚

In order to estimate the molecular packing in the as-cast BT polymorph, crystallographic refinement calculations were performed in which the theoretical X-ray scattering intensities from a test molecular arrangement are fitted to the observed intensities and the best-fit molecular packing is obtained by a Monte Carlo optimization of the fitting error. This procedure has been detailed previously.[74,83] Usually this fitting procedure fixes the molecular structure to a known conformation such as an available bulk molecular structure and only optimizes the positions and Euler angles of the molecules since there are typically not enough intensity data points to fit atomic positions as in single crystal X-ray refinement. However, in the present some conformational flexibility of the BT molecule was introduced by allowing a rotation of the N-octyldiisopropylsilyl acetylene side chains about the triple-bond, similar to what was previously done for TIPS-pentacene.[68] The obtained thin film packing exhibits a slipped one-dimensional (1D) π-stacking motif with a herringbone arrangement of adjacent stacks.

The goodness of the fit is graphically shown in **Figure 11**, where the degree of matching between calculated and measured scattering intensities is shown by pairs of half-circles. While the fit is quite satisfactory and the obtained packing of the BT cores plausible, the extremely conformationally flexible, large side chains are not well represented by this modeling and the obtained packing should thus be considered the best possible approximation of the molecular packing.

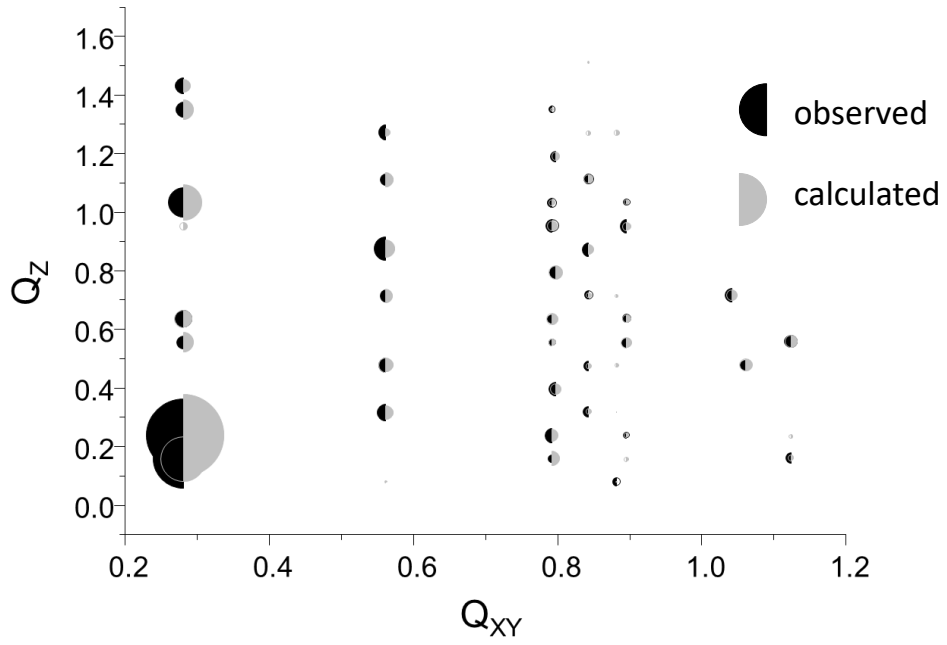

Figure 11 The measured and calculated diffraction intensities (best-fit) for the spin coated BT film.

The diffraction pattern after solvent vapor annealing shows a large change in molecular packing, as shown in **Figure 1e**. Using the same least-square-error fitting procedure, the lattice constants were extracted and representative of the bulk single crystal, with the (001) plane normal to the substrate, indicating that BT is packing in an edge-on arrangement. The molecular packing arranges into a 2D brick-like π-stacking motif with close intrastack distances of 3.35 Å. The stacks are characterized by two alternating intermolecular center-to-center distances of 8.59 Å and 8.01 Å between adjacent molecules due to the presence of two translationally inequivalent molecules. The molecular packing of the as-cast and solvent annealed films are shown in **Figure 12**.

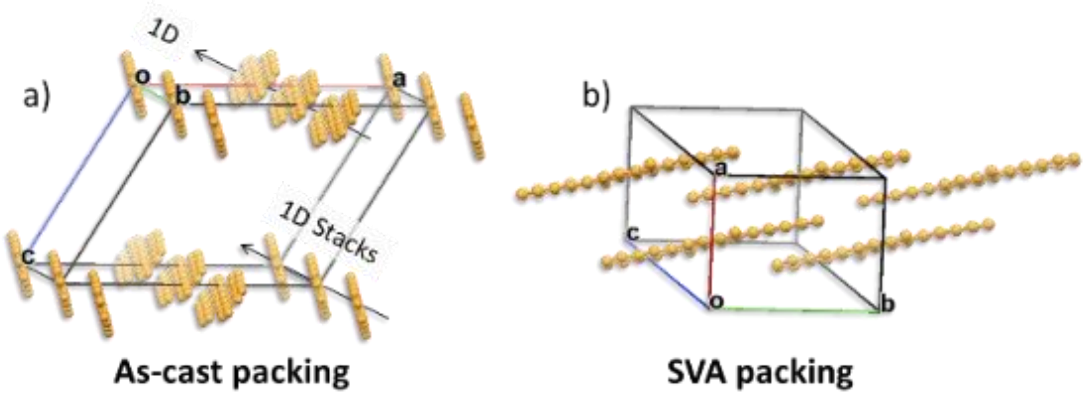

Figure 12 Crystal structure and molecular packing of (a) as-cast BT polymorph. The 1D pi-stacks crystallize along the b-axis (010). (b) The solvent vapor annealed BT molecular packing is identical to the bulk crystal structure (2D brick layer motif). Note: the silylethynyl solubilizing groups have been removed for clarity.

To further understand the morphological changes that occur during vapor exposure, *in-situ* solvent vapor annealing GIXD measurements were carried out.[84] A spin-coated film of BT, GIXD image shown in **Figure 13a**, was exposed to chlorobenzene vapors and the the diffraction patterns were recorded over time. After 30 minutes, **Figure 13b**, pronounced changes in the diffraction pattern could be observed, as the reflection at q_z = 0.31 $Å^{-1}$ and others representative of the competing polymorph that could not be indexed are no longer present, and only the peaks corresponding to the fitted thin film unit cell appear. The reflections also showed less mosaicity, indicating that the crystalline grains are more ordered. At 60 minutes of exposure, **Figure 13c**, new scattering features began to appear with a distinct Bragg rod forming centered at q_{xy} = 0.72 $Å^{-1}$ corresponding to the bulk BT solvent annealed film. After 300 minutes of solvent annealing, **Figure 13d**, the diffraction pattern was representative of the bulk triclinic crystal structure and resembled the static solvent annealed BT pattern, with no peaks present corresponding to the as-cast BT diffraction pattern.

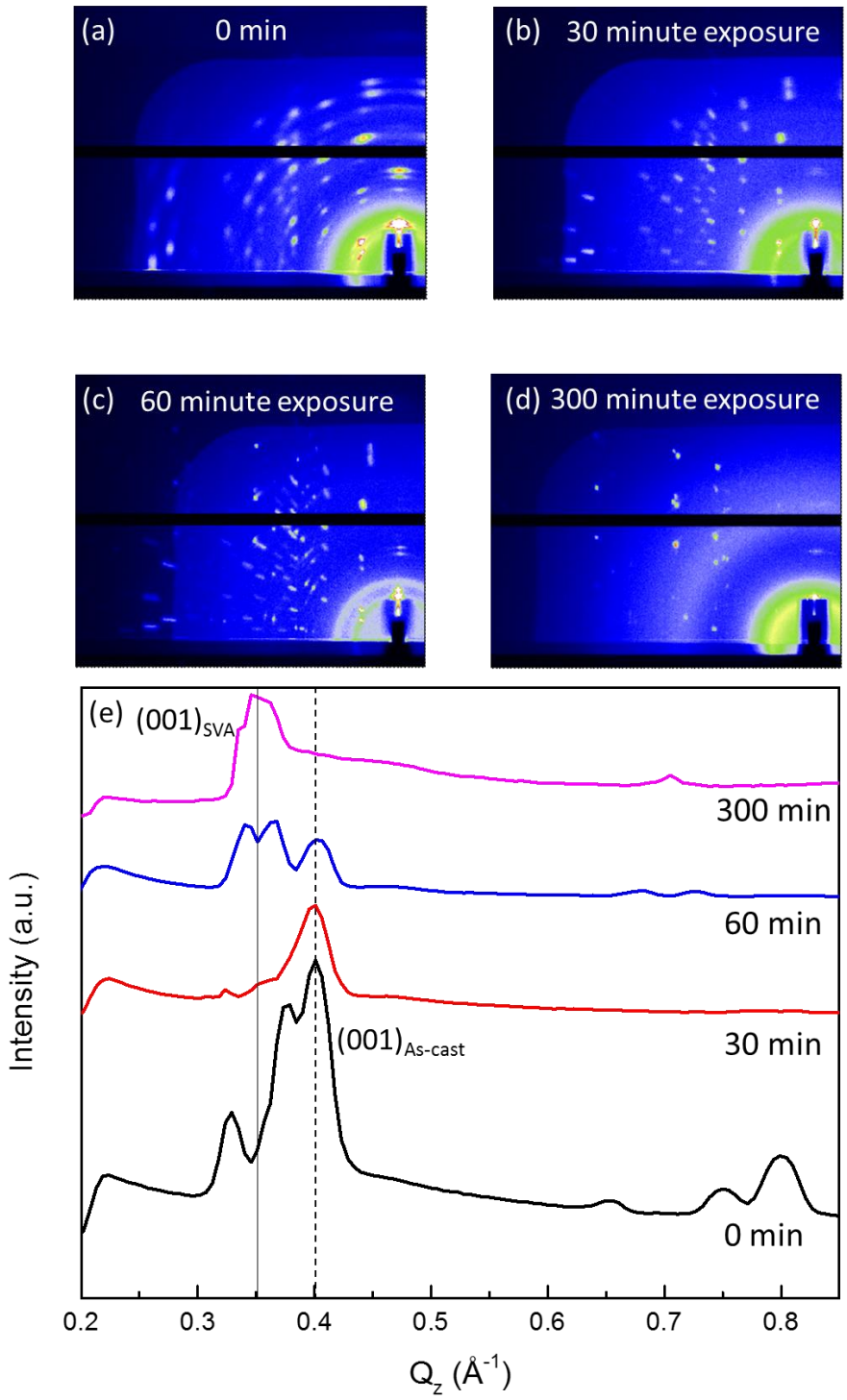

Figure 13 *In-situ* GIXD patterns of (a) spin-coated BT film before exposure to chlorobenzene vapors. (b) Film after 30 minutes, (c) 60 minutes, and (d) 300 minutes of SVA. (e) Out-of-plane intensity plots with lines to guide the eye along the major diffraction peak of the as cast (dashed) and static solvent annealed films (solid).

Differential scanning calorimetry (DSC) was used to quantify how molecular packing and processing conditions effected the material's thermal properties. We compare BT single crystal, as-cast, and SVA samples as shown in **Figure 14**. Single crystals were fabricated by slow evaporation from hexane solution.[78] The as-cast and SVA samples are prepared by drop-casting chloroform solution directly into the DSC sample pan (as-cast) followed by exposure to chlorobenzene vapors (SVA) for eight hours. The single crystal (black) shows one sharp endothermic melting transition at 142˚C during the first heating. Cooling from the melt, the single crystal sample exhibits no recrystallization exotherm. Only upon the second heating did we observe a 'cold-crystallization'[85-87] exotherm above 57˚C followed by a single sharp melting transition at 110˚C. The as-cast sample (blue) demonstrates a single melting endotherm at 106˚C in both the first and second heating ramps and a recrystallization peak at 57˚C during cooling. Finally, the SVA sample shows behavior similar to single crystal with a large melting endotherm at 138˚C during the first heating, recrystallization onset at 57˚C followed by a single melting endotherm at 107˚C.

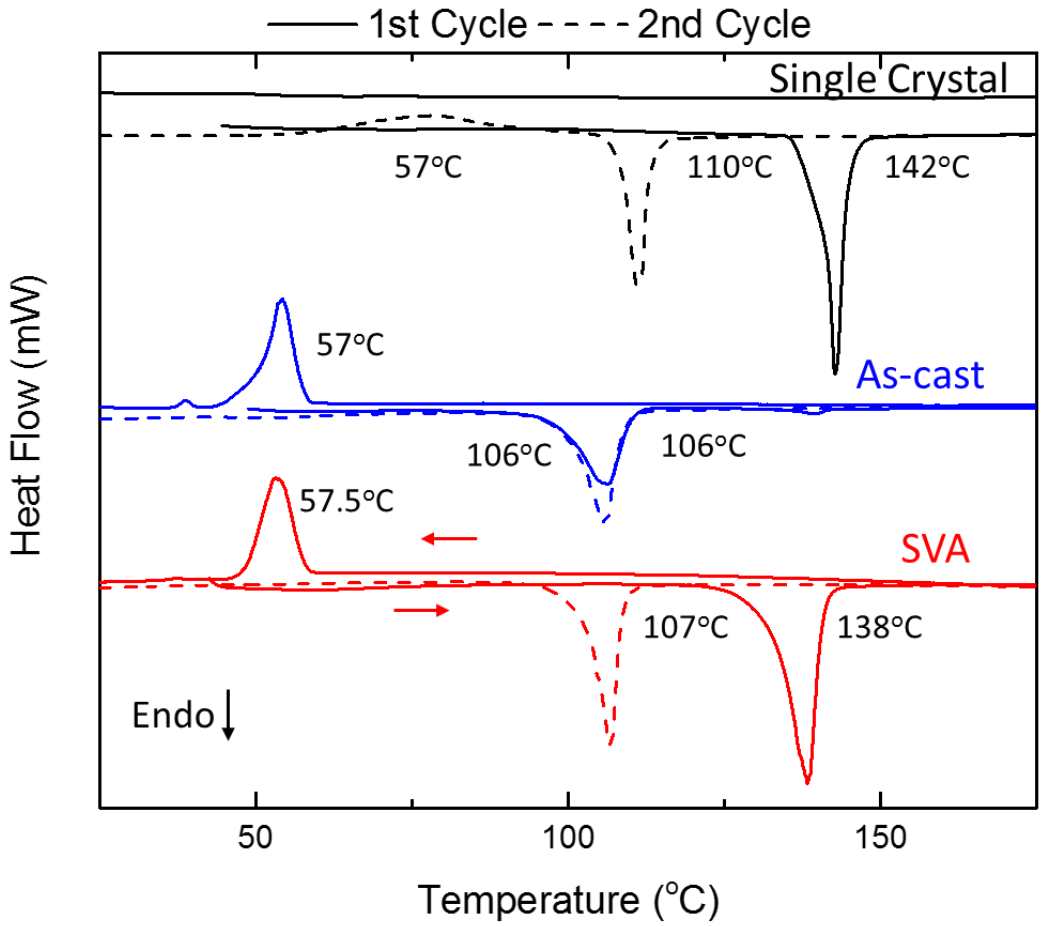

Figure 14 Heating (solid), cooling (solid), and 2nd heating (dashed) thermograms of BT in the single crystal (black), drop casted (blue), and solvent vapor annealed (red); heating rate, 10 °C/min.

The first heating curve reveals the crystal phase of these samples. The BT single crystal (black), and SVA (red) samples show similar melting onsets around 140˚C. This supports the conclusions drawn in GIXD analysis which indicates large similarities between the single crystal and SVA microstructures. We attribute the 'cold-crystallization' of the single crystal sample to the slow kinetics of the bulk system. All three samples have a second melting transition (dotted line) around 106-110˚C, indicating that regardless of initial processing conditions, BT adopts the thin film polymorph upon melting and recrystallization under these experimental conditions. GIXD attempts to observe this transition were inconclusive due to dewetting of films upon melting. In

summary, these experimental observations corroborate the GIXD results, as the SVA sample's DSC scans resemble that of the bulk single crystal. Post-processing and polymorph control are also demonstrated as a possible handle to tune a material's thermal properties.

To quantify the effect of molecular packing changes on charge transport within the films, PFBT-treated Au[88], bottom-gate, bottom-contact field-effect transistors were fabricated on 300 nm thermally grown silicon dioxide heavily doped Si wafers. The BT films spin-coated from chloroform solution had hole mobilities of 1.31 x 10^{-4} $cm^2/V{\cdot}s$, threshold voltage of 2.9 V, and an on/off ratio of 10^2. Transfer and output characteristics are shown in **Figure 15**. Devices measured after solvent vapor annealing showed a significant improvement in performance, with mobilities as high as 0.12 $cm^2/V{\cdot}s$, V_T of -12.6 V, and on/off of 10^5 for grains parallel to channel, three orders of magnitude increase in mobility over as-cast devices.

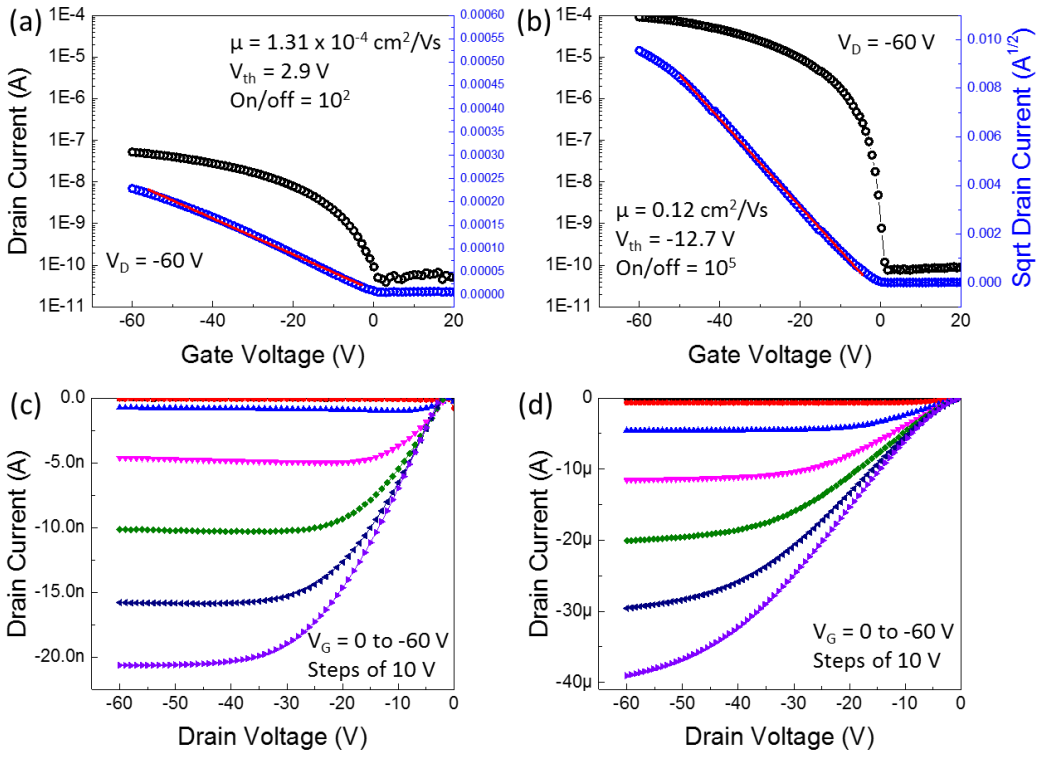

Figure 15. (a) Transfer characteristics in the saturated region of the as cast BT film and (b) SVA film. (c) Output characteristics of the as cast BT and (d) SVA film.

Using the method of crystallization by which crystallization is initated from the edge of the substrate, we fabricated devices with a large range of grain orientations relative to the channel. As carrier mobility in many high performance organic semiconductors is orientation-dependent[23,89-94], it is critical to study and understand the effect of grain orientation on device performance.[95,96] The solvent annealed film allowed us to conduct a detailed study into the anisotropy of charge transport in bistetracene films. The grain orientation of the films was measured using polarized optical microscopy. In total, over 200 devices were measured, and by plotting the mobility versus the grain orientation, a clear angular dependence of the mobility within bistetracene solvent annealed films is shown in **Figure 16**. The mobility of the films in which the grains were oriented perpendicular to the channel were on average 12 times lower than that of the parallel grain orientation, much larger than the anisotropy value of 3.4 from the transfer integral calculations[78], similar to mobility anisotropy measurements of single crystals, demonstrating the role of grain boundaries at this channel length (50 μm).[97] Yet, this mobility anisotropy compares well to the benchmark two-dimensional brick-layer packing small molecule, TIPS pentacene, which in the solution processed crystalline thin film exhibits mobility anisotropy on the order of 7.5 - 10.[96,98]

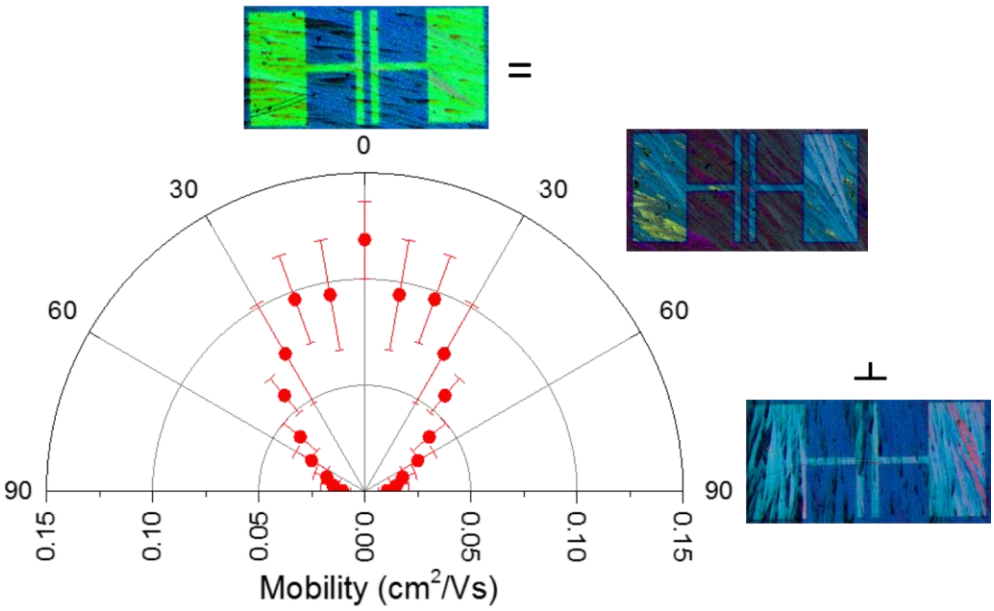

Figure 16. Polar plot of the hole mobility versus grain orientation angle of solvent vapor annealed BT film. The mobility data is reported from 0° to 90° and reflected to show the expected behavior over 180°. Devices with grains oriented at 0° are denoted as parallel, and grains oriented 90° to the channel are denoted as perpendicular devices.

To probe how molecular packing and orientation effect the mechanism of charge transport[99], carrier mobility measurements were carried out as a function of temperature. Three different conditions were tested, the first sample was spin-coated and solvent vapor annealed for 30 minutes to isolate the thin film polymorph of BT. The other films were solvent annealed for 8 hours to induce a phase transition to the bulk crystal phase, and devices were tested with grains oriented parallel or perpendicular to the channel. The transistors were measured under vacuum with decreasing temperature ranging from 300 to 100 K in 25 K intervals. The typical temperature dependent mobility for each sample is shown in **Figure 17**. The thin film phase of bistetracene exhibited thermally activated charge transport, with the mobility decreasing in two stages, a steep decline in the high-temperature region (300-200 K), followed by a less drastic decrease in mobility in the low temperature region (100-200 K), with an activation energy of 39 meV obtained from a fitted Arrhenius equation. Contrary to the thin film polymorph of bistetracene, the solvent

annealed devices showed an increase in mobility with decreasing temperature in the high temperature range for both the parallel and perpendicular devices. Similar temperature behavior is seen in other high-mobility solution-processed small molecules[100], explained by the intrinsic transport behavior dominated by lattice scattering.[101,102] The parallel devices mobility increased in the temperature range 250 K < T < 300 K, before plateauing between 200K < T < 250 K, and before decreasing upon further cooling. From the thermally activated low-temperature region, an activation energy of 4.7 meV was calculated. The perpendicular devices showed similar temperature dependent behavior to the parallel devices, with the mobility increasing in the 200 K < T < 300 K, before becoming thermally assisted below 200 K with a slightly higher activation energy of 5.7 meV. Most notably, we measured a non-monotonous temperature dependence[103-106], with a negative temperature coefficient of the mobility for both parallel and perpendicular devices at high temperatures, contrary to the thin film polymorph, which exhibits a thermally activated decrease in mobility with decreasing temperature over the entire investigated range.

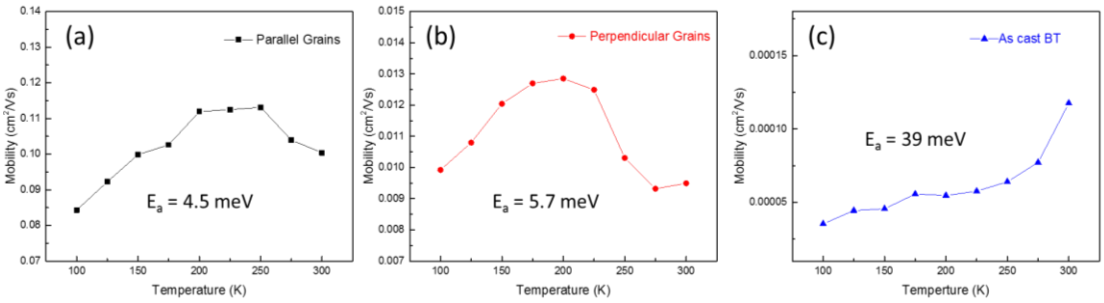

Figure 17 Temperature-dependent saturation mobility (V_D = -60 V) measured in 50 µm channel of (a) solvent-annealed parallel grains, (b) perpendicular grains, and (c) as cast film. The activation energies (E_a) extracted in the trap dominated regimes are also given.

2.4 Conclusion

We observed and characterized a new thin film polymorph of BT which can be converted to a structure similar to the bulk structure of BT using solvent vapor annealing. This transition was monitored using static and *in-situ* GIXD measurements. Field-effect transistors fabricated from the solvent annealed films exhibited three orders of magnitude increase in hole mobility compared to the spin coated films. Using the highly-ordered solvent annealed thin film, we measured the charge transport anisotropy and found it to be similar to the benchmark two-dimensional π-π stacking small molecule, TIPS-pentacene. Temperature dependent mobility measurements also showed a transition from a hopping charge transport mechanism for the thin film polymorph to a lattice scattering behavior in the solvent annealed film. Our experiments highlight the importance of polymorph control and thermal characterization in not just optimizing device performance, but also be as a powerful tool in better understanding the relationship between molecular packing and charge transport mechanism.

2.5 Acknowledgements

We thank Jack Ly for the material synthesis. Prof. Aram Amassian and Muhammad Naizi for allowing me the opportunity to work in their lab for 3 months at KAUST and help with troubleshooting the initial project. Dr. Detlef-M Smilgies for help with the experimental setup of the *in-situ* GIXD measurements. Prof. Stefan Mannsfeld for GIXD analysis and computational calculations to determine the thin film molecular packing.

CHAPTER 3

CRYSTAL PACKING AND MELTING POINT ALTERNATION IN BTTT MONOMERS

3.1 Introduction

The field of organic electronics has made major breakthroughs in performance over the past decade with mobilities of 1-10 cm^2/Vs now comparable to amorphous silicon[107,108] and organic photovoltaic devices exhibiting power conversion efficiencies >10%.[109-112] Advances in material design, processing, and device fabrication have led to this performance rise, with an increased understanding side chain interactions being a large driving force. For many years, the synthetic focus was novel conjugated backbones, with the belief that side chains had minimal effect on electronic properties, and merely allowed for solution processing. Yet, due to the importance of device microstructure, it has been shown that side chains play a much larger role and are a key chemical handle in designing novel state-of-the-art organic semiconductors, allowing for the fine tuning of a material's physical properties.[113-116] To better understand the impact of side chain length of polymer performance, studies have methodically adjusting the alkyl length[117-119], but there is a drawback to this type of study. The molecular weight variation and dispersity of these polymers can lead to batch variability, and packing frustration increases the difficult to investigate these semiconductors at a molecular level.

In contrast to their parent polymers, oligomers allow for the characterization of well-defined structures due to controlled, monodisperse synthesis and lack of chain entanglement that can frustrate packing and prevent single crystal analysis.[120-122] Oligomers allow for detailed structure-property relations and understanding the nuances of chemical modifications on molecular packing and microstructure.[123,124] Our group has previously exploited oligomers to investigate outstanding questions in the field that were previously inaccessible using a polymer-

based system. By varying the backbone length of PQT to investigate the effect of conjugation length on the transition of a material from small molecule-like to polymer.[125] PBTTT oligomers were used to characterize the unique interaction of the polymer with fullerenes to form a high fidelity intercalated bimolecular crystal.[126] The BTTT dimer formed a intercalated system with a much higher degree of crystallinity, and through x-ray analysis previously unaccusable with the polymer system, the molecular arrangement and unit cell of the cocrystal was determined, with the fullerenes residing within the side chains of the BTTT dimer. Another study addressed the addition of side chains to BTTT oligomers, and through experimental and computational work examined their effect on the backbone torsion angle and propensity of the anti vs syn arrangement.[127]

In this study, we synthesized a series of BTTT monomers to investigate the effect of side chain length and terminal methyl arrangement on interlayer molecular interactions and bulk properties. We find a melting point alternation that arises due to large variations in crystal packing, with an interlayer twist of 90˚ present only for the "odd-type" monomers. These results are further explored with computational results further probing these interactions, with a decrease in interlayer spacing in the twisted conformation driven by a calculated increase in interlayer cohesive energy, resulting in higher melting temperatures.

Alternation behavior have been verified in n-alkane and end-substituted n-alkanes[128-133], self-assembled monolayers[134-138], and silver nanoparticles.[139] N-alkane and derivatives were long known to have melting point alternation effects since the 1800s, yet a generic "packing effects" rationalization was normally given as an explanation. This phenomenon has received more recent attention made possible by advancements in instrumentation and crystallization techniques. The melting point alternation of n-alkanedithiols was found to stem from packing density alternation

as a result of differing interlayer interaction due to differing terminal methyl group orientations (**Figure 18**).[133]

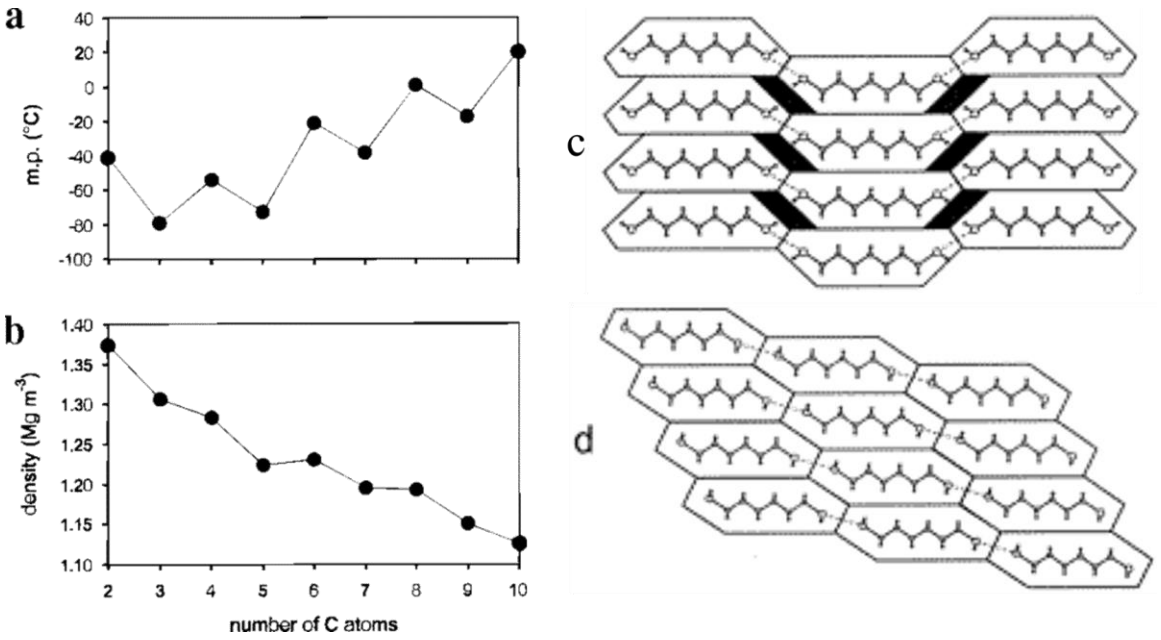

Figure 18. The melting point (a) and density (b) alternation in dithiols. Geometric model of the (c) odd and (d) even dithiols in two dimensions. The odd members restrict the packings, while the even members adopt a dense packing pattern. Reprinted from ref. 131.

A study of the melting point of layered lamella of silver alkanethiolates expanded on the importance of interlayer interaction, with precise control over layer thickness and nanocalorimetry measurements. Melting point alternation was shown for bilayer crystals, yet exhibited a step-wise increase in single layer studies, highlighting the interlayer interactions for property alternation (**Figure 19**).[139]

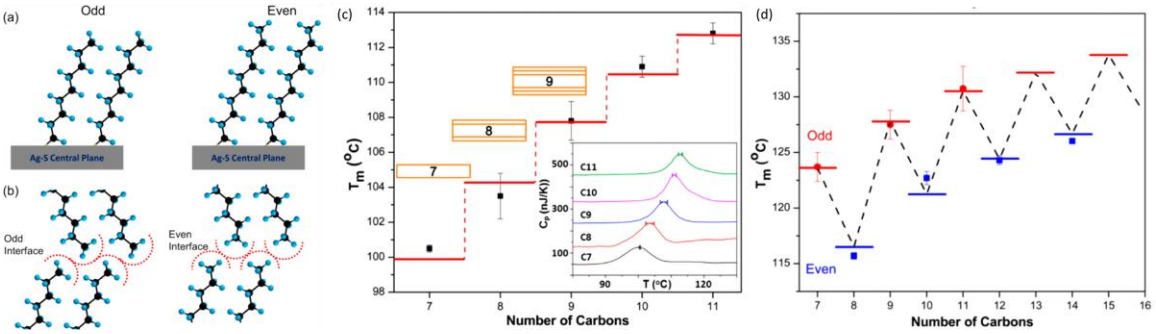

Figure 19 (a) Difference in the orientation of the terminal CH_3 group for both odd and even chains. This difference is due to the tilt of the alkyl chain relative to the central plane normal. (b) Different terminal CH_3 orientation affects the interface formed between layers for odd and even chains. (c) Size-effect melting for single layer $AgSC_n$ with different chain length showing a stepwise increase in T_m. (d) Odd/even alternation of T_m for 2-layer $AgSC_n$. Reprint from ref. 137.

Yet, although these crystal packing alternations have been shown for a wide range of materials, little attention has been paid to this effect in organic semiconducting materials, with few studies even synthesizing odd-length side-chain materials, and those that do, often overlook the possibility of a property alternation, as in the seminal work of Ebata et al, synthesis and characterization of a series of C_n-BTBT molecules with n = 5-14 and stated that, "d-spacing of the other (BTBT) derivatives depended on the length of the alkyl groups: with longer d-spacings were obtained, indicating that all the derivatives take similar molecular packing structures."[140] This study grew a single crystal using one chain length and extrapolated that molecular packing for all other molecules. Yet, using their provided structural information, it is shown that the out-of-plane spacing does not increase monotonously, **Figure 20**, with a distinct crystal packing alternation present. Our BTTT monomer series highlights an extreme of this crystal packing alternation, to highlight side chain alternation as an underexplored handle to modify molecular packing.

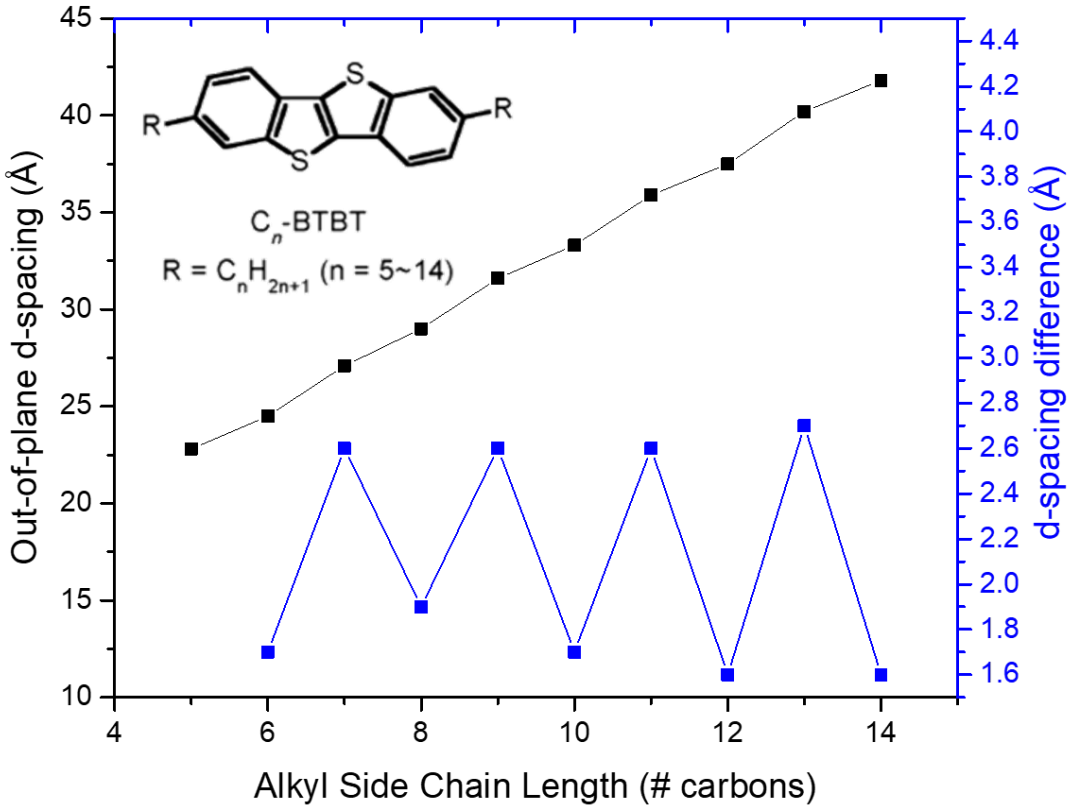

Figure 20 Out-of-plane d-spacing of a series of BTBT molecules with systematically varied side chain length. The nonlinear increase in spacing is highlighted in the d-spacing difference, demonstrating a molecular packing alternation. Data adopted from ref. 138.

3.2 Experimental

BTTT monomers were synthesized according to literature.[126] Single crystals were grown from slow evaporation in hexanes solution.

Differential scanning calorimetry (DSC) measurements were conducted under N_2 atmosphere at a scan rate of 10˚C/min. Standard aluminum crucibles were used. The sample weight was 5 mg.

Single crystal structure analysis via X-ray diffraction was performed by Dr. Sean Parkin at the University of Kentucky.

Ultraviolet-visible (UV-vis) spectroscopy was performed using a Shimadza 3600 UV-VIS-NIR spectrophotometer. Absorption spectrum were measured in chloroform solutions and thin films spin coated from chloroform solutions.

3.3 Results and Discussion

BTTT monomers were synthesized by Stille coupling of 2,5-bis(trimethylstannyl)-theino[2,3-b]thiophene with 2-bromo-3-*alkyl*thiophene. Alkylated thiophenes were synthesized via Kumada coupling as reported in literature.[126,127] The material's chemical structure can be seen in **Figure 21**.

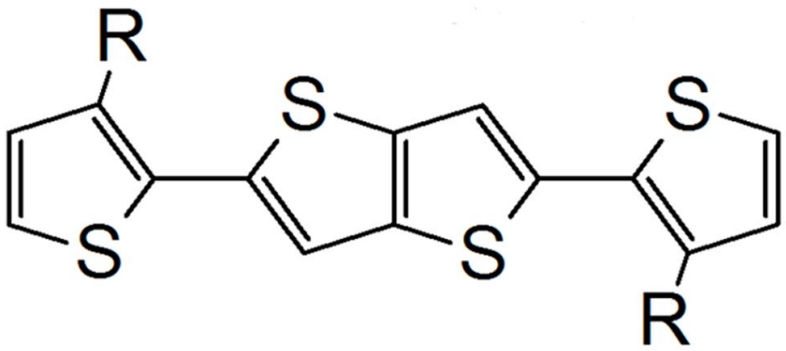

$R = C_7H_{15}, C_8H_{17}, C_9H_{19}, C_{10}H_{21}, C_{11}H_{23}$

Figure 21 Chemical structures of BTTT monomers.

Optoelectronic properties as determined by UV-Vis are equivalent for the set of monomers (**Figure 22**). The spectrum show minimal variation in absorption as a function of side chain length, with a broad, featureless peak centered at 345 nm. The absorption spectrum of the thin film, spin coated from chloroform, revealed a secondary peak at 425 nm, as shown in **Figure 22b**. An optical bandgap of 2.58 eV was calculated using the absorption edge, with no variation seen with different side chain lengths.

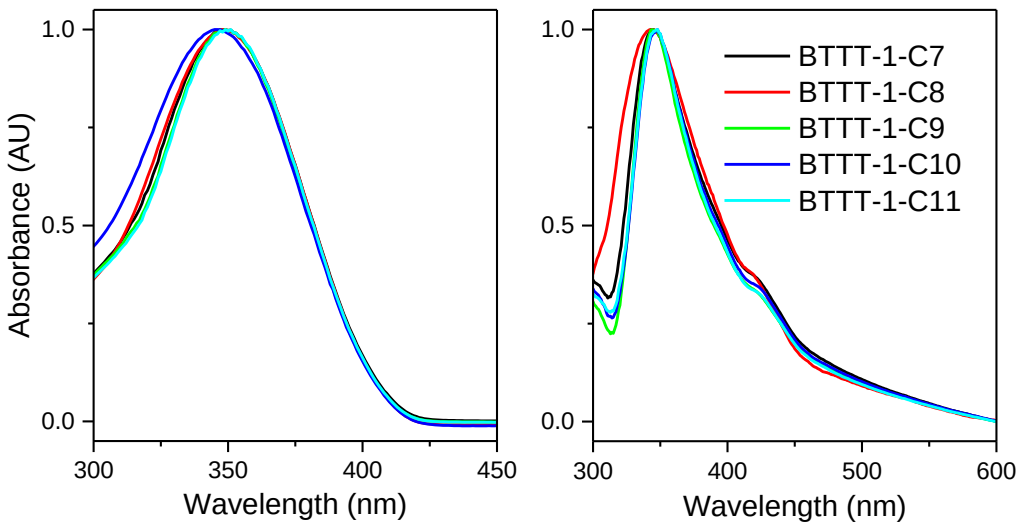

Figure 22 UV-Vis spectroscopy of BTTT monomers in a) chloroform and b) thin film on glass.

Differential scanning calorimetry (DSC) was used to investigate the BTTT monomers thermal properties. Samples were prepared from single crystals loaded into hermetically sealed aluminum pans using heating/cooling ramps ranging from 0 °C to 150 °C at 10°C/min. **Figure 23a** shows the second heating and cooling curves of the BTTT monomers. A melting and crystallization point alternation is present with increased alkyl side chain length as shown in **Figure 23b**. This odd-even melting point alternation is well documented for *n*-alkanes[128]: with even-numbered alkanes melt at higher temperatures than odd-numbered alkanes. However, in the case of the BTTT monomers, this alternation is reversed, with odd-numbered BTTTs demonstrating higher melting points than the even-numbered.

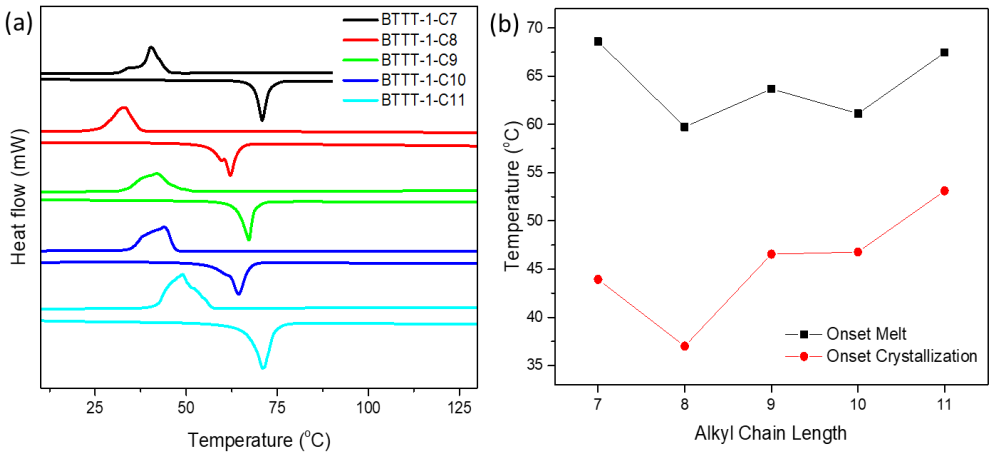

Figure 23(a) Cooling and second heating thermograms of the BTTT monomer series; heating rate, 10 C/min and (b) onset of melting (squares) and crystallization (circles) in the BTTT monomer series; heating rate, 10 °C/min.

To investigate how the chain length affects the solid-state structures of the BTTT monomers, single crystals were obtained from a slow evaporation of a hexane solution and analyzed by X-ray diffraction. Crystals of all BTTT monomers form as very thin, easily deformed plates/flakes. All the structures consist of stacked single layers of BTTT molecules. Within each layer, the BTTT groups and the alkyl chains segregate such that BTTT groups interact solely with BTTT on parallel adjacent molecules, and alkyl chains interact solely with adjacent, parallel alkyl chains. The refined structures of all the monomer crystals exhibit two distinct conformations for the central fused thiophene pair relative to the distal alkylated thiophenes. The diffraction patterns of all crystals contained discrete diffraction spots as well as extended diffuse streaks. By ignoring the diffuse streaks, all could be indexed as primitive monoclinic, with two short (~5Å) and one long (~46Å — 59Å) cell axis, though the convention of defining the monoclinic (i.e., non 90°) angle leads to two distinct packing types (vide infra), shown in **Figure 24**. Depending on crystal quality, however, the occasional crystal (e.g., a C9 crystal), could be transformed to a larger C-

centered monoclinic unit cell that also accounted for the streaks. For the simpler primitive setting, the refined crystal structure models all have the two BTTT conformers superimposed (i.e., disordered), whereas the centered model has the two BTTT orientations alternating within each layer. It seems likely that on a sub-microscopic scale there exist domains in which the two conformers alternate, but that for diffraction from macroscopic crystals this alternation is scrambled, leading to disorder.

The similar layer structure and visual similarities of all C7-C11 monomer crystals notwithstanding, the underlying crystal packing falls into two distinct types that vary in the relative orientation of adjacent layers. We initially thought that the two distinct packing types were characteristic of even/odd alkyl chain length. Crystals of the C8 and C10 monomers crystallize with alternate BTTT layers rotated by 180° by virtue of the 2_1 screw axis (of space groups $P2_1/n$ for C8 and C10). In contrast, in C7, C9, and C11, the layers are related by the c-glide operation (space group $P2_1/c$). We later found exceptions for crystals of the C8, but not for any of the other chain length variants. In both layer stacking types, the interlayer interactions are very weak, consisting solely of contacts between the end-methyl groups of the alkyl chains. It should be stated that these crystals/diffraction patterns were all exceedingly difficult to handle/measure, so the possibility exists that both polymorph types exist for all C9—C11 variants. It is also possible that some crystals are composites that include domains with both types of layer stacking. Indeed, many crystals with uninterpretable composite diffraction patterns were encountered during the crystallographic analyses.

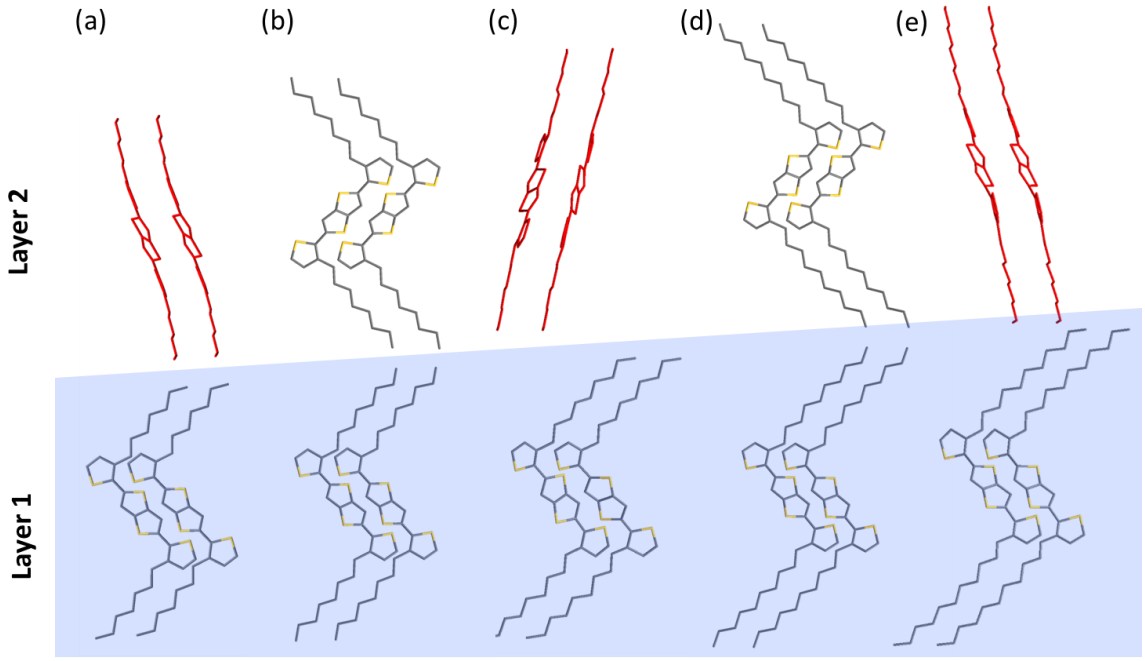

Figure 24 Crystal structures of (a) BTTT-1-C7, (b) BTTT-1-C8, (c) BTTT-1-C9, (d) BTTT-1-C10, and (e) BTTT-1-C11.

The difference in orientation of the terminal CH_3 groups in the odd and even chains plays a large role in this alternation. The terminal CH_3 group for the odd-numbered BTTT is oriented parallel to its neighboring layer, while the even-numbered terminal CH_3 group is oriented in a perpendicular manner. Examining the spacing of two monomer layers, we further understand the variations between the even and odd-type packing (**Figure 25**). It is shown the odd-type packing with the interlayer twist has a smaller unit cell height. Comparing the d-spacing distance at increasing side chain length highlights the distinct unit cell height difference between the two packing types. Measurements of the interlayer spacing between the terminal methyl groups corroborates that the twisted interlayer structure allowed for a decrease in interlayer spacing, this tighter packing is reflected the increase in melting temperature of the odd-type crystals.

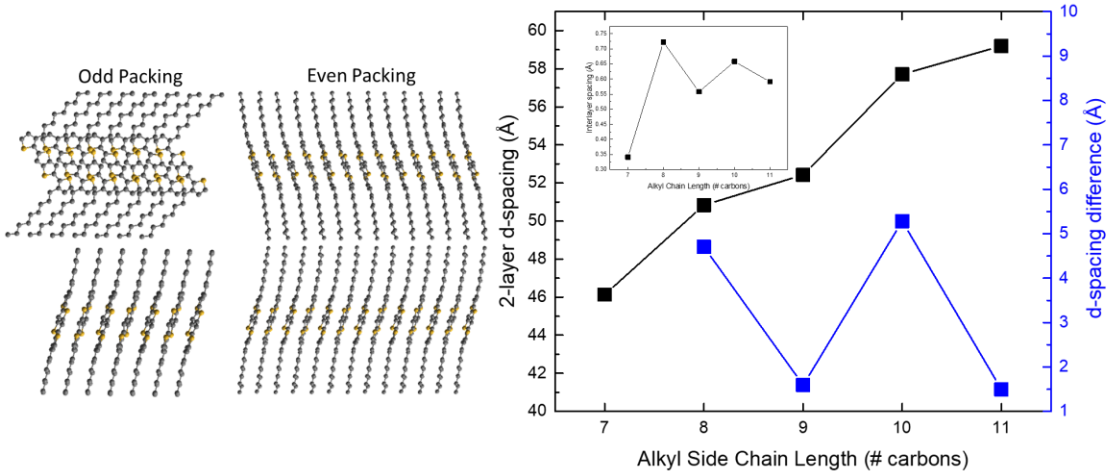

Figure 25 (left) 2-layer odd and even type packing. (right) 2-layer out-of-plane spacing (black) of the BTTT monomers as a function of chain length and (blue) the d-spacing difference with the addition of one carbon. The inset shows the interlayer spacing between the terminal carbons.

To illustrate the underlying interlayer interaction that leads to this odd-even effect, cohesive energies, defined as the total energy cost for dissociating molecules in the crystal, are calculated for both the crystals and the 2D mono-layer periodic structures extracted from the corresponding 3D crystals. The cohesive energy differences between the 2D and 3D structures will be used as the descriptor for estimating the strength of interlayer interaction. As shown in **Figure 26**, the intralayer interaction is much stronger than the interlayer interaction, which is expected due to the sulfur-based short contacts. Moreover, while the intralayer interaction increases almost linearly with respect to the side chain length, there is an odd-even oscillation in the interlayer interaction which indicates two types of interlayer structures.

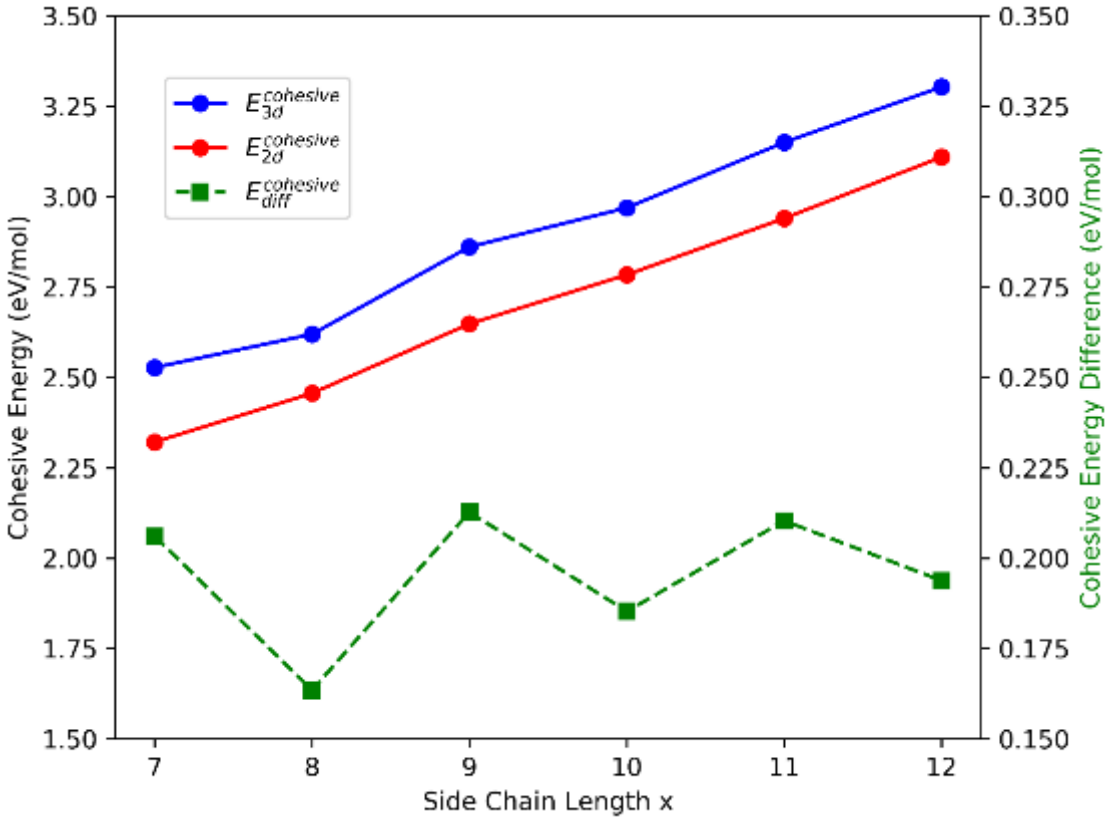

Figure 26 Cohesive energies in BTTT monomer crystals.

The difference in interlayer interaction can be, to some extent, explained by a purely geometric analysis of the alkyl chain topography at the interface. Such analysis is based on the molecular surface defined by Lee and Richards.[141,142] Following the scheme in **Figure 27a**, the surface morphology can be visualized by a colormap where the relative height of a certain point P on the surface, zP ≡ HP /H0, is depicted by the color. As shown in **Figure 27b**, the parity of x leads to different ending structures of the alkyl chains, thus distinct morphologies of the interlayer interfaces.

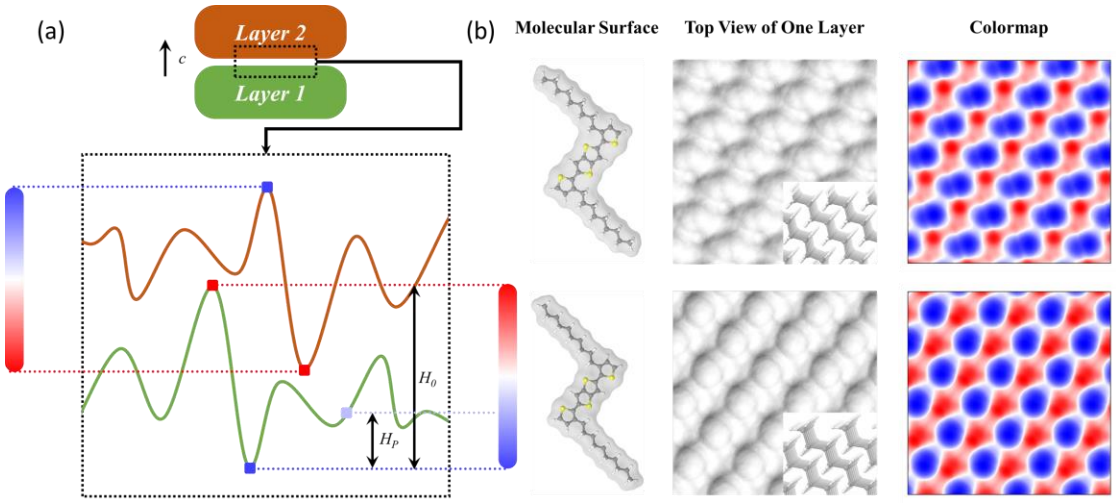

Figure 27 Geometric analysis for the interlayer interface. (a) Color scheme for illustrating *z*, the relative height of a certain point on the surface. (b) Differing terminal structures highlight the distinct morphologies of the interlayer interfaces of (top) odd and (bottom) even materials.

With such colormaps of both layers at the interface, we can proceed to investigate the interface interaction by the values of (z1 + z2)/2 which describes the overlap/contact of two molecular surfaces. That is, if (z1 + z2)/2 = 0.5 then both the overlap and the spatial gap between two molecular surfaces are minimized. One should notice in this case such description is valid due to the existence of an inversion center in the molecule. As shown in **Figure 28**, interfaces in four different crystals, namely BTTT-C9, pseudo-BTTT-C9 (built from simulations with layers packed as x is even), BTTT-C10, and pseudo-BTTT-C10 (built from simulations with layers packed as x is odd), are examined. When x = 9, the distribution of (z1 +z2)/2 in the pseudo-crystal is wider with respect to the one in real BTTT-C9, and the colormaps indicate more surface contacts appear in the pseudo-crystal. Such observations over the geometries of interface are in agreement with the DFT calculations in which the cohesive energy of real BTTT-C9 is 129 meV higher than that of pseudo-crystal. The same situation is also present when x = 10 and the cohesive energy raised 136 meV from pseudo-crystal to the real one.

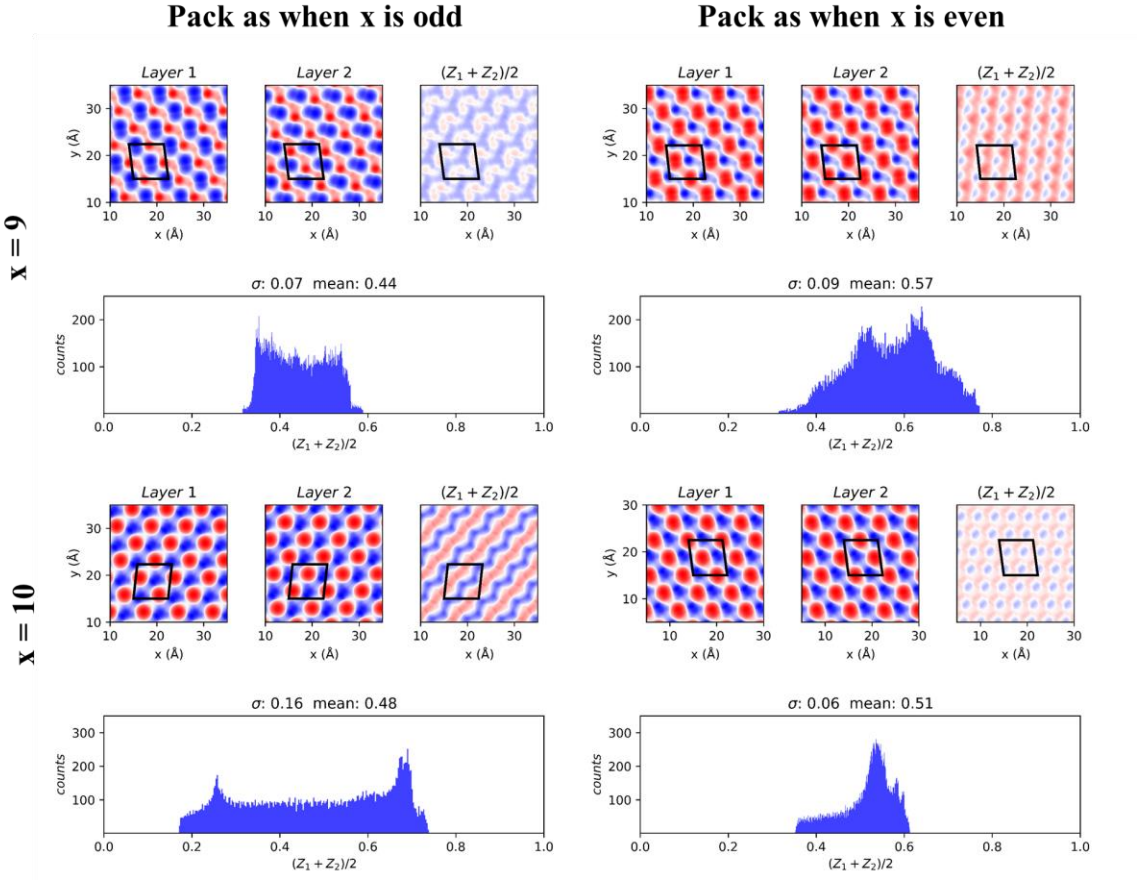

Figure 28 Packing comparison between real and pseudo-crystals.

To explain the significant difference between surface morphologies, one plausible argument is such difference is strongly affected by the angle between the extending direction of alkyl chain and the layer stacking direction (c axis). It is interesting that while the odd-even effect is still present in other crystals where θ is small, such as n-alkanes and BTBT-Rx,[128,140] no oscillation in layer stacking is observed. It is possible that there is a critical value θc beyond which the odd-even effect would be powerful enough to guide layer stacking during the crystallization.

An anomalous observation at side chain lengths of x = 9, 12, the disorder in crystal structures (**Figure 29a**) does not exist and the unit cell is large enough to incorporate 4 molecules, while in other cases the unit cell is smaller and only has two molecules. The two types of unit cell

can be related by a transformation matrix as depicted in **Figure 29b**. This intrigues us to verify the crystallographic results by evaluating the relative stabilities of two well-defined structures in 2d: the 'primitive' structure built from the larger unit cell, and the 'supercell' structure generated by applying the aforementioned transformation to the smaller unit cell with only one disorder group. As shown in **Figure 29c**, the primitive structure is around 50 meV more stable than the supercell structure, which suggests that the disorder may be a result from interlayer stacking.

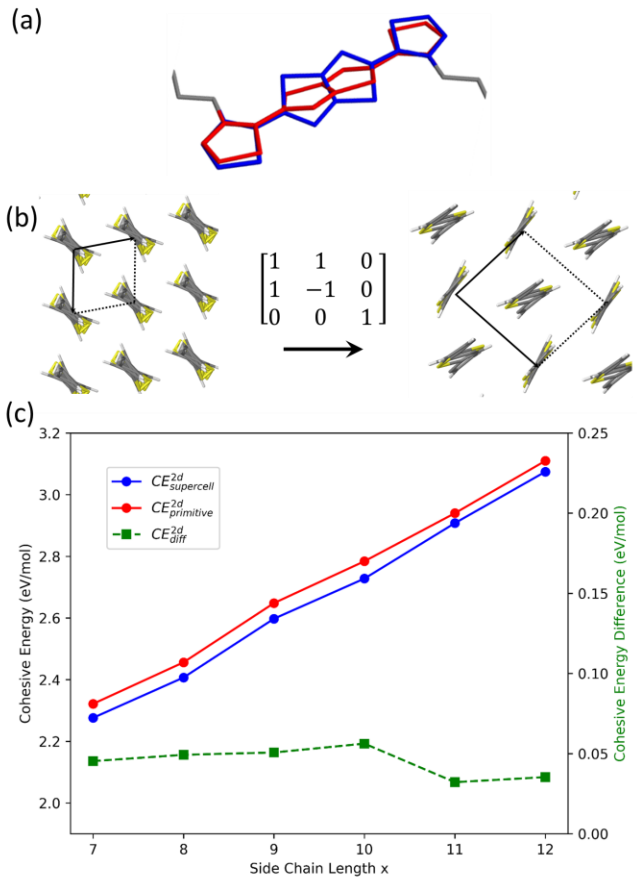

Figure 29 a) The disorder groups present in BTTT-C7, C8, C9, and C11. (b) The transformation matrix relating the "primitive" 2 molecule unit cell and 4 molecule "supercell". (c) cohesive energies of the two types of unit cells, demonstrating that the primitive structure is roughly 50 meV more stable than the supercell structure, which suggests that the disorder may be a results of interlayer stacking.

3.4 Conclusion

We synthesized and characterized a series of BTTT monomers and discovered a melting point alternation brought on by crystal packing differences in which the odd-type monomers exhibit a molecular twist that enables a smaller interlayer spacing. This phenomenon was further characterized with computational tools that demonstrated that this interlayer is favorable for increasing the cohesive energy of the system and is due to the terminal methyl vectors. The pronounced twist, which has not been demonstrated before in systems that exhibit alternation effects could be due to the extreme terminal methyl vectors caused by the side chain tilt angle. This study characterizes an extreme case of crystal packing alternation in an organic semiconducting material to highlight the effect of even-odd assembly as an under-utilized and under-reported handle for tuning the molecular packing of organic semiconducting materials.

3.5 Acknowledgments

We thank Ben Cherniawski for the synthesis of the BTTT monomers. Prof. Sean Parkin for going above and beyond in the characterization of these single crystals. Prof. Chad Risko and Ai Qianxiang for their help with the computation results and fruitful discussions.

CHAPTER 4

THE EFFECT OF SIDE CHAIN LENGTH ON OLIGOTHIOPHENE/FULLERENE INTERCALATION

4.1 Introduction

Morphology and microstructural control is essential for efficient organic photovoltaic (OPV) devices.[143-146] Short exciton diffusion lengths in organic semiconductors require careful tuning of domain spacing and purity for efficient charge generation.[147,148] The bulk heterojunction (BHJ) morphology is a widely-adopted strategy to maximize interfacial surface area while maintaining desirable domains spacings.[149,150] It was originally assumed that the donor and acceptor phases were pure, yet there has been experimental evidence of amorphous mixed phases[151-155], and even certain morphologies in which fullerenes intercalate within polymer side chains.[156-162]

Fullerene intercalation has been observed to form both amorphous[158] and crystalline phases[156,159]; intercalated crystalline phases are defined as bimolecular crystals. While intimate mixing of donors and acceptors is detrimental to OPV performance, polymer/fullerene intercalated systems have provided valuable insight into fundamental OPV processes.[163-167] Recently, Banerji and coworkers used PBTTT and fullerene bimolecular crystals to better understand charge separation and recombination physics at the donor-acceptor interface.[168] In general, intercalation provides a powerful approach for the inclusion of small molecules without disrupting microstructure, and has shown promise in doped polymer systems.[169]

Reports investigating the design rules for bimolecular crystal formation reveal that fullerene chemistry and side chain type and spacing influence intercalation.[157,159,162] Fullerenes with or without solubilizing groups are observed to intercalate with compatible polymers. With additional substitutions, the fullerene becomes too bulky to intercalate and phase separation is

observed instead.[157]18 Yet, even though Bis$PC_{61}BM$ and Bis$PC_{71}BM$ do not intercalate; ICBA, with two side groups does intercalate due to the smaller indene groups. It was later determined from the scattering profile that the ICBA packed in a differing manner from the PCBM derivatives, with the indene groups arranged parallel to the polymer backbone, instead of perpendicular with PCBM. Steric limitations can also be imposed by side chains. For all polymers that allow for intercalation, the side chain substitution pattern must offer sufficient space to accommodate a fullerene.[159] This space, called the "pocket", has been modulated by varying the substitution position, density, and side chain branching.[159] See **Figure 30** for chemical structures polymers from the study of McGehee and coworkers that allow and disallow PCBM to intercalate within their crystals. This study does state that, "changes to the PBTT side-chain length do not affect if intercalation occurs".

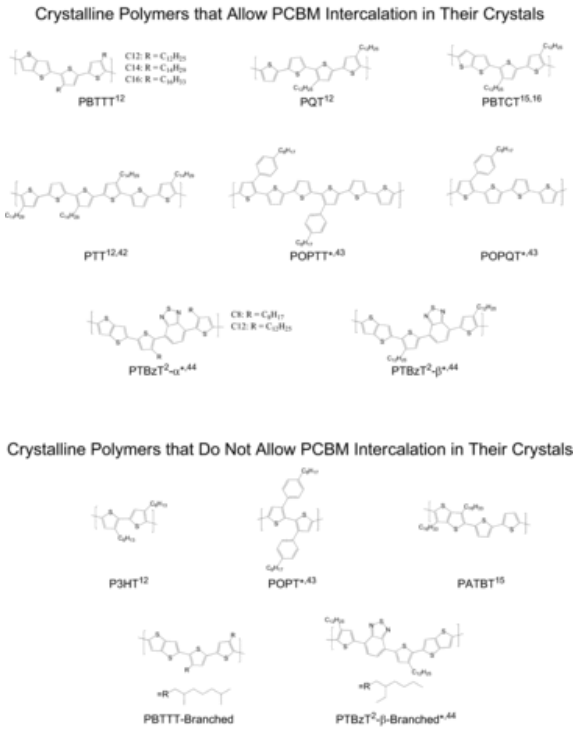

Figure 30 Semicrystalline polymers that allow (top) intercalation of fullerenes in their crystals, and (bottom) polymers that do not allow fullerene intercalation, demonstrating the effect of side chain position, density, and branching. Reprint from ref. 157.

Yet, this effect was not properly explored due to solubility limitations in polymers with decreasing side chain length, limited to PBTTT with C12, C14, and C16 side chains. Oligomers, which exhibit shared properties of the corresponding polymer, provide a versatile experimental platform unhindered by the solubility issues that limit systematic polymer studies. We previously demonstrated PBTTT-oligomers also form a bimolecular crystal with fullerenes with a similar molecular packing to that of the parent polymer.[126] To systematically study the effect of side chain length on bimolecular crystal formation, we synthesized BTTT dimers with linear alkyl side chains from butyl (C4) to tetradecyl (C14) and blend them with three fullerenes derivatives varying in size and substitution (Figure 1A). Grazing-incidence X-ray diffraction (GIXD) reveals a transition from a bimolecular crystal to an intimately-mixed amorphous blend upon decreasing side chain length. We further characterize these oligomer/fullerene blends using differential scanning calorimetry (DSC) and photoluminescence spectroscopy (PL) to understand this transition and probe the newly-observed amorphous phase.

4.2 Experimental

BTTT dimers were synthesized according to literature. $PC_{61}BM$, $PC_{71}BM$, and ICBA were purchased from Nano-C. All solvents were purchased from Sigma Aldrich and used as received.

Thin films for structural analysis as well as electronic characterization were fabricated by dissolving BTTT dimers and/or PCBM in chloroform (10 mg/ml) followed by spin coating at 1500 rpm for 60 seconds.

Differential scanning calorimetry (DSC) measurements were conducted under N_2 atmosphere at a scan rate of 10˚C/min. Standard aluminum crucibles were used. To emulate the thin film processing conditions, 5 mg/mL chloroform solutions were drop cast directly into

aluminum hermetic pans, or dried in glass vials, scraped, then loaded. The sample weight was 4 mg.

Ultraviolet-visible (UV-vis) spectroscopy was performed using a Shimadza 3600 UV-VIS-NIR spectrophotometer. Absorption spectrum were measured in chloroform solution and thin film spin coated from chloroform solutions.

Grazing incidence wide-angle x-ray scattering (GIWAXS) measurements were carried out at D-line (Cornell High Energy Synchrotron Source). A 0.5 × 0.1 mm beam with a wavelength of 1.23 Å and wide band pass (1.47%) was generated from double-bounce multilayer monochromator. The incidence angle was 0.15° with respect to the substrate plane.

Device Fabrication and Characterization: Bottom-contact, bottom gate devices were fabricated using Si wafers with thermally grown SiO2 (300 nm thick) were used as the gate and dielectric, respectively, prepatterned with 50 nm Au bottom contacts. Device channel dimensions of 300 μm and 20 μm for the width and length, respectively, were used. The substrates were sonicated in deionized water and soap, acetone, isopropanol, and deionized water and dried with nitrogen. Substrates were then exposed to UV-ozone treatment for 15 minutes. Electrical device characterization at room temperature was carried out under ambient conditions. Mobility was evaluated in the saturation regime, at a drain voltage Vd = -60 V.

Electron-only devices consisted of ITO/C60-N/Active layer/Ca/Ag. The ITO substrates were sonicated in deionized water and soap, acetone, isopropanol, and deionized water and dried with nitrogen. Substrates were then exposed to UV-ozone treatment for 15 minutes. 2 mg/ml solution of C60-N in TFE was spin coated at 500 rpm for 5 seconds, then 2000 rpm for 55 seconds. The 10 mg/ml chloroform active layer solution was then spin coated at 1500 rpm for 60 seconds. The substrates were then transferred into a thermal evaporator within a N_2 glove box where a 12 nm Ca layer was deposited at 0.1 Å/s at a base pressure of 1×10^{-6} mbar and then without breaking

vacuum a 100 nm Ag layer was deposited at 1.0 Å/s. Hole-only devices of the dimers were fabricated using the architecture ITO/PEDOT:PSS/Active layer/MoOx/Ag. The ITO substrates were sonicated in deionized water and soap, acetone, isopropanol, and deionized water and dried with nitrogen. Substrates were then exposed to UV-ozone treatment for 15 minutes. PEDOT:PSS solution (AI 4083) was spin coated at 2000 rpm for 60 seconds and heated at 130 ˚C for 15 minutes to remove any excess water. The 10 mg/ml chloroform active layer solution was then spin coated at 1500 rpm for 60 seconds. The substrates were then transferred into a thermal evaporator within a N_2 glove box where a 10 nm MoO_x layer was deposited at 0.1 Å/s at a base pressure of 1 x 10^{-6} mbar and then without breaking vacuum a 100 nm Ag layer was deposited at 1.0 Å/s.

4.3 Results & Discussion

Detailed synthesis is shown in the appendix and the general procedure has been previously reported.[126,170] Briefly, 3-alkylthiophenes were synthesized through Kumada coupling of alkyl Grignards and 3-bromo thiophene. The 2 position of the thiophene was selectivity brominated with NBS to afford 2-bromo-3-alkylthiophene. Stille coupling of 2-bromo-3-alkylthiophene and 2,5-bis(trimethyltin)-thieno[3,2-b]thiophene yielded the BTTT monomer. The monomer is monobrominated with NBS and purified prior to Stille coupling with hexamethylditin to afford the final product. Precursors and final products were purified with column chromatography (silica gel) in hexanes. We selected [6,6]-phenyl-C61-butyric acid methyl ester (PC61BM), its C70 analogue (PC71BM), and indene-C60-bisadduct (ICBA) fullerenes to explore variations in size and substitution. Chemical structures of BTTT dimers, side chains, fullerenes, as well as interdigitated and intercalated lamellar packings are shown in **Figure 31**.

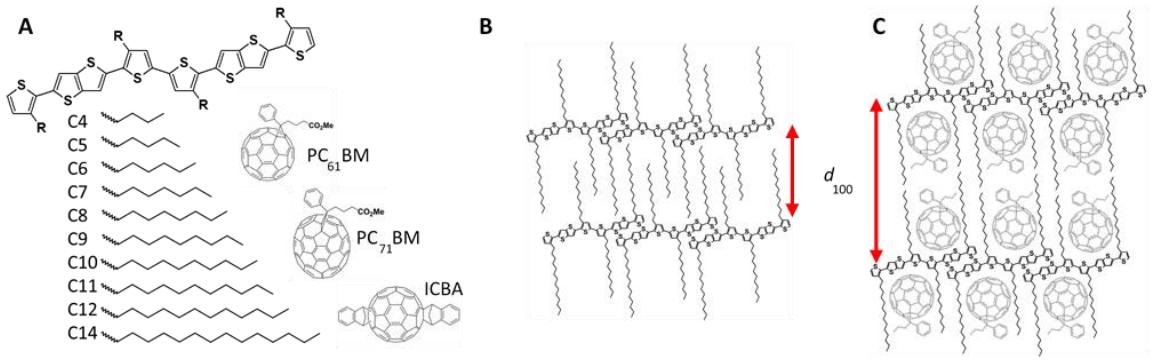

Figure 31 A) chemical structure of BTTT-R dimers and selected side chain series. Cartoon representations of B) neat dimer interdigitation in the solid-state and C) the intercalated BTTT-R/fullerene bimolecular crystal.

Intercalation of fullerenes causes an increase in the lamellar spacing of a BTTT dimer, visualized in **Figure 31b,c**, thus GIXD was employed to measure the lamellar spacing of the neat and blended BTTT/fullerene films to determine if bimolecular crystal formation occurs. Samples were prepared by mixing 50:50 wt% BTTT with PC61BM, PC71BM, and ICBA in a heated chloroform solution and spin coating onto silicon substrates. In the neat films, the BTTT dimers pack in a similar manner to PBTTT, with the lamellar stacking axis oriented out-of-plane with side chain interdigitation.[171] Out-of-plane line cuts of the neat and blended films for all side chain lengths are shown in **Figure 32a**. Additional line cuts and a full set of diffractograms are located in the Appendix. BTTT lamellar spacing in-creases linearly from BTTT-7 (14.9 Å) to BTTT-14 (24.5 Å) similar to PBTTT films with varied side chains lengths.[172] Dimers with side chain lengths of C5 through C8 show evidence of polymorphism in neat films. Upon blending with PC61BM, a shift in the peak positions along qz ~ 0 indicates an increase in lamellar spacing consistent with bimolecular crystal formation for BTTT-7/PC61BM (25.8 Å) through BTTT-14/PC61BM (31.4 Å). Note, despite evidence of multiple polymorphs in the BTTT-7 and -8 neat films, addition of fullerene unifies the morphology to a single, intercalated packing. **Figure 32b** shows the d-spacing vs side chain length in the neat and blended films.

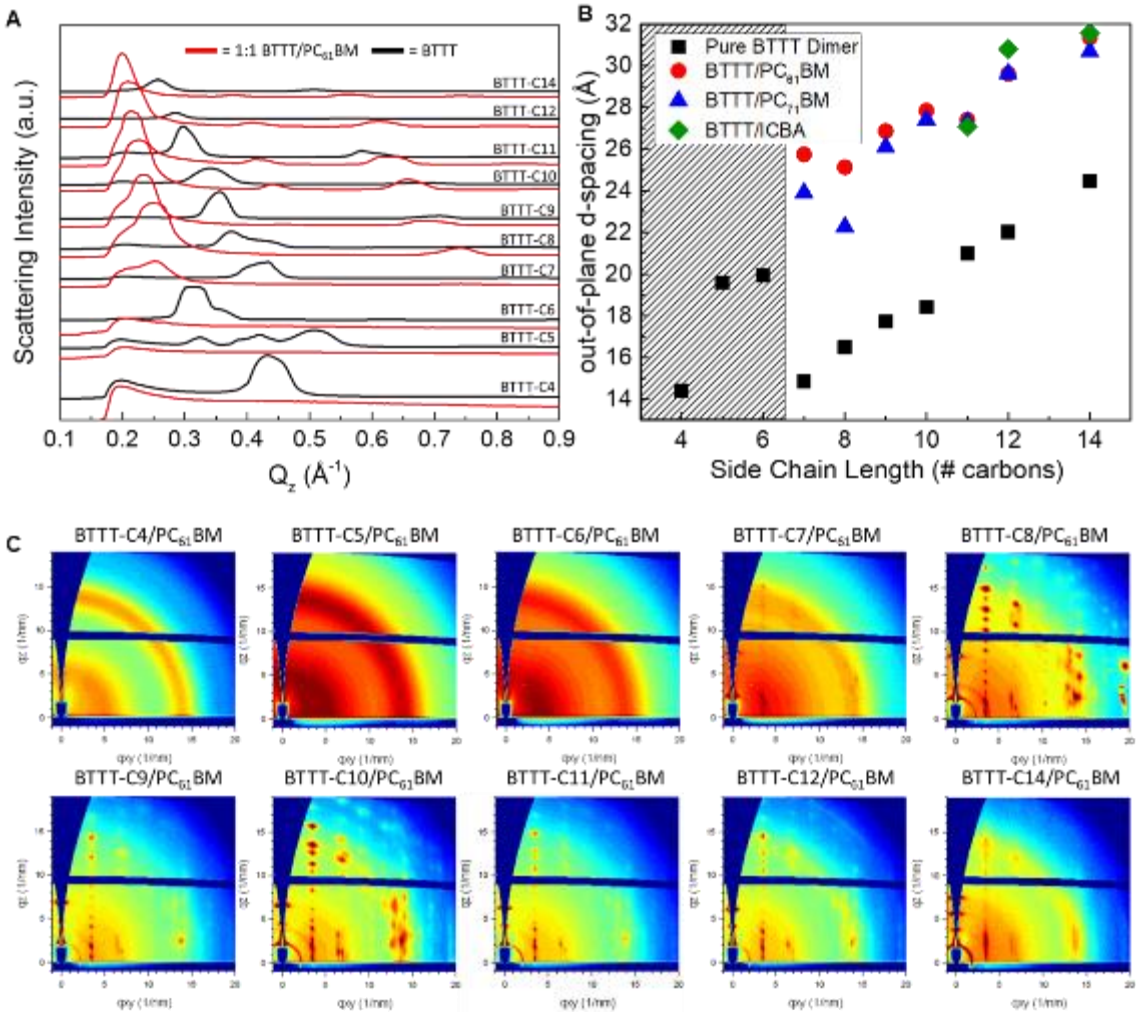

Figure 32 A) GIXD Q_z linecuts of neat dimer films (black) and $PC_{61}BM$/dimer blended (1:1 wt%) films. B) lamellar d-spacing as a function of side chain length for neat films (black, square), $PC_{61}BM$ blended films (red, circle), $PC_{71}BM$ blended films (blue, triangle), and ICBA blended films (green, diamond). Line fill indicates amorphous blends without bimolecular crystal formation. C) Diffraction patterns of the BTTT dimers blended with $PC_{61}BM$.

BTTT with hexyl (C6) and shorter side chains do not follow the linear lamellar spacing trend observed for longer side chains due to a different thin-film molecular packing. Interestingly, blends of BTTT-6 and shorter with fullerenes do not show an increase in d-spacing, instead the BTTT scattering intensity is completely suppressed and replaced by broad powder rings corresponding to PC61BM, indicating a morphology of amorphous dimer and nanocrystalline

PCBM. However, we contend that even at decreased pocket height, fullerenes can still occupy the space between the side chains and intercalate, disrupting aggregation and crystallization of the dimer and fullerene. In separate studies, polyterthiophene (PTT) also exhibited similar side chain mediated behavior. McGehee and coworkers report bimolecular crystal formation in fullerene blends with PTT-C14 containing long tetradecyl side chains.[156] Yet, Scharber and coworkers reported fullerene blends with shorter hexyl side chains, PTT-C6, show crystallization suppression also observed in our study and attributed this to fullerene intercalation.[173] These studies support our claim that BTTT dimer-fullerene blends transition from crystalline to amorphous with decreasing side chain lengths while maintaining an intercalated morphology.

Additional experiments varying fullerene size (PC61BM vs PC71BM) showed no significant differences in lamellar spacing of the bimolecular crystal or transition to the amorphous blend. We do note a small deviation in lamellar spacing at side chains C7 and C8 with PC71BM. ICBA, an alternate di-substituted fullerene known to intercalate with PBTTT, was also investigated. ICBA blends demonstrated only partial intercalation into BTTT dimers ≥ C11. Additionally, blends with BTTT-11, -12, and -14 exhibit lamellar spacing corresponding to domains of both pure dimer and bimolecular crystal. Films of ICBA with BTTT-10 and shorter show suppression of the co-crystalline microstructure, mirroring PCBM blends with smaller side chains. Interestingly, the lamellar spacing of the ICBA bimolecular crystal was very similar to the PCBM blends, differing from what has been previously reported with blends of PBTTT/ICBA, which exhibited a smaller expansion of the side chains upon the introduction of ICBA compared to PCBM derivatives.[162] This could be due to the ICBA arranging in a differing manner in which the side groups are not perpendicular to the BTTT side chains and thus contribute to the lamellar spacing of the bimolecular crystal.

To probe the order to disorder transition observed in GIXD, we characterized the thermal behavior of both neat and blended films of BTTT -12, -9, -6, and -4 with DSC. **Figure 33** shows the first heating thermograms of the neat dimer and PC61BM blends. To emulate the thin film processing conditions, 5 mg/mL chloroform solutions were drop cast directly into aluminum hermetic pans, or dried in glass vials, scraped, then loaded. All neat materials exhibit strong melting endotherms. BTTT-6, -9, and -12 melt around 100 °C, whereas BTTT-4 melts at 155 °C. Upon blending, BTTT-12 and -9 show a melting point shift, indicating a new crystalline phase which we attribute to the bimolecular crystal. In the blended samples of BTTT-6 and -4, the melting transition is suppressed. The absence of a strong melting endotherm in BTTT-6 and -4 support the featureless diffraction patterns and the proposed order to disorder transition at side chain lengths ≤ C6. Full heat/cool/heat cycles of drop-cast samples, neat powders, and BTTT-4 blends with PC61BM, PC71BM, and ICBA are available in SI.

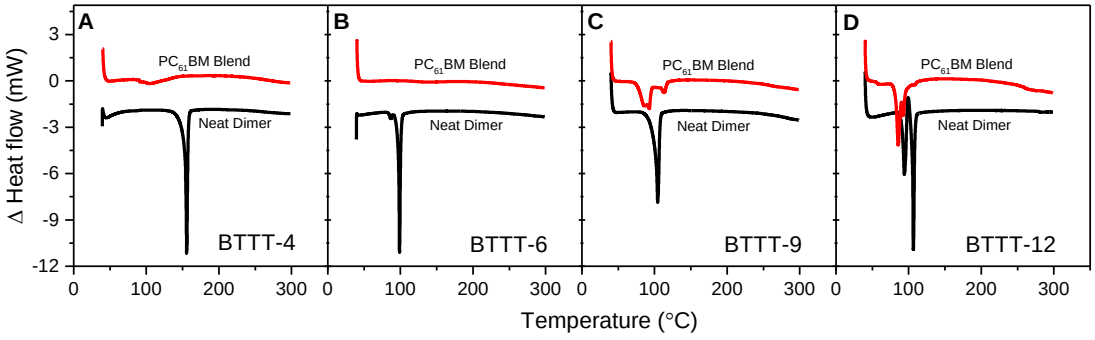

Figure 33 Differential scanning calorimetry first heating curves of neat dimers (black) and 50:50 wt% blends with $PC_{61}BM$ (red) of A) BTTT-4, B) BTTT-6, C) BTTT-9, and D) BTTT-12. Exo up.

PL quenching is an indicator of how efficiently excitons can diffuse to a donor-acceptor interface.[174,175] In intercalated systems, excitons are formed in immediate proximity of a fullerene, allowing for near quantitative PL quenching.[157,158] Conversely, in phase separated systems, some population of excitons formed in the donor phase do not reach an interface and recombine emissively.[157,158,163,164,166] To gain insight into the distribution of donor and acceptor molecules

within the amorphous blends, we compare the PL quenching behavior of the co-crystalline and amorphous blends. **Figure 34** shows the PL signal for both neat and blended systems. Upon fullerene blending, both co-crystalline and amorphous systems demonstrated complete quenching. PL spectra of the crystalline and amorphous blends confirms no pure domains larger than the nanometer scale exist.

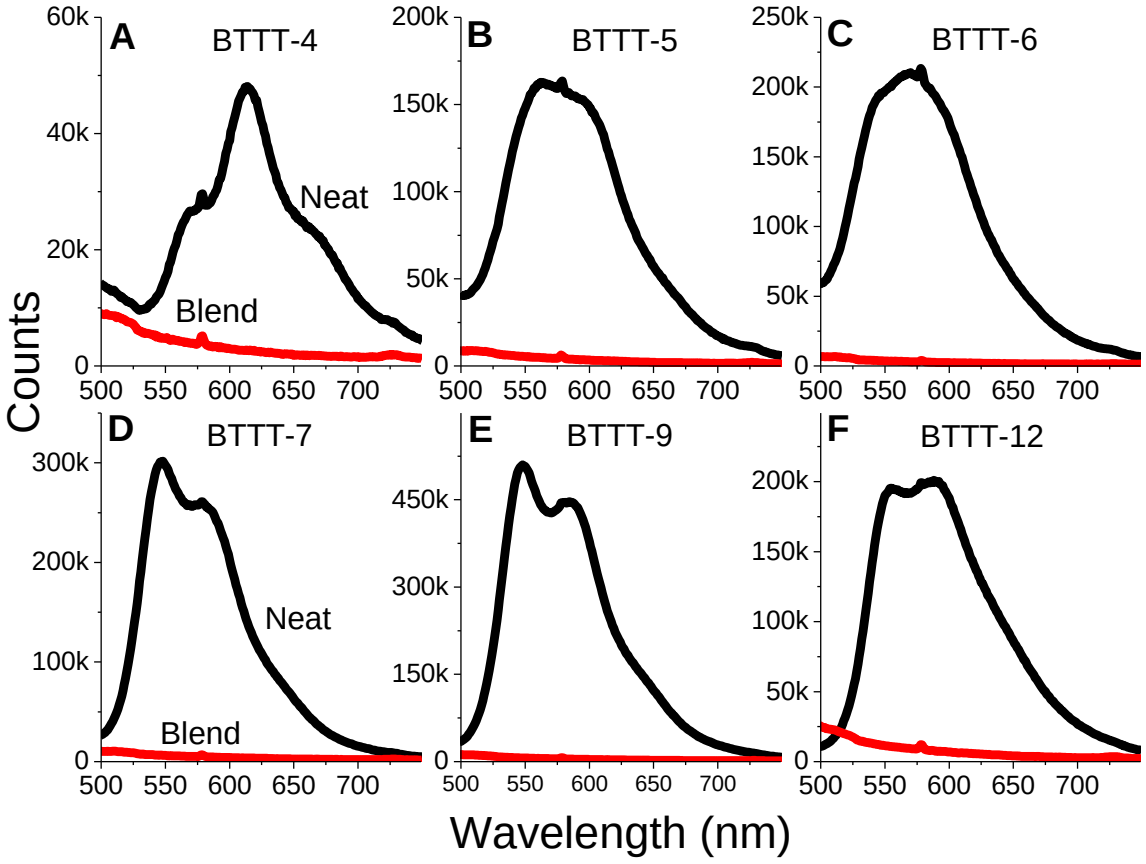

Figure 34 Photoluminescence of neat (black) and 50:50 wt% BTTT/PC61BM (red) films of (a) BTTT-4, (b) BTTT-5, (c) BTTT-6, (d) BTTT-7, (e) BTTT-9, and (f) BTTT-12. Excitation wave-length: 450 nm.

To correlate the morphology to the electronic properties of the bimolecular crystal and amorphous blends, electron-only, hole-only, and field-effect transistor devices were fabricated. In our previous work, we determined the structural model of the BTTT-12/PC61BM bimolecular crystal.[126] This packing is characterized by 1-D connected channels of fullerenes sandwiched

between layers of 2-D connected dimers aligned parallel to the substrate. Due to the highly oriented nature of the cocrystal and the lack of structural information of the amorphous blend, measuring the out-of-plane (electron/hole -only devices) and in-plane (OFET) transport builds a more complete picture of the molecular connectivity and arrangement. BTTT-6 was chosen as a representative dimer of the amorphous blend, and BTTT-12 to represent the bimolecular crystal.

Current density-voltage characteristics of the electron-only and hole-only devices are shown in **Figure 35a,b** respectively. Electron-only devices consisted of ITO/C60-N/Active layer/Ca/Ag. The highest current density is observed in pure PCBM devices. Upon blending, current density decreases, yet electron transport in the amorphous blend of BTTT-6/PC61BM is greater than the bimolecular crystal of BTTT-12/PC61BM. The combination of GIXD and electrical measurements indicates that amorphous blends afford greater three-dimensional connectivity of the fullerene. This is evident from¬ the halo at Q ~ 1.4 Å-1 associated with PC61BM order is more prominent than in the bimolecular crystal. In BTTT-12 devices, the bimolecular crystals orient edge-on to the substrate and causes the fullerenes to lose vertical connectivity and decrease electron transport. Hole-only devices of the dimers were fabricated using the architecture ITO/PEDOT:PSS/Active layer/MoOx/Ag. The current densities of the neat dimers were very similar, yet upon blending with PC61BM the current in the BTTT-6/PC61BM blend (amorphous) was lower than the BTTT-12/PC61BM (bimolecular crystal) due to the loss of BTTT crystallinity.

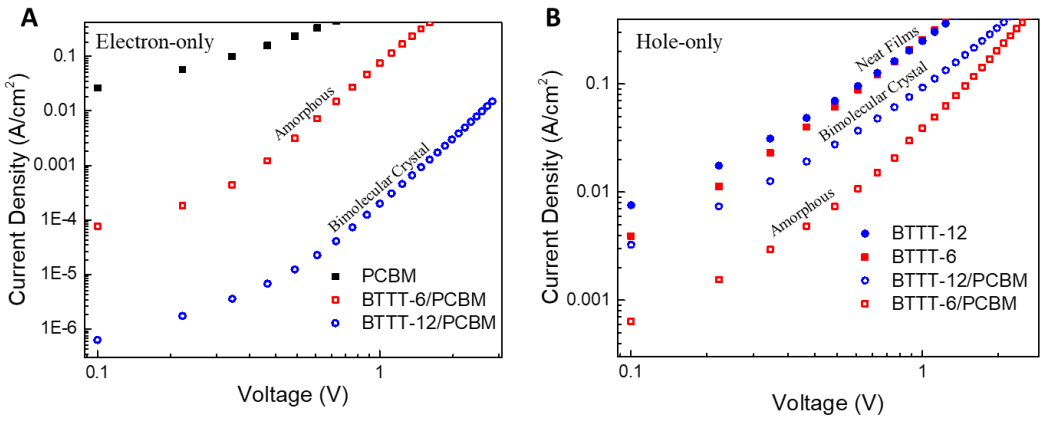

Figure 35 Current density-voltage characteristics of (a) electron-only and (b) hole-only devices comparing neat and blended films that form bimolecular crystals and amorphous blends.

To explore in-plane charge transport within these blends, bottom-gate, bottom-contact field-effect transistors were also fabricated using the same processing conditions consistent with GIXD sample preparation. The mobility of the BTTT-6 was calculated to be two orders of magnitude greater than BTTT-12 in the neat film. GIXD and DSC indicate that BTTT-6 adopts a different thin film packing which accounts for the improved charge transport in the neat film.[170] Upon blending with PC61BM, the BTTT-6/PC61BM device exhibited no field-effect, while the BTTT-12/PC61BM transistor performance improved by two orders of magnitude. Summary of device performance is shown in **Table 2**.

Table 2 OFET characteristics comparing neat and blended films of bimolecular crystals and amorphous blends.

Material	Mobility ($cm^2/V{\cdot}s$)	Threshold Voltage (V)	On/ Off
BTTT-6	$(4.5 \pm 0.25) \times 10^{-4}$	24.9 ± 1.1	10^2
BTTT-12	$(1.27 \pm 0.05) \times 10^{-6}$	9.3 ± 1.0	10^2
BTTT-6 /PCBM	No field effect		
BTTT-12 /PCBM	$(3.0 \pm 0.1) \times 10^{-4}$	12.4 ± 0.7	10^2

While we are uncertain of the fundamental driving force behind the BTTT/fullerene order to disorder transition as mediated by side chain length, we point interested readers to a report by Jayaraman and coworkers.[176] This work details coarse-grain morphology simulations of BTTT dimers with varying side chain lengths and fullerene. They observe a change in the blended morphologies at the shorter side chain length (the BTTT-C6 analog) which is in remarkable agreement with our findings.

To more directly address the underlying forces at play, we highlight a few of our results which provide critical clues. We observe the order to disorder transition of the blended system is dependent on both the side chain length (long vs. short) and fullerene chemistry (PCBM vs. ICBA). ICBA did not illicit different phase behavior, but did shift the onset of the transition to larger side chain lengths. No size dependency was observed in the PC61BM vs PC71BM results, possibly because their size difference is not large enough to cause a shift. Alternatively, the molecular design, bis-adduct (ICBA) vs the mono-adduct (PC61/71BM), could have a larger effect than fullerene size alone.

Regardless of fullerene size/type, small side chains (≤ C6) do not fully envelope the fullerene and solubilizing group within the pocket. This allows fullerenes to establish additional non-bonding interactions which likely contribute to the amorphous microstructure formation. This curious and reproducible micro-structure which is conserved across multiple fullerenes unambiguously indicates that BTTT and fullerene significantly inter-act, even at 'undersized' pocket dimensions.

4.4 Conclusion

In summary, we investigated the effect of side chain length on the formation of BTTT/fullerene bimolecular crystals. BTTT dimers with alkyl side chain lengths ranging from C4 to

C14 were blended with PC61BM, PC71BM, and ICBA to explore fullerene intercalation previously inaccessible with polymer systems. In both PC61BM and PC71BM blended films, we observe two regimes; bimolecular crystal and amorphous intercalated. BTTT -14 to -7 show spontaneous bimolecular crystal formation while BTTT -6 to -4 exhibit a lack of thin film microstructural order as demonstrated by GIXD and DSC. However, complete PL quenching of the amorphous blends indicate that the fullerene and dimer are also molecularly mixed. Hole/electron-only devices were dominated by the dimensionality and crystallinity of the materials. In OFETs, the lack of crystalline order in the amorphous blend resulted in no field effect whereas the enhanced crystalline order in the bimolecular crystal improved charge transport. This work highlights the growing list of side chain related phenomena and rational molecular design considerations essential to morphologic control of organic semiconductors.

4.5 Acknowledgments

We greatly thank Ben Cherniawski for the synthesis of these materials and help putting together this manuscript. Prof. Sean Parkin for single crystal analysis, and Dr. Detlef Smilgies for help with GIXD experimentation.

CHAPTER 5

VARIABLE SIDE CHAIN BTTT DIMERS MORPHOLOGY AND INTERACTIONS WITH FULLERENES

5.1 Introduction

Organic semiconductors have shown promise as an alternative to inorganic semiconductors in optoelectronic devices such as solar cells[110,177], thin film transistors[178-180], and light-emitting diodes[181-183]. Morphology and microstructural control is essential for the development of high performance organic electronic devices.[184-186] Solution processability is a necessity for this materials for utilizing ink-based printing techniques for low cost fabrication on flexible substrates. Thus, solution-processable conjugated materials consist of two parts: pi-conjugated backbones and flexible solubilizing side chains. It was assumed that the conjugated backbone determined the optoelectronic properties of the material, and side chains were added merely for solubility. Yet, morphology and microstructural control is essential for the development of high performance materials and side chains have been shown as a handle to tune a materials absorption, emission, molecular packing, and charge transport.[113]

Side chain arrangement greatly influences a materials interactions and morphology within blended systems.[187-189] A major focus has been placed on blends of conjugated polymers and small molecules with fullerenes, due to their importance in the development of organic photovoltaic active layers. It was originally assumed that the donor and acceptor phases were pure, yet there has been experimental evidence of amorphous mixed phases[151-155], and even certain morphologies in which fullerenes intercalate within polymer side chains.[156,158-162,190] Further exploration into this phenomena revealed the side chain substitution pattern along the backbone must offer sufficient space to accommodate a fullerene.[159] This space, called the “pocket”, has been modulated by varying the substitution position, density, and side chain branching.[159]

Additives or processing techniques to control fullerene intercalation have also been investigated. Asymmetric molecules, such as fatty acid methyl esters[166], were used to control the phase morphology of polymer:fullerene blends (**Figure 36**). The additive's polar end would favor the PCBM, while the alkyl side would favor the side chains of the polymer. Increasing the alkyl length was able to expel larger fractions of fullerene, leading to formation of a pure polymer phase and allow for systematic phase control through alkyl length modification.

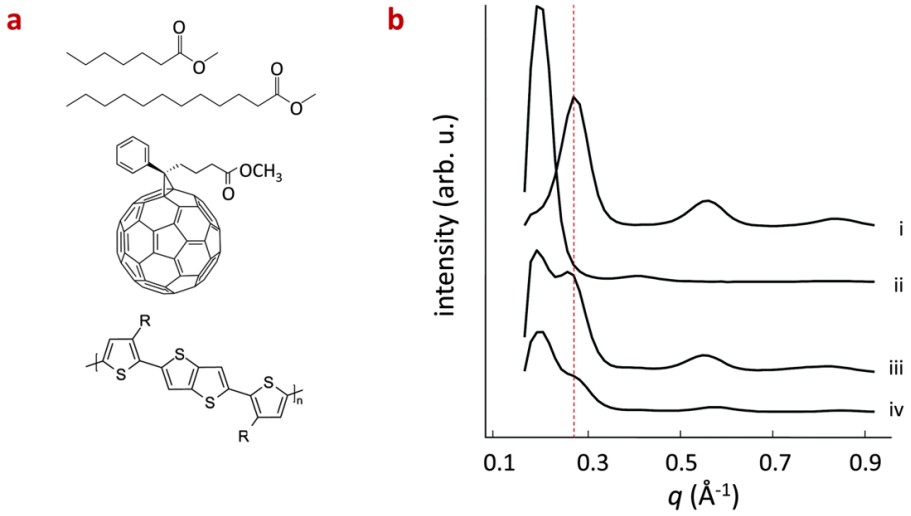

Figure 36 (a) From top to bottom, chemical structures of Me7, Me12, $PC_{61}BM$ and pBTTT where R = $(CH_2)_{15}CH_3$. (b) Grazing-angle incidence X-ray diffractograms of neat pBTTT (i), pBTTT:$PC_{61}BM$, forming co-crystals (ii), pBTTT:Me12:$PC_{61}BM$ (iii) and pBTTT:Me7:$PC_{61}BM$ (iv). The dashed line indicates the position of the (100) diffraction associated with the lamellar packing distance of the neat polymer at $q \sim 0.28$ Å^{-1}. Reprint from ref. 164.

Another study utilizing processing modification of a bilayer system for tuning the diffusion of PCBM molecules into the polymer crystallites by altering the structural order within the polymer film, **Figure 37**.[191] If the polymer layer was given more time to arrange and crystallize through differing casting conditions, upon contact with the fullerene layer, it was less likely to allow bimolecular cocrystal formation.

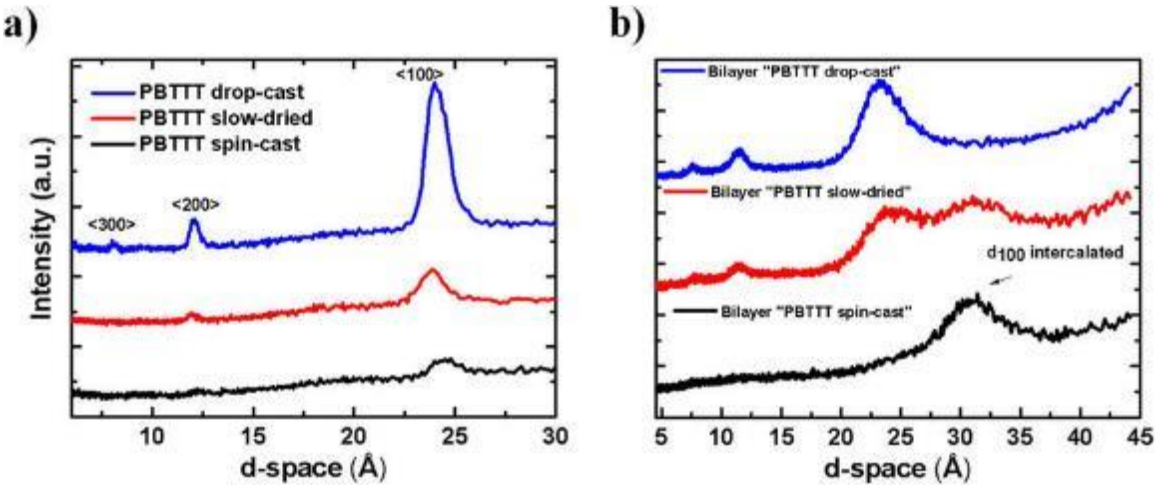

Figure 37 XRD pattern (out-of-plane) of PBTTT pure deposited via spin-casting, slow-drying and drop-casting. The <100> peak (at ~24° for all the films) and its higher orders refer to the lamellar stacking (see ref. 12). None of the pure PBTTT films was thermally annealed. (b) XRD pattern (out-of-plane) of PBTTT/PCBM films obtained by sequentially depositing the PCBM on top of the three different polymer films (PBTTT spin-cast, slow-dried and drop cast). Although perfect bilayers are not formed due to PCBM diffusion and intercalation in the polymer layer, we refer to these samples as bilayer "PBTTT spin-cast", "PBTTT slow-dried" and "PBTTT drop-cast" for simplicity. Note that all the bilayers were annealed at 185 °C for 10 minutes. Reprint from ref. 189.

In our previous work, we investigated the role of side chain length on the intercalation of fullerenes. To explore smaller side chain lengths below the solubility limitations of the benchmark polymer to allow intercalation, PBTTT, we used BTTT dimers, which have been previously been shown to be the smallest unit that can replicate the intercalation properties of the polymer[192], making it an ideal material with increased solubility while maintaining microstructure. At side chains lengths below C6, a transition from a bimolecular crystal to an intimately-mixed amorphous blend was discovered. In this study, we expand this BTTT system to investigate the influence of side chain length and position on solid state interactions and self-assembly by synthesizing a series of BTTT dimers with varying substitution patterns of short C4 (butyl) and long C12 (dodecyl) chains. The substitution pattern is found to greatly effects the morphology and kinetics of the film formation of the materials in the neat and fullerene blended films, even demonstrating the first phase separated linear alkyl BTTT dimer/fullerene blend through side

chain positional control. The side chain position is also shown to influence the assembly of these materials and blends, with thin film self-organization at room temperature. These changes were tracked with a combination of optical microscopy, UV-Vis, and OFET measurements.

5.2 Experimental

BTTT dimers synthesis details are available in the appendix. $PC_{61}BM$ was purchased from Nano-C. All solvents were purchased from Sigma Aldrich and used as received.

Thin films for structural analysis as well as electronic characterization were fabricated by dissolving BTTT dimers and/or PCBM in chloroform (10 mg/ml) followed by spin coating at 1500 rpm for 60 seconds. For aging experiments, samples were placed in shielded vacuum chamber to prevent any degradation from oxygen or light.

Ultraviolet-visible (UV-vis) spectroscopy was performed using a Shimadza 3600 UV-VIS-NIR spectrophotometer. Absorption spectrum were measured in the thin film spin coated from chloroform solutions.

Differential scanning calorimetry (DSC) measurements were conducted under N_2 atmosphere at a scan rate of 10˚C/min. Standard aluminum crucibles were used. The sample weight was 4 mg.

Grazing incidence wide-angle x-ray scattering (GIWAXS) measurements were carried out at D-line (Cornell High Energy Synchrotron Source). A 0.5 × 0.1 mm beam with a wavelength of 1.23 Å and wide band pass (1.47%) was generated from double-bounce multilayer monochromator. The incidence angle was 0.15° with respect to the substrate plane.

Device Fabrication and Characterization: Bottom-contact, bottom gate devices were fabricated using Si wafers with thermally grown SiO2 (300 nm thick) were used as the gate and dielectric, respectively, prepatterned with 50 nm Au bottom contacts. Device channel dimensions of 300 µm and 20 µm for the width and length, respectively, were used. The substrates were

sonicated in deionized water and soap, acetone, isopropanol, and deionized water and dried with nitrogen. Substrates were then exposed to UV-ozone treatment for 15 minutes. Electrical device characterization at room temperature was carried out under ambient conditions. Mobility was evaluated in the saturation regime, at a drain voltage Vd = -60 V.

5.3 Results & Discussion

BTTT dimers were synthesized with various substitution patterns of short C4 (butyl) and long C12 (dodecyl) alkyl chains. **Figure 38** shows the structures of all iterations with two long and two short chains; BTTT-441212, BTTT-124412, BTTT-412124, and BTTT-412412. BTTT-412412 could not be successfully synthesized and purified due to impurities in the precursors. Full synthetic details are available in the appendix.

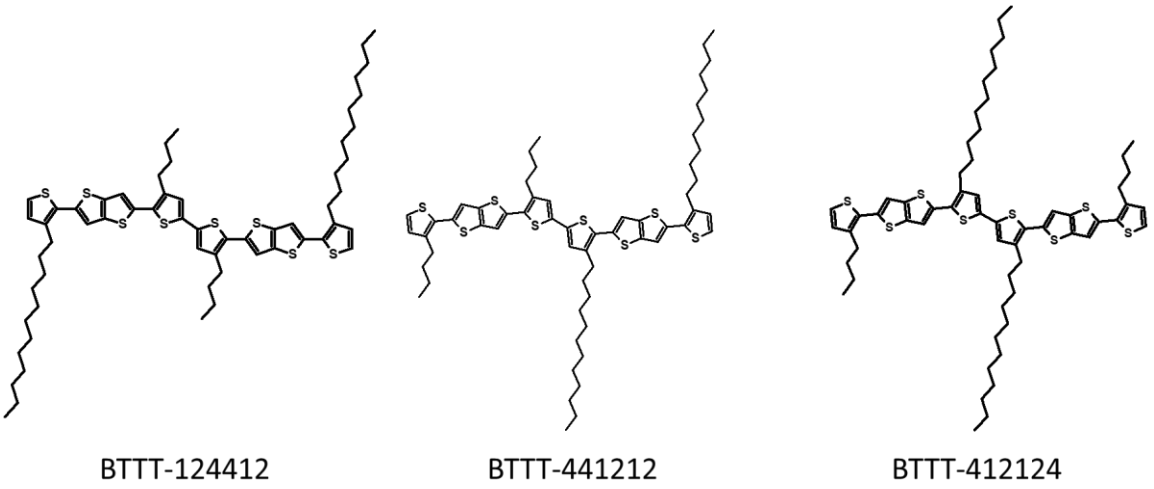

Figure 38 Chemical structures of variable side chain BTTT dimers.

To understand how the substitution pattern effects the self-assembly and morphology of the BTTT dimers in the neat thin film and upon blending with $PC_{61}BM$, GIXD measurements were carried out. As a point of reference, neat BTTT-2-C12 assembles in a lamellar structure with fully interdigitated side chains. The out-of-plane spacing of this molecular packing is 22.0 Å. The GIXD pattern of the BTTT-124412 (**Figure 39**) shows a similar molecular packing to the BTTT-2-C12, a

lamellar structure with a slightly larger out-of-plane spacing of 24 Å. Upon blending with PCBM, no discernable changes to peak position, with a decreased azimuthal distribution, thus an increasing of dimer crystallite texture. A weak halo at Q ~ 1.4 $Å^{-1}$, representative of PCBM aggregates is also present. Indicative of phase separation within this blended film with signatures of crystalline regions for each material. The first phase separation in BTTT dimer/PCBM blends and demonstrating morphological control through modification of side chain length and position.

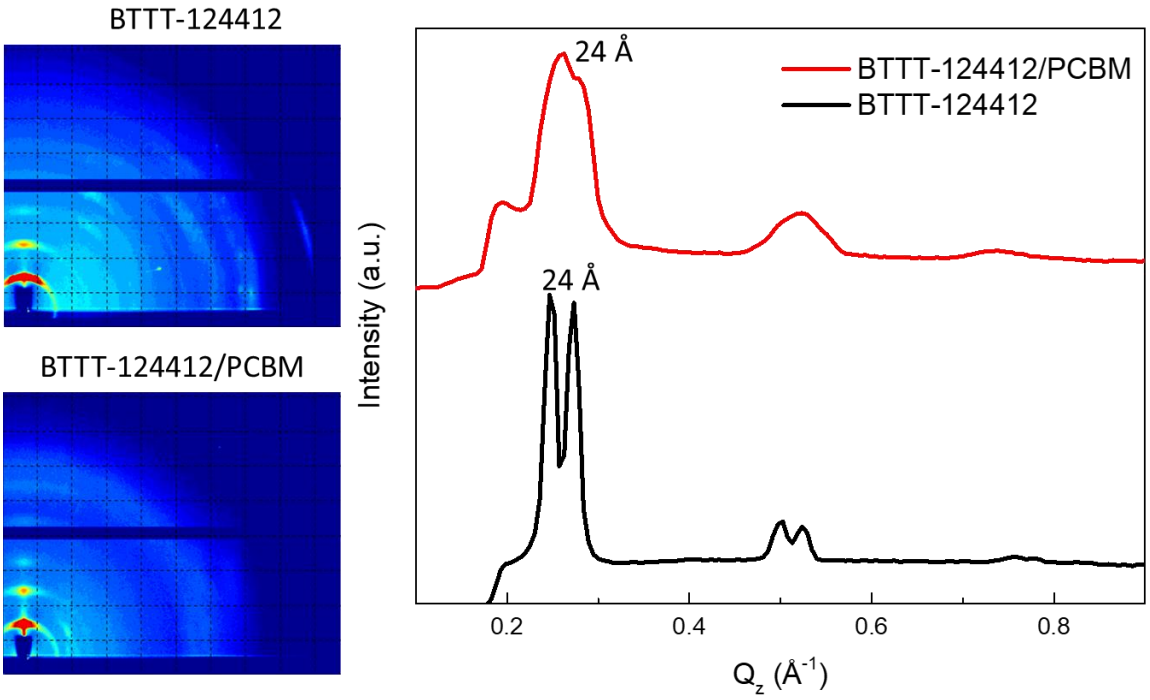

Figure 39 GIXD patterns of (top left) neat BTTT-124412 thin film, (bottom left) BTTT-124412/PCBM blend, and (right) out-of-plane lincuts of neat and blended films, the first demonstration of a phase separated BTTT dimer/fullerene thin film.

The BTTT-441212 diffraction pattern exhibits a film with minimal texture and large peak arching that indicates no preferential crystallite orientation (**Figure 40**). The d-spacing of the dimer was 34 Å, and from the interdigitated BTTT-2-C12 molecular packing corresponded with an out-of-plane spacing of 22 Å and the length of a C12 side chain measuring roughly 12 Å, we can deduce that the BTTT-441212 side chains do not interdigitate, explaining the materials lack of crystalline texture. When blended with PCBM, the diffraction pattern resembles previously

indexed BTTT-2-C12/PCBM films[126], indicating the PCBM intercalate within the BTTT-441212 side chains forming a cocrystal. The blended films out-of-plane spacing decreases to 25.5 Å, the first report of a reduction in lamellar spacing upon fullerene intercalation. This bimolecular crystal's lamellar spacing does match that of the intercalated BTTT-2-C8/PCBM spacing. This is surprising as the spacing was assumed to be dictated by the longer C12 chains shown previously to intercalate. However, C8 is the average chain length between a C4 and C12 component and suggests the chains are registering long-to-short in the cocrystal, as shown in our proposed molecular packing cartoon, **Figure 40c**.

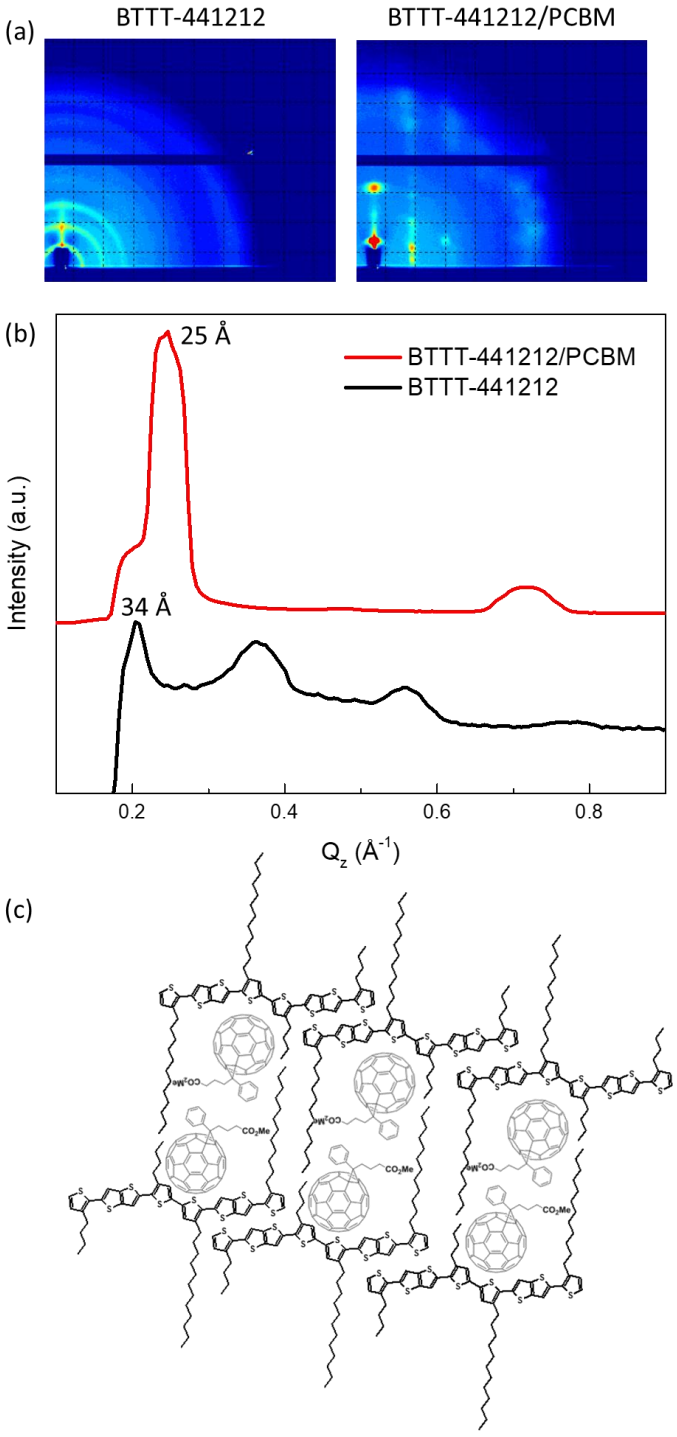

Figure 40 GIXD patterns of (a) neat BTTT-441212 thin film and BTTT-441212/PCBM blend, (b) out-of-plane lincuts of neat and blended films, and (c) the proposed molecular packing of the bimolecular cocrystal.

BTTT-412124 exhibits a highly crystalline diffraction pattern (**Figure 41**), yet demonstrating two competing polymorphs in the as-cast neat film, with lamellar spacing corresponding to 16 Å and 20 Å. Upon annealing at 90 ˚C for 10 minutes, isolation of one polymorph is possible.

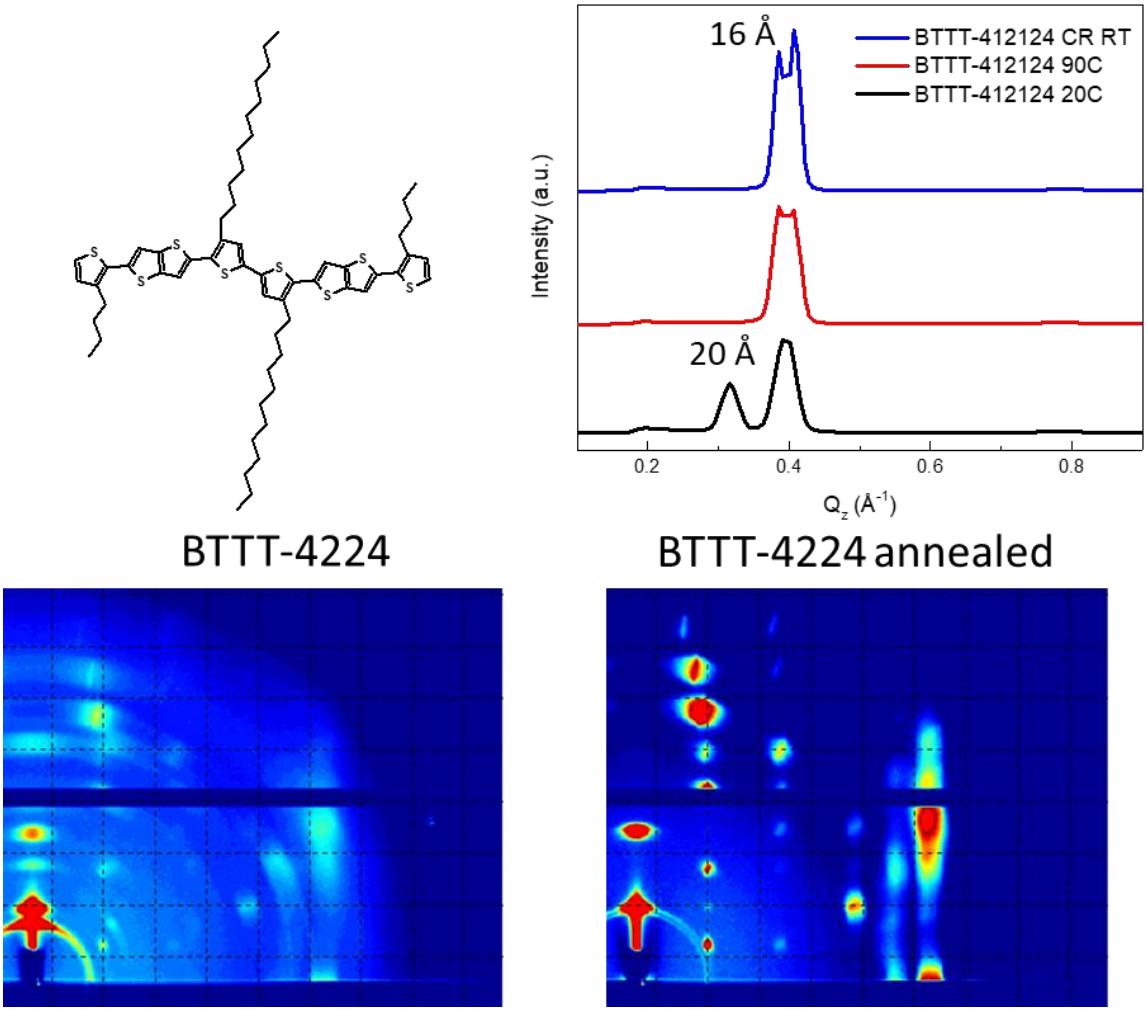

Figure 41 GIXD patterns of (bottom left) neat BTTT-412124 thin film, (bottom right) annealed BTTT-412124, and out-of-plane lincuts of BTTT-412124 before and after annealing, demonstrating the coexistence of two polymorphs in the as cast film and the isolation of a singular molecular packing upon annealing at 90 ˚C.

This isolatable polymorph is identical to the unit cell determined from single crystal x-ray analysis, shown in **Figure 42**, and adopts a very unique molecular arrangement in which the

terminal C4-thiophene is oriented cis relative to the internal C12 thiophene. This conformation allows for increased backbone interaction (3 exposed sulfurs). This is not the standard molecular packing observed for long chain dimers and polymers, BTTT-2-C7 to BTTT-2-C12 adopt a trans arrangement (only 2 exposed sulfurs), however the cis packing is observed in BTTT-2-C6.[170] Shorter alkyl chains do not provide enough Van der Waals interactions to outweigh the increase in favorable backbone interactions. By orienting in the cis confirmation, the rotation of the terminal thiophene allows for increased backbone interactions with neighboring dimers. This driving force is also exemplified in the peculiar conformation of the butyl alkyl groups, adopting a curled arrangement with the 2nd and 3rd methylenes assuming cis conformations. This chain organization allows for butyl chains in nearby molecules to pack in a tighter manner, further increasing the interactions between dimer backbones.

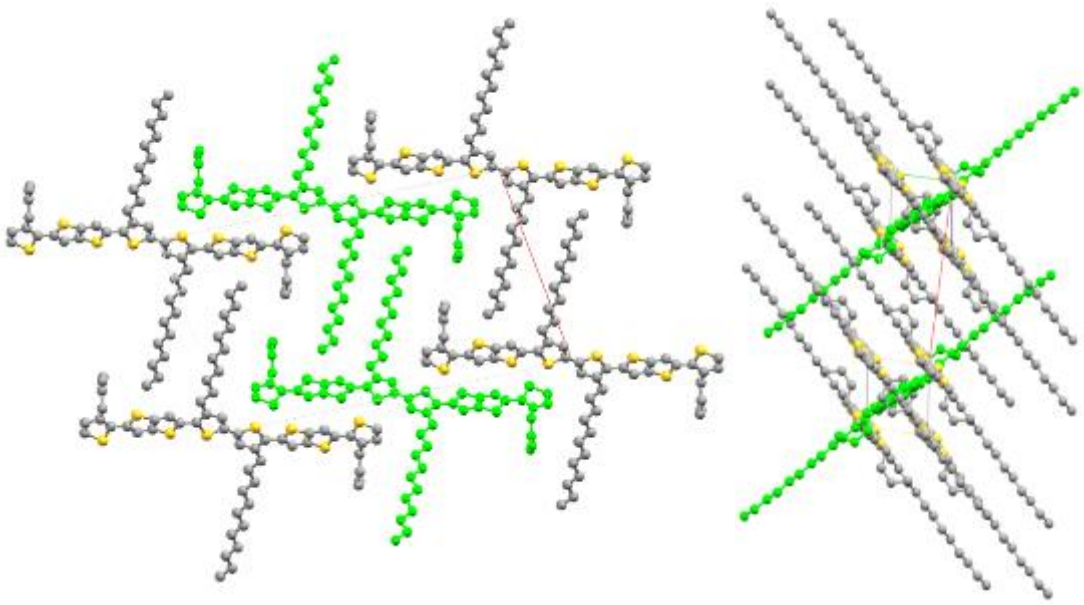

Figure 42 Molecular packing arrangement of BTTT-412124 in the single crystal and in the annealed thin film.

BTTT-412124/PCBM blends demonstrate the formation of a bimolecular crystal. The diffraction pattern exhibits a highly crystalline film, with multiple intense Bragg rods present, with

a lamellar spacing of 25 Å is identical to the BTTT-441212/PCBM cocrystal, further corroborating the proposed packing arrangement in which the C4 and C12 side chains coordinate, **Figure 43**. The proposed molecular packing of this blend is shown as a cartoon in **Figure 43c**. Interesting to note the minimal effect of neat film on blend morphology, as despite polymorphism present in the neat material, only one packing motif upon with the addition of PCBM, previously shown in the side chain length investigation that neat films that exhibit polymorphism only exhibit a singular blending morphology.

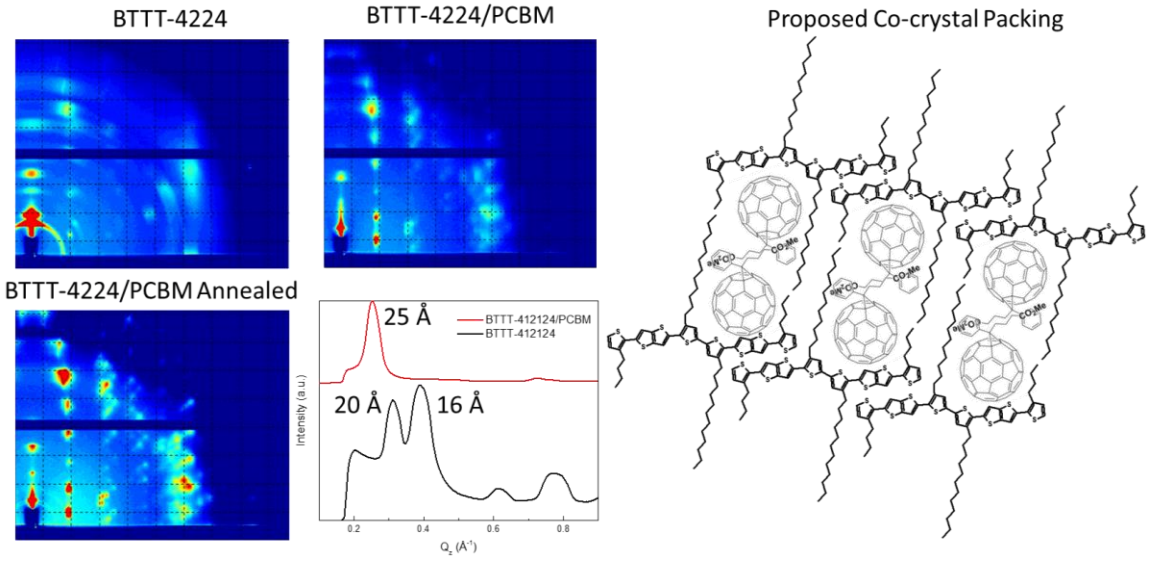

Figure 43 GIXD patterns of neat BTTT-412124 thin film and BTTT-412124/PCBM blend before and after annealing, out-of-plane lincuts of neat and blended films, and (c) the proposed molecular packing of the bimolecular cocrystal.

These X-ray measurements were carried out on films that had been cast and let self-assemble for 14 days. To investigate the time dependence of the structural changes within the variable side chain BTTT dimers and BTTT/fullerene blends, films were cast and held in a vacuum chamber to mitigate any residual solvent effects. The vacuum chamber also prevented any degradation mechanisms that could arise from interactions with oxygen or UV sources.

Figure 44 shows optical microscopy (OM) images of BTTT-124412 as a function of time. After spin coating, the image (0 days) exhibits the formation of a thin film, yet does not exhibit any crystalline features. After 1 day of aging, the images demonstrated large crystalline spherulitic features, roughly 100 µm in diameter. Further aging did not lead to any additional structural changes.

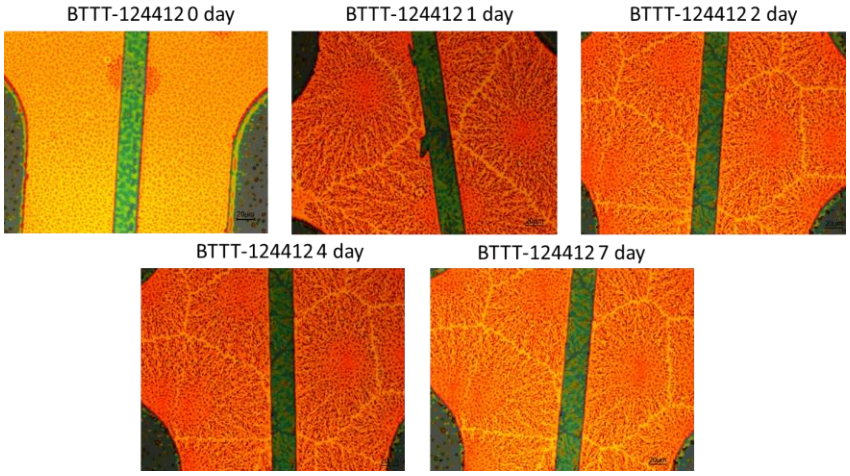

Figure 44 Changes in optical microscopy images of BTTT-124412 as a function of aging time (0, 1, 2 4, and 7 days).

BTTT-412124 (**Figure 45**) images showed very small grain formation immediately upon casting and examination over time did not reveal any major morphology variation.

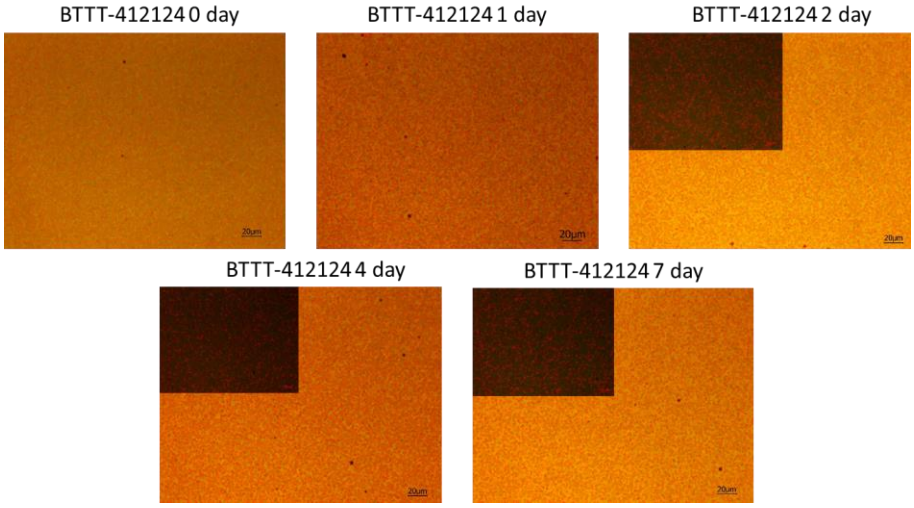

Figure 45 Changes in optical microscopy images of BTTT-412124 as a function of aging time (0, 1, 2 4, and 7 days). Additional OM images were collected using a polarizer and shown as insets for days 2, 4, and 7.

BTTTT-441212 at 0 days (**Figure 46**) showed small, 10 µm circular features that were sporadically located within the film. After 1 day these features completely engulfed the film, yet did not increase in size. Addition aging showed no changes to the film morphology.

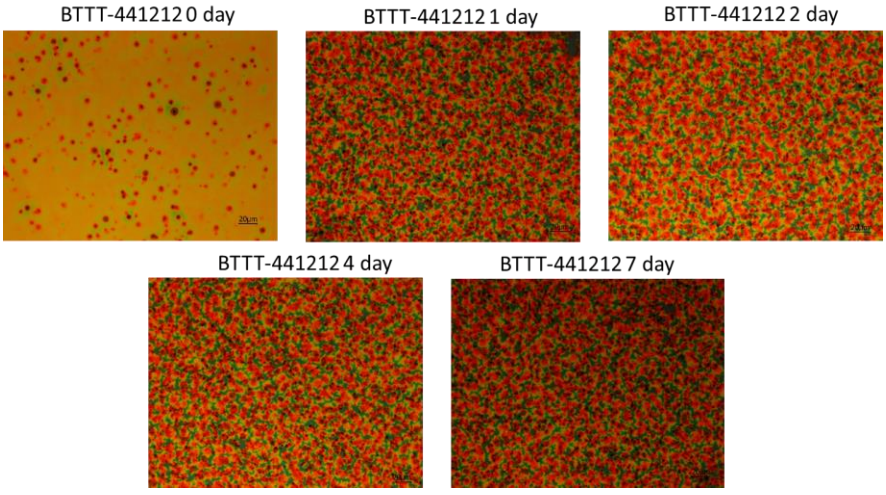

Figure 46 Changes in optical microscopy images of BTTT-441212 as a function of aging time (0, 1, 2 4, and 7 days).

The BTTT-124412/PCBM film, **Figure 47**, had no observable features upon casting (0 days). After 1 day, small, needle-like features about 10 µm in length are present. On day 2, the length and density of these features have increased, with the features roughly 20 µm in length. After 4 days, the aggregates dominate the film, 30 µm in length, and upon additional aging, show no increase in size or density at 7 days. We hypothesize that these features are pure BTTT-124412 aggregates, corroborating the GIXD pattern that indicates that this blend phase separates.

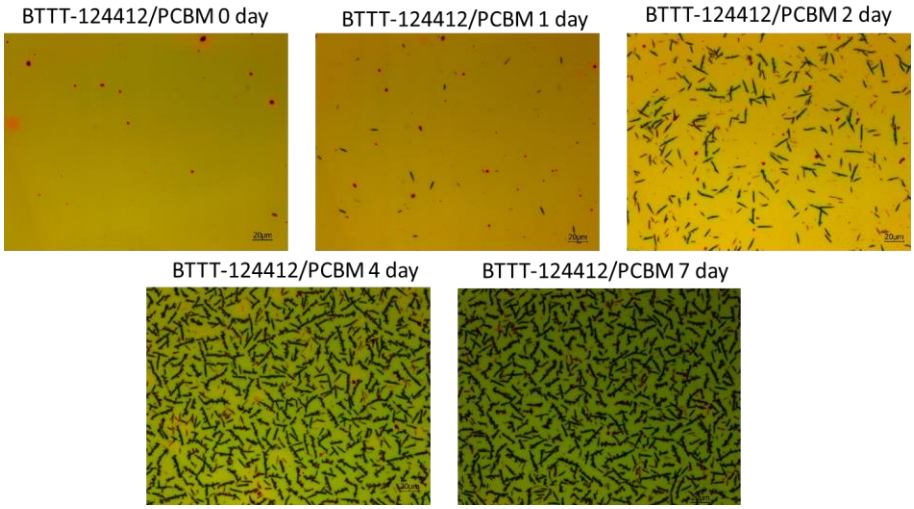

Figure 47 Changes in optical microscopy images of BTTT-124412/PCBM as a function of aging time (0, 1, 2 4, and 7 days).

The BTTT-412124 and BTTT-441212 fullerene (**Figure 48**, **Figure 49**, respectively) blended films exhibit a different aging process. Upon immediately imaging after spin coating, both films have no observable features. Yet after 1 day, the BTTT-412124/PCBM film exhibits crystalline features that can be observed under polarized light. No changes in the film can be seen upon additional aging time.

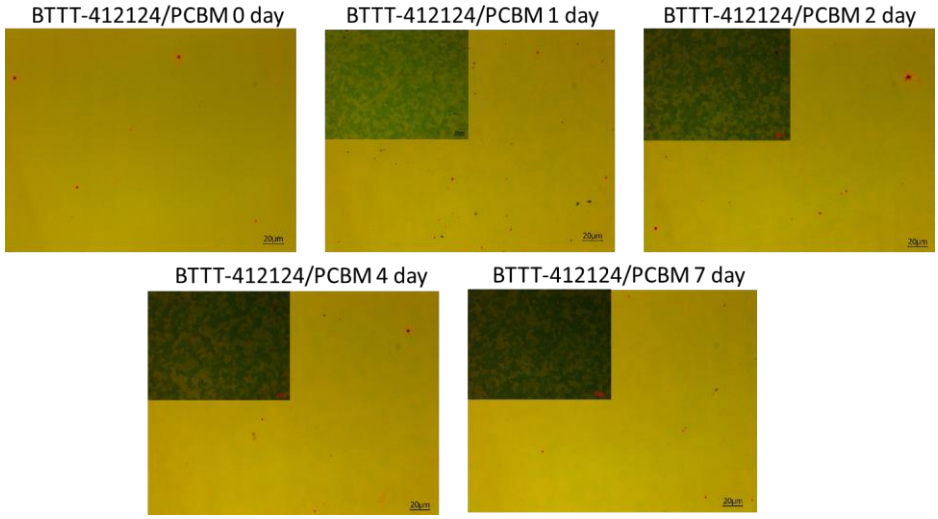

Figure 48 Changes in optical microscopy images of BTTT-412124/PCBM as a function of aging time (0, 1, 2 4, and 7 days). Additional OM images were collected using a polarizer and shown as insets for days 1, 2, 4, and 7.

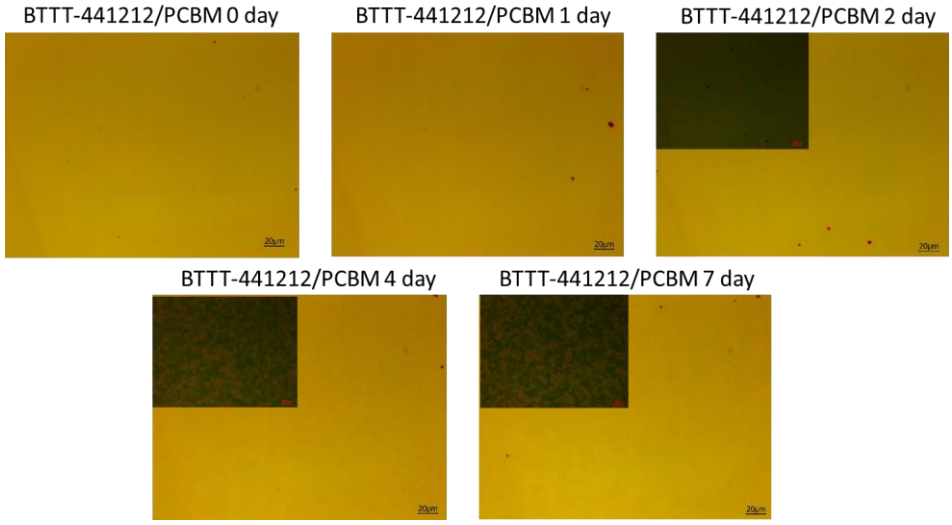

Figure 49 Changes in optical microscopy images of BTTT-441212/PCBM as a function of aging time (0, 1, 2 4, and 7 days). Additional OM images were collected using a polarizer and shown as insets for days 2, 4, and 7.

The BTTT-441212/PCBM film demonstrates the same BTTT-412124/PCBM features, yet their formation takes additional time and are not observable until after 4 days.

These images with similar structural features are in agreement with the GIXD images, yet due to transportation of the films to a synchrotron source, the GIXD measurements were conducted on films that were aged for 14 days. Thus, the morphological picture previously displayed from the GIXD measurements is accurate, but does not demonstrate the structural assembly differences present in the optical images. Comparing the BTTT/PCBM images after 7 days with the GIXD does corroborate phase separation of the BTTT-124412/PCBM film with the formation of pure dimer aggregates. The other two dimer films form an intercalated cocrystal, yet the time scale in which this cocrystal forms does depend on the side chain position, as the BTTT-412124/PCBM film demonstrating a bimolecular cocrystal after 1 day, while the BTTT-441212/PCBM takes 4 days to form the same intercalated features. This difference could be influenced by the asymmetric design of the molecule that could affect the kinetics of the bimolecular crystal formation.

To examine how the self-assembly of these materials and blends influences the absorption spectra, UV-Vis spectroscopy measurements were carried out. The neat films, **Figure 50**, of BTTT-124412 and BTTT-441212 both exhibited similar spectra with peaks centered 438 nm and 323 nm. The BTTT-412124 displayed a red-shifted absorption spectrum with a maximum absorption at 488 nm and a shoulder at 535 nm. After 7 days all three materials exhibited distinct absorption features. The BTTT-124412 has sharp absorbance bands at 557, 514, 484, and 330 nm. The BTTT-441212 film exhibited broadened peaks with a red shift centered at 451 nm and 316 nm. There were minimal changes in the BTTT-412124 film, with a slight feature sharpening.

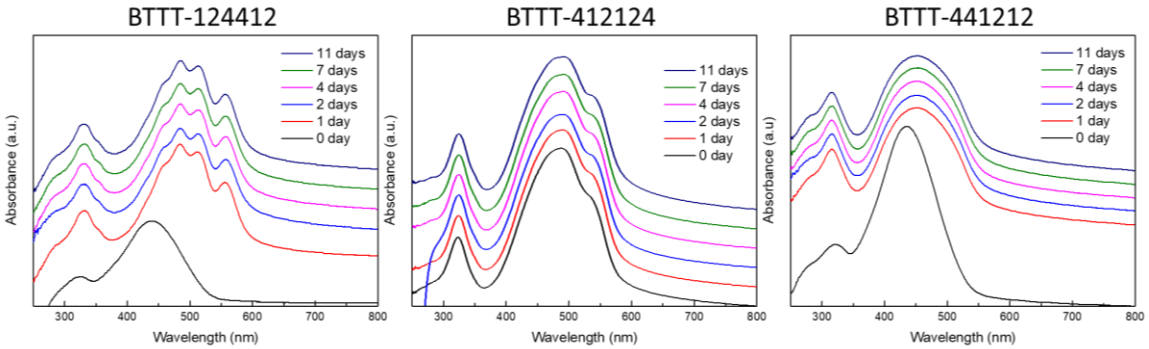

Figure 50 UV-vis spectra of spin coated variable side chain BTTT dimers at different aging times.

Upon blending these BTTT dimers with PCBM, it can be seen in **Figure 51** that immediately after spin coating, the films have nearly identical absorption profiles, with dominate peaks at 442, 333, and 265 nm, resembling the optical microscopy trend in which all blends had no distinguishable features upon casting. As the films were monitored over time, different features began to appear, with the BTTT-124412/PCBM blend exhibiting correspondent peak to the neat BTTT-124412 absorption after 2 days. The BTTT-412124/PCBM and BTTT-441212/PCBM did not show any neat dimer associated peaks, but did develop a new peak at 310 nm. The only differences being the kinetics of the peak formation, as the BTTT-412124/PCBM blend showed development after 1 day and little variation in the profile upon additional aging. The BTTT-441212/PCBM profile develops slower, with small variation tracked over time until a maximum reached after 4 days. These absorption changes verify the morphological changes in which BTTT-124412 does not allow fullerene intercalation seen from the development of peaks associated with the neat absorption profile in the blended films. The BTTT-412124 and BTTT-441212 both exhibiting the same absorption profile upon blended with PCBM also fortifies the argument that these materials do form a bimolecular cocrystal.

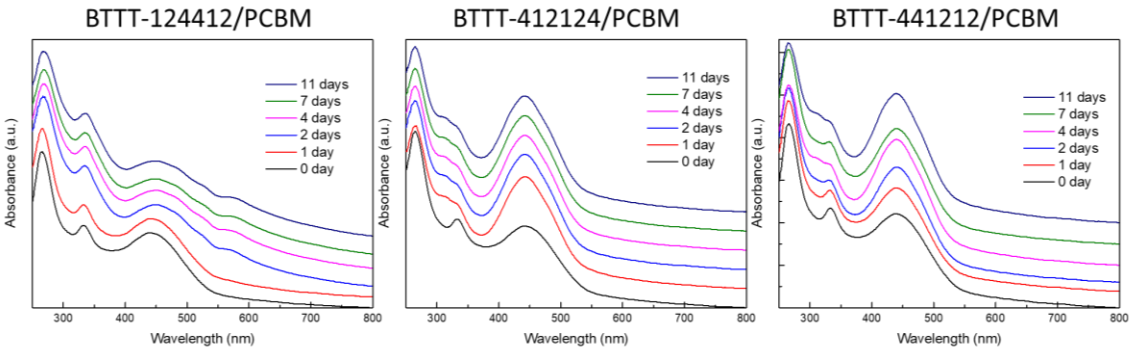

Figure 51 UV-vis spectra of spin coated variable side chain BTTT dimer/fullerene blends at different aging times.

To examine the morphological and self-assembly influences on the materials charge transport properties, field-effect transistors were fabricated and measured over a period of 14 days, shown in **Figure 52**. Upon casting, BTTT-124412 exhibited a low mobility of 1.75×10^{-6} cm^2/Vs, yet after 1 day the mobility improved by two orders of magnitude to 5.1×10^{-4} cm^2/Vs and stabilized upon further aging. This mobility improvement can be attributed to the self-assembly of this material previously tracked with OM and UV-Vis spectroscopy. The BTTT-412124 film exhibited a mobility of 1.9×10^{-4} cm^2/Vs immediately upon spin coating and remained constant upon additional aging, reflecting the highly crystalline GIXD pattern and stable absorption profile. The BTTT-441212 did not display any field effect immediately after spin coating, and after 1 day of aging, demonstrated a low mobility of 1.9×10^{-7} cm^2/Vs. This mobility did not change after repeated measurements with additional aging time. The time-dependent mobility behavior mirrors the UV-Vis and OM images which exhibited large changes in the absorption profile and film structure after 1 day. The low mobility can be attributed to the molecular packing, the GIXD demonstrating the side chains do not interdigitate and

possess minimal texture, resulting in very little order within the film that hinders charge transport.

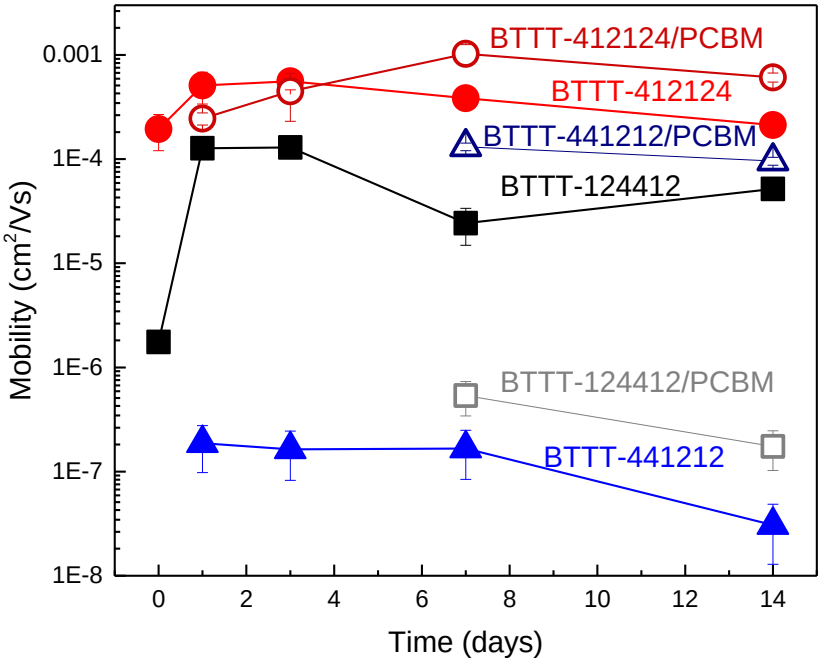

Figure 52 Changes in field-effect mobility of neat dimers and dimer/fullerene blends as a function of aging time.

None of the BTTT/PCBM blends exhibit any field effect immediately after spin coating, as no films exhibiting ordering upon this time scale, given the identical featureless OM images and absorption profiles. After 1 day, the BTTT-4224/PCBM blend has a mobility of 2.5×10^{-4} cm^2/Vs, further increasing to above 1.0×10^{-3} cm^2/Vs after 7 days. This high mobility can be attributed to intercalation of PCBM within the side chains of the dimer, which enables the BTTT-412124 to pack without competing polymorphs, large twist between dimer units, and forced cis conformation of the side chains that could impede charge movement through the thiophenes. The BTTT-124412 and BTTT-441212 do not exhibit any field effect until 7 days, the BTTT-124412/PCBM film displaying a low mobility of 5.4×10^{-7} cm^2/Vs. This slow film development and low mobility can be

attributed to the phase separation process that was monitored with OM and UV-Vis, measured with GIXD. The mobility measurements corroborate the hypothesis that the needle-like features developing in the optical images were BTTT-124412 aggregates, as no hole mobility is measured until 7 days, in which the needle features are larger than the channel length of 20 μm. The blend mobility is two orders of magnitude lower than the neat dimer film, as the PCBM impedes the crystallization of the BTTT-124412, which relies on large crystalline aggregates to transport charge, as inter-aggregate transport is heavily limited in oligomers that cannot rely on tie lines present in polymer systems. The BTTT-441212/PCBM blend also exhibit no field effect until 7 days, however the mobility is measured at 1.3×10^{-4} cm^2/Vs, three orders of magnitude higher than the neat material. The slow self-assembly of this film can be attributed to the unique proposed molecular packing of the cocrystal, which did not show exhibit full formation with UV-Vis and OM until 7 days. The mobility improvement due to the PCBM catalyzing the BTTT-441212 crystallinity and pack in a more effective manner. The PCBM intercalation, results in a coordination of the C4 and C12 side chains, and this slight side chain interdigitation increases crystallinity and transport of charge compared to the non-interdigitated neat film packing.

To understand these materials room temperature self-assembly properties, their thermal behavior was measured by DSC and thermograms are shown in **Figure 53**. BTTT-124412 shows a broad and weak melting peak at 72 ˚C, indicating a large distribution in crystalline size and quality. BTTT-441212 also demonstrates a similar behavior, with a slightly higher melting point of 86 ˚C. It is surprising that the asymmetric dimer has a higher melting transition. An absence of any crystallization or melting peak for both of these materials upon cooling or a secondary heating ramp indicates that the self-

organization of crystalline domains is kinetically limited. The BTTT-412124 demonstrates the highest melting temperature of the variable BTTT dimers, with a single reproducible endothermic peak at 103 ˚C. This transition is still slightly lower than the BTTT-2-C12, which could be caused by the differing backbone orientation and fewer side chain interactions. These measurements can help explain the self-organization of these materials at room temperature, as the slowest assembling materials, the BTTT-124412 and BTTT-441212 both exhibit very low melting temperatures and difficulty to form crystalline domains, thus require a large amount of time to assemble, yet enough thermal energy is provided at room temperature to allow for molecular rearrangement.

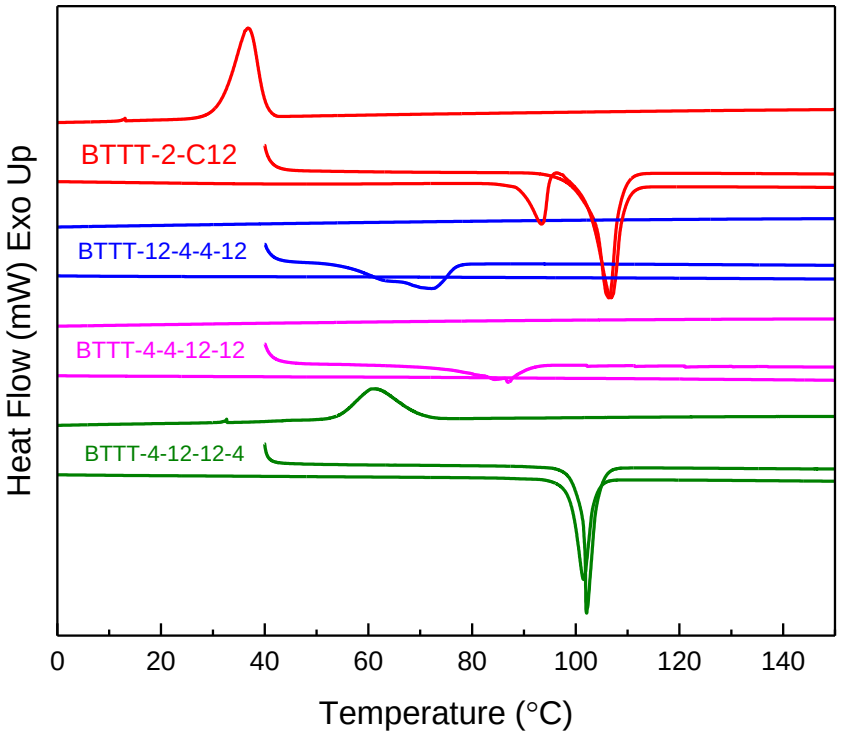

Figure 53 Heating and cooling thermal thermograms of variable side chain BTTT dimers and BTTT-C12 and BTTT-C4 included for reference.

5.4 Conclusion

In conclusion, this study explores the effect of side chain position on the molecular packing of BTTT dimers and interaction with PCBM without pocket dimensional modifications (every pocket consists of one C4 and C12 chain). Side chain position has a large influence on the assembly of the materials with unique BTTT morphologies in the thin film and PCBM blends. The asymmetric BTTT-441212 did not allow for side chain interdigitation, resulting in a non-textured film with low mobility. BTTT-124412 formed a phase separated system upon blending with PCBM, the first demonstration of phase separation within the BTTT dimer family. These side chain position modification effects on the morphology and self-assembly of these materials was measured as a function of time using OM, UV-Vis spectroscopy, and transistors and all corroborate our morphologic self-assembly model.

An interesting distinction and clue into what could cause these large differences in film morphology of the blended BTTT/PCBM films could be the length of the interior side chains. As the BTTT-412124 and BTTT-441212, which exhibit bimolecular crystal formation, both have interior C12 side chains. Also contributing to this hypothesis of the necessity of longer interior side chains is the differences in the time dependent formation of the cocrystals, as the BTTT-412124, which has two interior long side chains, demonstrates a more rapid cocrystal formation after 1 day, compared to the BTTT-441212, which has one interior C12 chain, and does not form a cocrystal until 4 days, thus requiring much more time to form this morphology. BTTT-124412, which possesses no long interior side chain does not intercalate. This phenomenon could be caused by the interior side chains having less rotational freedom then the terminal positions, thus providing a more rigid pocket to allow for the intercalation of PCBM.

Another possible explanation for the differing morphologies could be the competition between the cis and trans conformation of the BTTT dimers. The only single crystal analysis demonstrates that these materials can adopt an energetically favorable cis conformation. The BTTT-124412, which does not intercalate, could be arranged in a cis conformation, **Figure 54**, thus reducing the pocket size and disallowing fullerene intercalation. Why this is the case for just the BTTT-124412 and not the other dimers, which adopt the trans conformation to allow for intercalation, is not understood at present and would require additional computation calculation and collaboration.

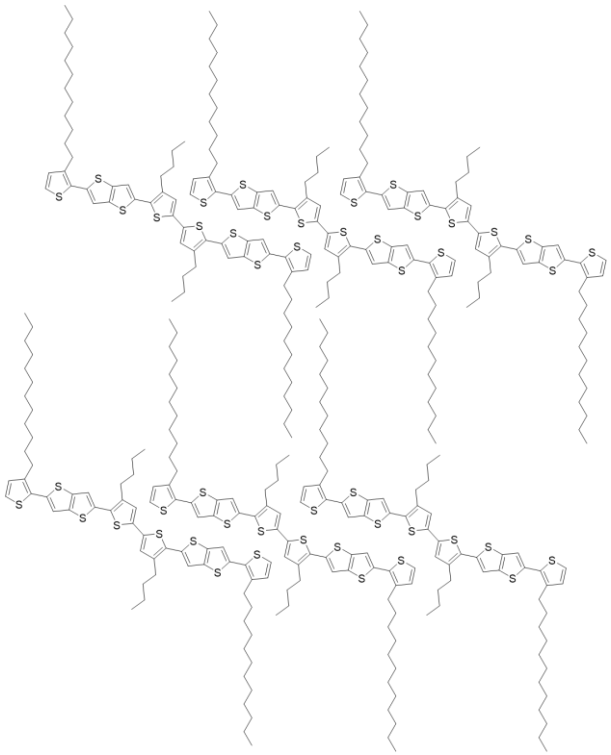

Figure 54 Possible cis molecular packing of BTTT-124412 in the neat and blended film that disallows fullerene intercalation.

This study further elaborates the factors governing intercalation, demonstrating that pocket position also influences the intercalation of fullerenes into donor systems,

but also expands the morphologic control of donor/acceptor systems design rules, paramount for the advancement of flexible conductive materials and thermoelectrics.

5.5 Acknowledgments

We thank Ben Cherniawski for the synthesis of the materials. Prof. Sean Parkin for the single crystal determination of the BTTT-412124.

CHAPTER 6

EXPLORING SMALL MOLECULE/DOPANT INTERACTIONS WITH VARIED DOPANTS

6.1 Introduction

The discovery that the addition of impurity atoms doped inorganic semiconductors allowed for the implementation and functionality of modern electronic devices. The process allowed for precise interfacial band alignment control and the fabrication of highly conductive materials though minimal necessary dopant additives, as the covalent nature of these additions resulted in highly efficient doping and the formation of free carrier.[32] If To reach the same level of implementation of organic semiconductors as its inorganic counterpart, than its doping process must be as understood and controllable.[38]

Early research into the doping of organic semiconductors hoped to mimic that of inorganic semiconductors through the introduction of atomic alkali metals or halides[34,35], and although very conductivities were reached, the noncovalent doping proved more difficult and device inappropriate due to their ease of diffusion. To decrease the diffusivity of the dopants, molecular electrical doping has emerged as a more promising candidate for device application[38], employing strong molecular acceptors for p-type doping[42,45] and donors for n-type doping[193-196]. Energy level tuning through chemical modification allows for molecular dopants to be designed such that, for p-type doping, their electron affinity (EA) is in the range of the ionization energy (IE) of the OSC, and conversely for n-type doping.[48] These high conductivity films have a large demand as hole or electron conducting interlayers in organic light-emitting diodes, organic photovoltaic cells, organic field-effect transistors, and thermoelectrics.

The most extensively studied organic semiconductor/dopant combination has been polythiophenes/tetracyanoquinodimethane (TCNQ) derivatives.[169,197-203] Polythiophenes due to their high mobility and extensive application in transistors and solar cells and TCNQ derivative as

p-type dopants due to their ideal energy levels for charge transfer, the most commonly used material being F4TCNQ. Yet, performance and morphology are shown to be heavily processing dependent, exhibited in **Figure 55**. The first processing technique for the fabrication of high conductivity films was spin coating a blended solution of polymer/dopant. This method led to moderate conductivities of ~1 S/cm with P3HT and PBTTT[197,198]. Yet, in both cases the F4TCNQ molecules were found to arrange within the polymer backbone, disrupting the pi-pi interactions that govern charge transport through the polymer, limiting conductivity. These conductivity values were improved upon through the implementation of a two-step process in which a PBTTT film was first spin coated, allowing for the formation of a high mobility polymer film, sequentially a F4TCNQ layer was thermally evaporated onto the film.[169] The molecules fully penetrated the polymer film due to solid state diffusion From X-ray measurements, the evaporated F4TCNQ slightly increased the out-of-plane spacing, did not disrupt the pi-pi stacking, and increased the crystallinity of the film, as the authors presumed that F4TCNQ molecules arranged within the side chains of the polymer. This sequential processing technique and differing morphology was shown to improve the overall conductivity, reaching values over ~200 S/cm.

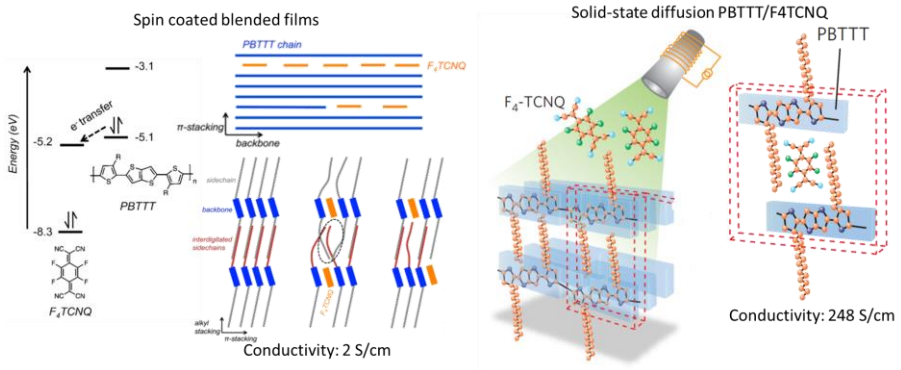

Figure 55 Cartoon representation of the effect of processing conditions on PBTTT/F4TCNQ morphology. The blended spin coated film (left) exhibited modest conductivity values and the F4TCNQ molecules residing within the polymer backbone. The thermal evaporation of F4TCNQ (right) onto a previously cast PBTTT and through solid-state diffusion the dopant molecular arrange within the polymer side chains, leading to a larger increase in conductivity. Reprinted from ref. 195 and 167.

Although this paper provided a powerful example of morphologic control through the proper film processing techniques, if high conductivity organic films are to be commercialized at low costs, a one-step, solution-based processing condition is a necessity.

The standard methodology for p-doping of using a high mobility polymer and blending with the benchmark F4TCNQ seems to be nearing a plateau, as these blends have not led to large breakthroughs in conductivity values. Yet, these materials can be chemically modified to improve and control the semiconductor/dopant interactions and morphology. Tailoring side chains to increase the polymers miscibility with dopants[204-207] has led to increase in conductivity using a gycolated polythiophene derivative that allowed for larger dopant loading.[204] Another system used PQT as a benchmark system and demonstrated through modification to the side chains or backbone can tailor the position of the dopant within the blended film, resulting in the highest one-step non-ionic conductivity measurements to date, **Figure 56**.[208]

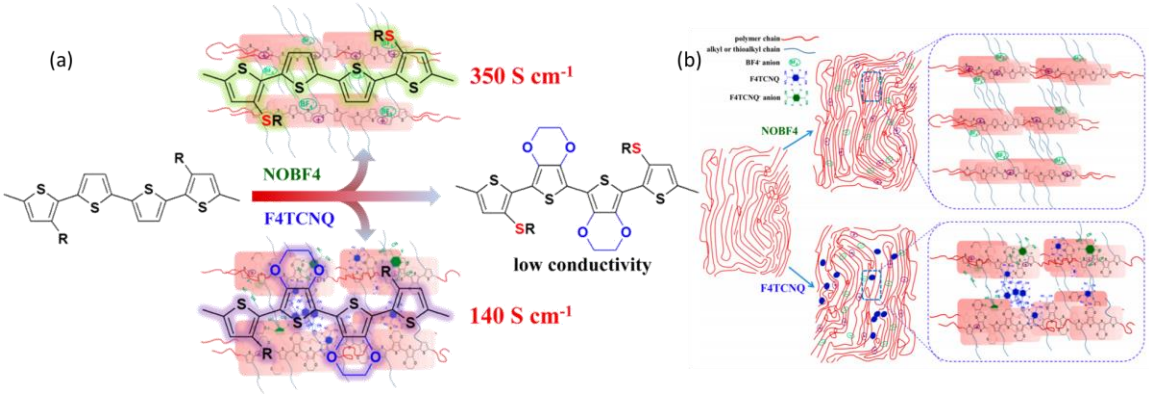

Figure 56 (a) Synthesized structurally modified poly(disdocdecylquaterthiophene) (PQT12) to increase oxidizability. Through correct dopant choice, record nonionic conductivities were reached. (b) Illustration of doping process and packing models doped by NOBF4 and F4TCNQ, respectively showing the strong interactions of the $BF4^-$ anions with the polymer side chains and $F4TCNQ^-$ anions with the polymer backbone. Reprinted from ref. 206.

To push to higher conductivities, structure-property relations must be established to understand the possible morphologies available in these blended semiconductor/dopant films, identify the higher conductivities, and tune the chemical structures of the semiconductor or dopant to control the morphology. These design rules are especially lacking for doping small molecule organic semiconductors, which have been seen to be governed by a different doping mechanism, charge transfer hybridization. In this study, we will use a model BTTT dimer, which has previously shown to be an excellent small molecule model system of its parent polymer, with similar molecular packing and cocrystal formation with fullerenes.[126] We explore the effect of dopant type by comparing TCNQ derivatives and metal complexes. UV-Vis-NIR measurements reveal differing absorption signatures, yet no anion or polaron peaks were present in most blends, with a possible ion-pair formation using F6TCNNQ, concluding a majority that these organic semiconductor/dopant blends are governed by a charge transfer hybridization mechanism.[50] A six-orders of magnitude increase in conductivity was measured upon the addition of metal complex dopants compared to a modest conductivity increase with TCNQ blended films. A morphological comparison revealed the F4TCNQ molecules pack within the BTTT backbone while the metal complexes intercalate within the side chains of the dimer. This study demonstrates the dopant choice as another tunable handle to vary the morphology of the OSC/dopant blends and increase conductivity.

6.2 Experimental

BTTT-C12 dimer was synthesized with further details available in literature.[126] F4TCNQ was purchased from Ossilla. F6TCNNQ, $Mo(tfd)_3$, and $Ni(tfd)_2$ were synthesized and received from the Marder group at Georgia Tech. All solvents were purchased from Sigma Aldrich and used as received.

Thin films for structural analysis as well as electronic characterization were fabricated by dissolving BTTT dimers and/or dopants in chloroform (1 mg/ml) separately and then mixing in solution directly before spin coating at 1500 rpm for 60 seconds.

Ultraviolet-visible-near infrared (UV-vis-NIR) spectroscopy was performed using a Shimadza 3600 UV-VIS-NIR spectrophotometer. Absorption spectrum were measured in the thin film spin coated from chloroform solutions.

Grazing incidence wide-angle x-ray scattering (GIWAXS) measurements were carried out at D-line (Cornell High Energy Synchrotron Source). A 0.5 × 0.1 mm beam with a wavelength of 1.23 Å and wide band pass (1.47%) was generated from double-bounce multilayer monochromator. The incidence angle was 0.15° with respect to the substrate plane.

Device Fabrication and Characterization: Two-probe conductivity measurements were done using Si wafers with thermally grown SiO2 (300 nm thick) prepatterned with 50 nm Au bottom contacts. Channel dimensions of 300 μm and 20 μm for the width and length, respectively, were used. The substrates were sonicated in deionized water and soap, acetone, isopropanol, and deionized water and dried with nitrogen. Substrates were then exposed to UV-ozone treatment for 15 minutes. Electrical device characterization at room temperature was carried out under ambient conditions.

6.3 Results & Discussion

The conductivity of solution-processed, molecularly-doped organic semiconductors has a large dependence on the morphology of the blended film. In this study we investigate the doping of dimer, BTTT-C12, of PBTTT, a small molecule of interest due to thin film packing and unique interactions with fullerenes representative of its parent polymer. We also investigate the effect of dopant on the conductivity and morphology by using two families of dopants, conjugated

benchmark materials, F4TCNQ and F6TCNNQ, and metal complexes, $Ni(tfd)_2$ and $Mo(tfd)_3$, chemical structures shown in **Figure 57**.[209-211]

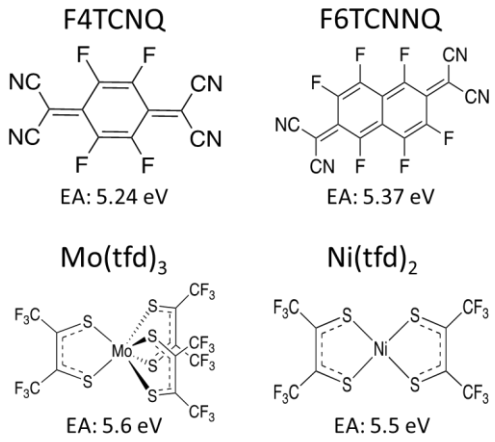

Figure 57 Chemical structures of the dopant molecules used in this study.

To investigate the effect the addition of molecular dopants on the absorption profile of BTTT-C12, UV-Vis-NIR measurements were carried out. The neutral BTTT-C12 displays a prominent peak at 455 nm. Upon loading of F4TCNQ, **Figure 58**, a bleaching of this peak is present with the rise of sub-bandgap features, indicative of doping. Yet, these features are centered 587 nm and 941 nm, which are not correspondent to a F4TCNQ anion, which displays features at 765 nm and 855 nm. Thus, no ion-pair formation is present in BTTT/F4TCNQ blends, indicating that these features arise from a charge-transfer complex formation between these materials, contrary to the polymer/dopant profile.

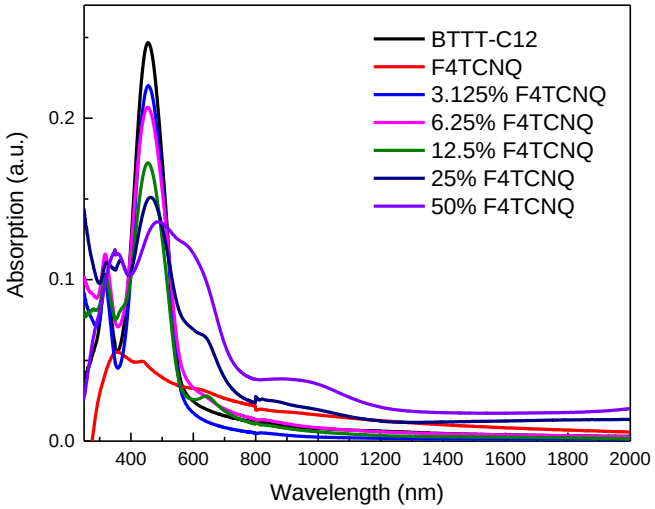

Figure 58 Absorption spectra of BTTT-C12 blended with F4TCNQ at increasing ratio.

In the F6TCNNQ blended films, a reduction of the neutral BTTT-C12 peak and formation of sub bandgap features is shown in **Figure 59**, with two slight peaks at 996 nm and 1169 nm, very similar to the anion peaks of F6TCNNQ, but very weak compared to benchmark ion-pair formation blends. The increase in absorption intensity in the NIR region could also be associated with a positive polaron of BTTT-C12.

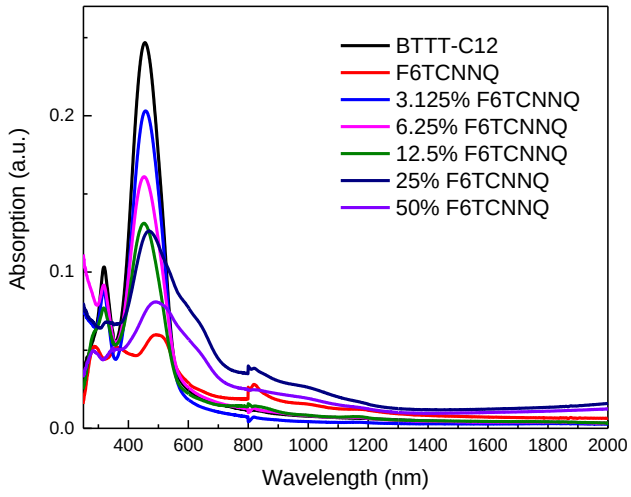

Figure 59 Absorption spectra of BTTT-C12 blended with F6TCNNQ at increasing ratio.

The difference in the signatures between F4TCNQ and F6TCNNQ could arise from the mechanism of ion pair formation, as in the case of p-type doping, the energetic offset of the electron affinity of dopant and ionization energy of the organic semiconductor the driving force of electron transfer. F6TCNNQ is a stronger dopant than F4TCNQ with a higher electron affinity, so this increased energetic offset for F6TCNNQ/BTTT-C12 could form a dopant anion and an organic semiconductor cation. The fact that an ion pair forms in the PBTTT/F4TCNQ blend and not in the BTTT-C12/F4TCNQ may be related to the slight difference in the ionization energies of the BTTT materials, PBTTT of 5.1 eV and BTTT-C12 of 5.3 eV. When blended with F4TCNQ, with an electron affinity of 5.2 eV, there is not the ideal offset for electron transfer in the BTTT-C12 blends that is present in the PBTTT. Yet, upon blending BTTT-C12 with F6TCNNQ, which has higher electron affinity of 5.4 eV, the offset is enough for features of dopant anion and dimer polaron formation to be present.

The blended films of BTTT-C12 with the metal complexes (**Figure 60**, **Figure 61**) exhibit very different absorption profiles from the TCNQ dopants, with a stronger reduction of the neutral dimer peak and the formation of intense peaks in the NIR, similar to the peak formed in 4T/F4TCNQ blends that was verified to be a ground state charge transfer complex.[49]

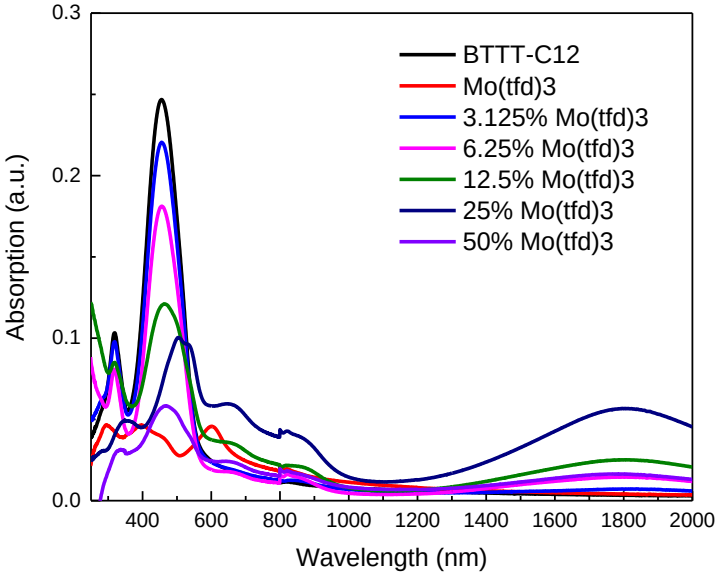

Figure 60 Absorption spectra of BTTT-C12 blended with $Mo(tfd)_3$ at increasing ratio.

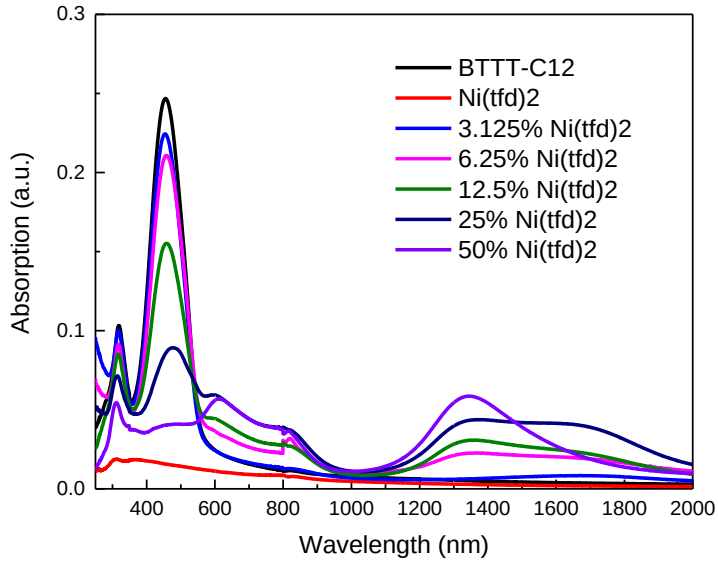

Figure 61 Absorption spectra of BTTT-C12 blended with $Ni(tfd)_2$ at increasing ratio.

To further understand the charge transport properties of these blended films, conductivity measurements were carried out as a function of doping concentration, as shown in **Figure 62**. The BTTT-C12 exhibits a very low inherent conductivity of 7.5×10^{-9} S/cm and displayed

very differing conductivity behavior dependent on the dopant choice. The TCNQ-based dopants showed modest conductivity increase with a maximum value of ~1 x 10^{-6} S/cm for both F4TCNQ and F6TCNNQ at 12.5% MW loading. This is unexpected, as F6TCNNQ is the stronger dopant, yet could be limited due to a decreased solubility. The metal complex dopants display a very different conductivity behavior than the TCNQ dopants, with $Mo(tfd)_3$ increasing conductivity by over six orders of magnitude, similar to the solid-state dopant study of PBTTT/F4TCNQ by Sirringhaus and coworkers. The metal complexes also allow for higher dopant loading without disrupting conductivity, with the peak values at 25% MW.

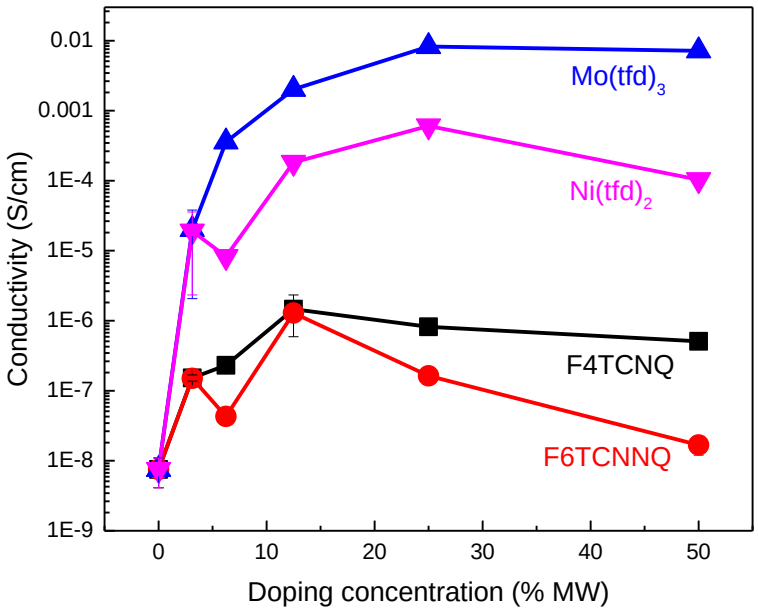

Figure 62 Lateral thin-film conductivity as a function of dopant ratio for films of BTTT-C12 dimer with various dopants.

To investigate if this dopant-dependent conductivity values is morphologically related, grazing-incidence wide-angle x-ray scattering measurements were carried out to determine the changes in molecular packing of BTTT-C12 upon the introduction of each dopant. The neat BTTT-C12 arranges in an edge-on orientation with an out-of-plane lamellar spacing of 22 Å with interdigitated side chains previously characterized in detail. At low loading concentrations of

F4TCNQ (6.25% MW), there is a slight decrease in out-of-plane scattering intensity (**Figure 63**), with no changes in peak position. The in-plane pi-pi stacking peak is shown to be completely quenched, indicating that the F4TCNQ disrupts the interlayer backbone interactions. At 25% F4TCNQ blends, there is a noticeable out-of-plane spacing decrease to 18.5 Å. Although insufficient diffraction spots for unit cell determination or molecular packing, this decrease in out-of-plane spacing resembles BTBT/F4TCNQ blends, in which the dopant molecules coordinate with the conjugated backbone, causing a large side chain rearrangement, reducing the lamellar spacing.[51]

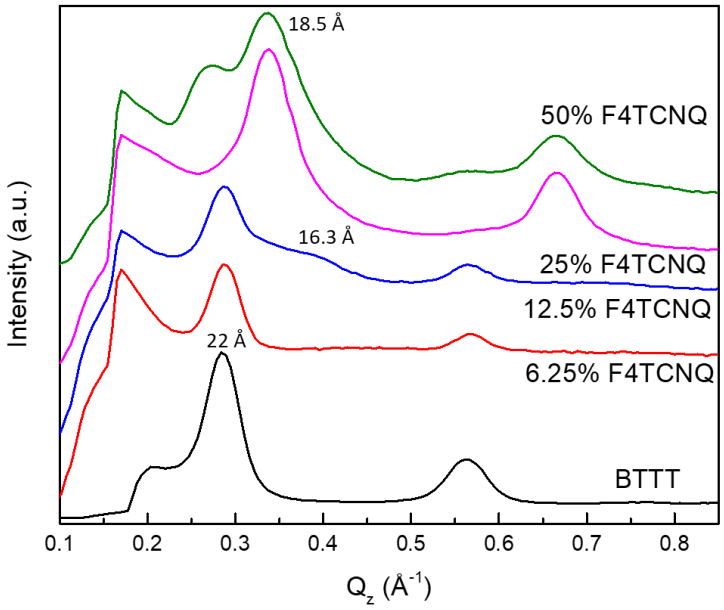

Figure 63 GIXD measurements and out-of-plane linecuts of pure BTTT-C12 and increasingly doped BTTT-C12/F4TCNQ blends.

BTTT-C12 blends with F6TCNNQ exhibit a similar morphological behavior, **Figure 64**, in which the pi-pi stacking order is severely disrupted at low dopant loading ratios. At 25% F6TCNNQ doping, the lamellar spacing slightly shrinks to 20.5 Å. This similar behavior at high dopant loading to F4TCNQ indicates that they pack in a similar manner, with the variation in lamellar spacing attributed to the differences in molecular dopant size.

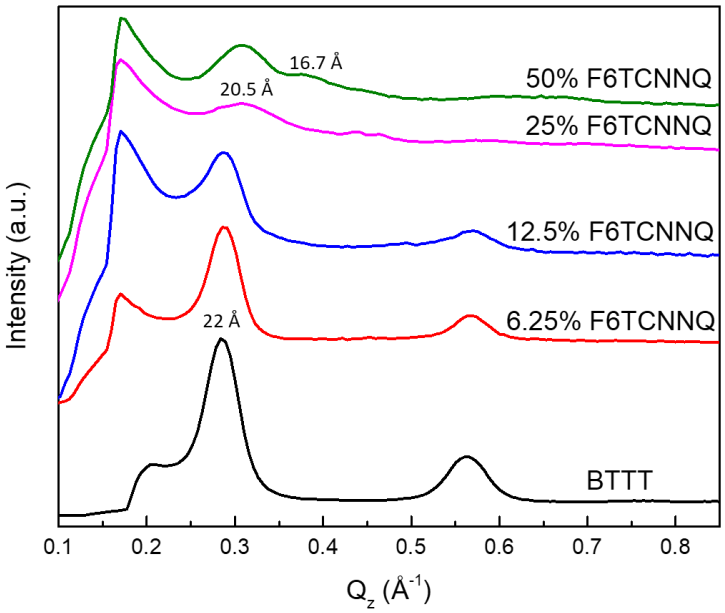

Figure 64 GIXD measurements and out-of-plane linecuts of pure BTTT-C12 and increasingly doped BTTT-C12/F6TCNNQ blends.

BTTT-C12/$Mo(tfd)_3$ blends display a differing morphology behavior, **Figure 65**, with the appearance of a new out-of-plane peak corresponding to 32.9 Å at 25% doping MW. This increase in lamellar spacing is much larger than previous PBTTT/F4TCNQ sequential evaporated films, which caused an increase of 2 Å upon dopant deposition and diffusion. They proposed a molecular packing structure of a single F4TCNQ molecule intercalated within the side chains of the polymer. In the BTTT-C12/$Mo(tfd)_3$ system, this increase of 10.9 Å is similar to previous BTTT-C12/PCBM blends[126] in which two fullerene molecules pack within the side chains of the dimer, disallowing side chain interdigitation. Despite a large investigation into possible small molecule intercalates with PBTTT, this is the first non-fullerene to exhibit this large out-of-plane spacing expanded cocrystal.

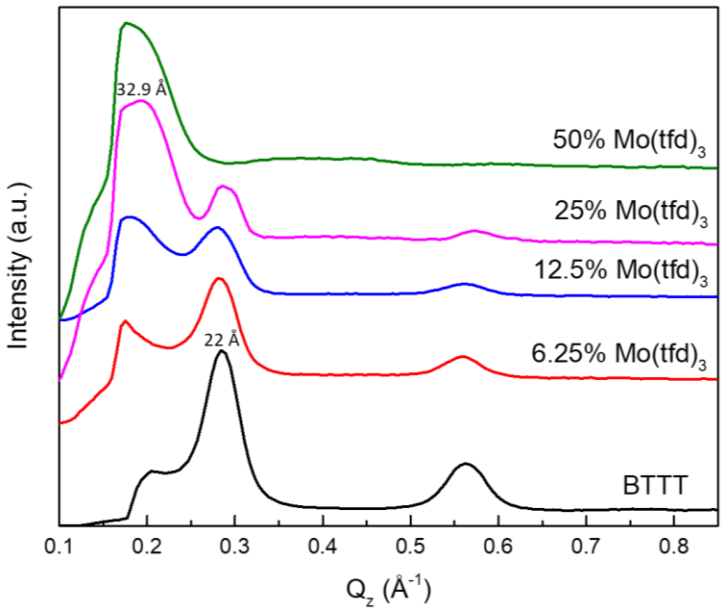

Figure 65 GIXD measurements and out-of-plane linecuts of pure BTTT-C12 and increasingly doped BTTT-C12/$Mo(tfd)_3$ blends.

The molecular packing of $Ni(tfd)_2$ doped films follow a similar trend, **Figure 66**, with a new peak forming along the q_z axis corresponding to a d-spacing of 29.6 Å. This peak does arise at lower loading ratios, with a coexistence of the intercalated cocrystal and neat dimer morphology present at 6.25% MW. The smaller expansion of the unit cell compared to the $Mo(tfd)_3$ could be related to the smaller dopant molecular size, due to fewer substituent groups. It is interesting to note that the highest conductivity values for each of these metal complex dopants is at 25% MW, and the GIXD reveals a coexistence of intercalated morphology and a small fraction of crystalline BTTT-C12 domains. Upon further dopant loading, all crystalline domains of BTTT-C12 are disrupted, with the only crystalline domains that remain corresponding to the intercalated cocrystal, resulting in a slight decrease in conductivity.

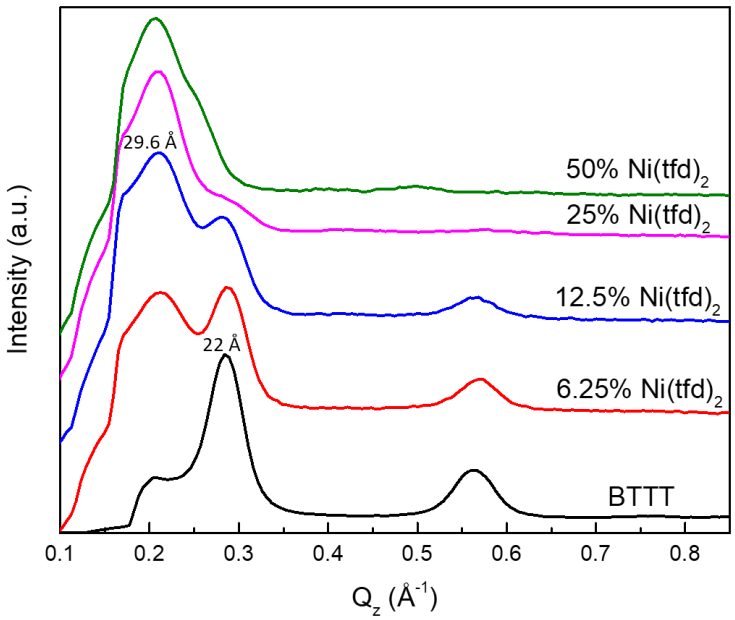

Figure 66 GIXD measurements and out-of-plane linecuts of pure BTTT-C12 and increasingly doped BTTT-C12/Ni(tfd)$_2$ blends.

6.4 Conclusion

This study investigated the effect of dopant choice on the conductivity and morphology using a benchmark oligomer of PBTTT. UV-Vis-NIR spectroscopy measurements reveal that these films form ground-state charge transfer complexes, yet a large six orders of magnitude increase in conductivity is demonstrated using 3D metal complex dopants. Comparing the morphology of the TCNQ and metal complex derivatives reveal a difference in molecular location of the dopants, with the conjugated 2D TCNQ derivatives arranging within the conjugated backbone of the BTTT-C12 due to pi-pi interactions. The 3D metal complexes do not have this strong interaction with the dimer backbone, and instead reside within the side chains of the material, forming an intercalated cocrystal. Although the intercalation of small molecules within PBTTT and derivates has been heavily studied due to the interactions with fullerenes, these metal complex dopants are the first non-fullerene molecule to exhibit similar large out-of-plane expanded intercalated

morphology. It has been previously noted to reduce the coupling between organic semiconductors and dopant frontier molecular orbitals that the use of a three-dimensional organic semiconductor could reduce the pi-pi interactions between the host and dopant. These investigation shows that this type of control is not just limited to the host organic semiconductor and by changing the structure of the dopant from two-dimensional to three-dimensional we can tune the morphology of the blended film and in effect, lead to large variations in conductivity. This study highlights the effect of blended morphology on conductivity and the importance of dopant choice on tuning this morphology and demonstrating the intercalated cocrystal as an advantageous morphology for high conductivities.

6.5 Acknowledgments

We thank Prof. Seth Marder for suppling the dopant materials. Hongmo Li for running UV-Vis-NIR measurements. Liyang Yu for GIXD measurements.

CHAPTER 7

CONCLUSION

7.1 Conclusion

This thesis demonstrates the importance and large effect that processing techniques and chemical modifications have on molecular packing and charge transport within organic semiconducting materials. Through control of processing techniques, a thin film polymorph of bistetracene was discovered and characterized, yet the bulk crystal packing can be accessed in the thin film upon solvent vapor annealing. This process improves hole mobility by three orders of magnitude and allowed for a very controlled system for investigating the effect of molecular packing and directionality on charge transport without any chemical modifications. Temperature dependent mobility measurements also demonstrate a transition from a hopping charge transport mechanism for the thin film polymorph to a lattice scattering behavior in the solvent annealed film. Our experiments highlight the importance of polymorph control and thermal characterization in not just optimizing device performance, but also a powerful tool in understanding the relationship between molecular packing and charge transport mechanism.

The other focus of this thesis is demonstrating how oligomer systems can be powerful tools to investigate the effect of slight chemical modifications to benchmark organic semiconducting materials and understand questions that were previously unanswerable with a polymer system. Using PBTTT as a model system, we were able to characterize the effect of interlayer interactions and terminal methyl vector on the crystal packing of BTTT monomers and characterized a molecular packing alternation that is usually ignored in organic semiconductors.

The BTTT oligomer enabled further understanding the effect of “pocket-height” on intercalated systems using BTTT dimers and fullerenes to synthesize and investigate side chain lengths below the solubility limit of the polymer, PBTTT. Previously, it had been assumed that side

chain length did not influence bimolecular crystal formation, yet this study demonstrates that short side chains form an amorphous blend with fullerenes, previously unaccusable with PBTTT systems.

Expanding on the knowledge of the previous study, we explored the self-assembly properties of atomically similar dimers with varied side chain positions of long and short side chains. We found that the side chain position had a large effect on the materials self-assembly and interactions with fullerenes. Without modification to pocket size or additional additives, we characterized unusual BTTT morphologies, the first phase separated BTTT dimer/fullerene blend, a decrease in lamellar spacing upon fullerene blending, and a coordination of small and long side chains to form intercalated systems. These materials also demonstrate long-term room temperature self-assembly with bimolecular cocrystal formation taking over seven days to assemble. This study highlights the importance of side chain position on small molecule assembly and morphologic control over fullerene interactions through side chain positional modifications.

The last study explored the effect of dopant structure on conductivity using the BTTT dimer system that has previously been representative of the polymer. This study exhibited first demonstration of the expanded BTTT/fullerene cocrystal morphology with a non-fullerene material. This intercalated blend was shown to be advantageous, reaching conductivities three orders of magnitude higher than non-intercalated morphologies. This system could advance future dopant studies as a demonstrated beneficial blend morphology for high conductivity films.

7.2 Outlook

This thesis demonstrates the importance of side chain modification and processing conditions on figures of merit in organic semiconducting materials. The lasting message of this work will be the necessity to recognize the importance of dopant/semiconductor interactions in achieving high conductivity films through molecular doping. For many years the field of organic

semiconducting doping usually operated using the same formula. Take the highest mobility organic semiconductor and blend it with the benchmark p-dopant, F4TCNQ. Report the results and repeat after a new higher mobility material is available. This process has only led to moderate conductivities, no system that rivals that of PEDOT:PSS, and no overarching understanding the doping mechanism in organic semiconductors.

This and other groups recent work has demonstrated the impact of tuning the interactions between the organic semiconductor and dopant together and that selecting the dopant on a system-dependent level can have a much larger effect on conductivity than just using the highest mobility semiconductor with a benchmark dopant. Side chain modification has been demonstrated as a beneficial tool to tune the semiconductor/dopant interactions and morphology to reach higher conductivities. The use of ethylene glycol side chains improved dopant miscibility in organic semiconductors, thus increasing dopant sites and conductivity. Intelligent molecular design to control dopant interactions and location within blends has also show large increases in conductivity compared to standard benchmark organic semiconducting materials. I believe that there will be great advances in molecular doped organic semiconductors, and with a combination of increased knowledge of the interactions of certain side chain modifications with certain dopants will lead to blends in which the morphology of the organic semiconductor is not disrupted upon dopant blending but enhanced. The intercalated cocrystal morphology of organic semiconductor and dopant can be modified to yield a more crystalline mixture upon changes to the side chain chemistry. The understanding of the rules governing intercalation of molecular dopants and formation of highly crystalline blend morphologies will be a powerful tool in the understanding of the organic semiconducting dopant and could allow for a detailed understanding of the mechanism of doping.

Oligomeric systems can also be used to shed more light into the misunderstood doping mechanism. A well-controlled system in which the monomer undergoes a ground-state charge transfer complex formation and its polymer forms an ion pair formation would be a great system to further understand the crossover point from one mechanism to the other. A monomer, dimer, trimer, tetramer, pentamer, and polymer study would be of great interest to the doping community. Further investigation at the crossover point using differing processing conditions to investigate if the doping mechanism can be tuned through processing or morphological modification, something not seen to date, would greatly improve our understand of the governing rules of molecular doping.

APPENDIX A

EFFECT OF SIDE CHAIN LENGTH ON BIMOLECULAR CRYSTAL SUPPORTING INFORMATION

Synthesis:

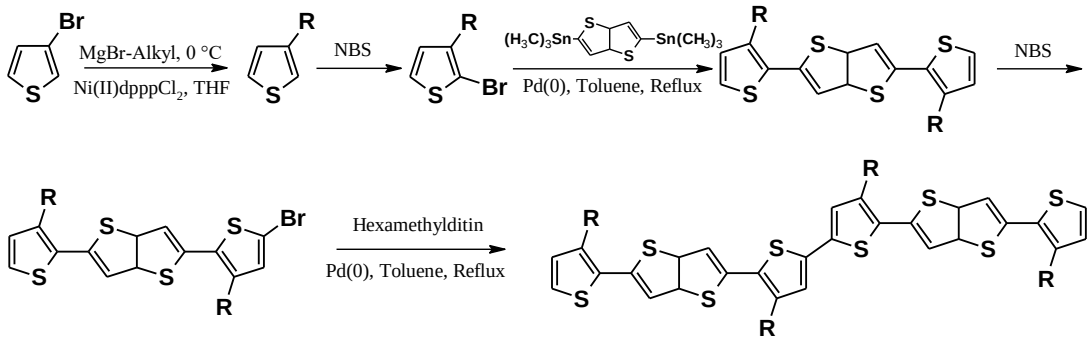

Scheme 1. Shows the general route for dimer (BTTT-R) synthesis with selected linear alkyl chains. R = 4, 5, 6, 7, 8, 9, 10, 11, 12, 14.

General procedure for synthesis of 3-*alkyl*thiophene

n-bromo(butane, pentane, heptane, octane, nonane, decane, undecane, dodecane, tetradecane) were purchased from Sigma Aldrich. Ni(II)Cl_2(dppp), Magnesium, and 3-bromothiophene were purchased from Alfa Aesar. THF was dried in a still with sodium / benzophenone. Glassware was thoroughly dried prior to use.

Preparation of alkyl functionalized thiophene from 3-bromothiophene follows a Kumada coupling procedure adapted from reference [212]. n-bromoalkanes (1 eqv., ~10g) were added to a stirring flask of magnesium (1.05 eqv.) and anhydrous THF (~10ml/$g_{thiophene}$) under nitrogen. Grignard formation took place over 2-4 hours of warm sonication. In some cases, crystalline iodine (~1-3 mg) was added to help speed up the reaction. Formation of Grignard was determined by the disappearance of magnesium and a grey solution color. Note, proper dilution is especially important for longer alkyl chains so they do not 'solidify' and clog the cannula or addition funnel in the subsequent steps. After complete formation of the Grignard, the reaction is cannula

transferred into a dry addition funnel and added dropwise to a stirring mixture of 3-bromothiophene (0.85 eqv.), Ni(II)Cl_2(dppp) (0.02 eqv.), and anhydrous THF at 0 °C under nitrogen. The reaction turns dark brown after addition and is allowed to warm to RT and stir over night. All materials were purified via column chromatography (silica) with hexanes eluent yielding a colorless/light-yellow oil at 70-80% yield.

General procedure for synthesis of 2-bromo-3-*alkyl*thiophene

NBS was purchased from Alfa Aesar and recrystallized from water. Chloroform and glacial acetic acid were purchased from Fischer Scientific.

Bromination of 3-*alkyl*thiophenes proceeds via electrophilic aromatic substitution directed by the alkyl group. 3-alkylthiophene (1 eqv.) is added to stirring mixture of chloroform:glacial acetic acid (50:50 vol) at 0 °C. NBS is then added (1 eqv.) and the reaction is covered to prevent light from forming radical bromine species and is left in ice and covered to stir overnight. The reaction mixture is then extracted with hexanes/water and the organic layer is collected to dry in vacuo. Care must be taken to remove all the acetic acid, and may require additional extraction. The concentrated organic layer is then purified via column chromatography (silica, hexanes) to yield a colorless/light-yellow oil at 90-95% yield.

General procedure for synthesis of BTTT monomer (Monomer-R)

2-Bromo-3-hexylthiophene and 2-bromo-3-dodecylthiophene were purchased from Alfa Aesar. Anhydrous toluene was purchased from Sigma Aldrich. Tetrakis(triphenylphospheno)palladium(0) was purchase from Strem Chemicals. 2,5-bis(trimethyltin)-thieno[3,2-b]thiophene was synthesized according to reference [172]. Glassware was thoroughly dried prior to use.

Monomer-R synthesis follows a procedure previously reported by our group in reference [126,170]. 2-bromo-3-*alkyl*thiophene (2.1 eqv), 2,5-bis(trimethyltin)-thieno[3,2-b]thiophene, Tetrakis(triphenylphospheno)palladium(0), and anhydrous toluene are combined in a dry round bottom flask under nitrogen. The reaction is degassed and heated to reflux overnight. After cooling, toluene is mostly removed in vacuo and hexanes is added forming a red precipitate. This mixture is heated, sonicated, and then gravity filtered and washed with hexanes. The red solid (used catalyst) is discarded. Skipping catalyst removal typically results in clogged column and material trapped in the solidified catalyst. The remaining solution is purified in column chromatography (silica, hexanes) and dried to yield a yellow solid (bright blue fluorescence on TLC); 70% yield.

General procedure for synthesis of monobromo-BTTT monomer (Monomer-R-Br)

Bromination of **Monomer-R** monomer proceeds via electrophilic aromatic substitution of the thiophene α-hydrogen. Note, since both terminal-thiophene α-hydrogens have the same reactivity this reaction will result in significant yields of starting material, mono-brominated (desired product), and di-brominated products. **Monomer-R** (1 eqv.) is added to a stirring mixture of chloroform:glacial acetic acid (50:50 vol) at room temperature. NBS is then added (1.2 eqv.) and the reaction is covered to prevent light from forming radical bromine species. The reaction is left covered to stir overnight. The reaction mixture is then extracted with hexanes/water and the organic layer is collected to dry in vacuo. Care must be taken to remove all the acetic acid, and may require additional extraction. The concentrated organic layer is then purified via column chromatography (silica, hexanes) to yield a bright-yellow solid at 60-75% yield. Note, this can be challenging to separate as the mono-brominated material elutes in between the starting material and di-brominated biproduct.

General procedure for synthesis of the BTTT dimer (BTTT-R)

Hexamethylditin was purchased from Alfa Aesar. Glassware was thoroughly dried prior to use. Note, Hexamethylditin is acutely toxic and should be handled with great care.

Dimers (**BTTT-R**) are synthesized through Stille coupling of **Monomer-R-Br**. Hexamethylditin (0.5 eqv.), tetrakis(triphenylphosphine) palladium (0) (0.1 eqv.), anhydrous toluene, and **Monomer-R-Br** are added to a dry round bottom flask with a reflux condenser. The reaction is degassed and heated to reflux overnight. After cooling, toluene is mostly removed in vacuo and hexanes is added forming a red precipitate. This mixture is heated, sonicated, and then gravity filtered and washed with hexanes. The red solid (used catalyst) is discarded. Skipping catalyst removal typically results in clogged column and material trapped in the solidified catalyst. The remaining solution is purified in column chromatography (silica, hexanes) and dried to yield a yellow solid (bright blue fluorescence on TLC); 60% yield. Note, low side chain lengths (C4 for example) are not very soluble in hexanes and may require alternate catalyst removal techniques. Additionally, C4 and C5 materials are purified in chromatography with hot hexanes.

Characterization: NMR, Bruker 500 MHz.

BTTT-4 ^{1}H NMR (500 MHz, $CDCl_3$, δ) 7.25 (s, 4H), 7.22 (d, 2H), 7.04 (s, 2H), 6.96 (d, 2H), 2.82 (t, 8H), 1.68 (m, 8H), 1.42 (m, 8H), 0.95 (t, 12H)

BTTT-5 ^{1}H NMR (500 MHz, $CDCl_3$, δ) 7.27 (s, 4H), 7.25 (d, 2H), 7.06 (s, 2H), 7.00 (d, 2H), 2.80 (m, 8H), 1.71 (m, 8H), 1.39 (m, 16H), 0.95 (t, 12H)

BTTT-6 1H NMR (500 MHz, $CDCl_3$, δ) 7.27 (s, 4H), 7.25 (d, 2H), 7.06 (s, 2H), 7.00 (d, 2H), 2.84 (m, 8H), 1.71 (m, 8H), 1.42-1.30 (m, 24H), 0.95 (t, 12H)

BTTT-7 ^{1}H NMR (500 MHz, $CDCl_3$, δ) 7.25 (s, 4H), 7.23 (d, 2H), 7.04 (s, 2H), 6.97 (d, 2H), 2.80 (m, 8H), 1.68 (m, 8H), 1.42-1.25 (m, 32H), 0.88 (t, 12H)

BTTT-8 ^{1}H NMR (500 MHz, $CDCl_3$, δ) 7.25 (s, 4H), 7.23 (d, 2H), 7.04 (s, 2H), 6.97 (d, 2H), 2.80 (m, 8H), 1.68 (m, 8H), 1.42-1.25 (m, 40H), 0.88 (t, 12H)

BTTT-9 ^{1}H NMR (500 MHz, $CDCl_3$, δ) 7.25 (s, 4H), 7.23 (d, 2H), 7.04 (s, 2H), 6.97 (d, 2H), 2.80 (m, 8H), 1.68 (m, 8H), 1.42-1.25 (m, 48H), 0.88 (t, 12H)

BTTT-10 ^{1}H NMR (500 MHz, $CDCl_3$, δ) 7.25 (s, 4H), 7.23 (d, 2H), 7.04 (s, 2H), 6.97 (d, 2H), 2.80 (m, 8H), 1.68 (m, 8H), 1.42-1.25 (m, 56H), 0.88 (t, 12H)

BTTT-11 ^{1}H NMR (500 MHz, $CDCl_3$, δ) 7.25 (s, 4H), 7.23 (d, 2H), 7.04 (s, 2H), 6.97 (d, 2H), 2.80 (m, 8H), 1.68 (m, 8H), 1.42-1.25 (m, 64H), 0.88 (t, 12H)

BTTT-12 ^{1}H NMR (500 MHz, $CDCl_3$, δ) 7.25 (s, 4H), 7.23 (d, 2H), 7.04 (s, 2H), 6.97 (d, 2H), 2.80 (m, 8H), 1.68 (m, 8H), 1.42-1.25 (m, 72H), 0.88 (t, 12H)

BTTT-14 ^{1}H NMR (500 MHz, $CDCl_3$, δ) 7.27 (s, 4H), 7.25 (d, 2H), 7.06 (s, 2H), 7.00 (d, 2H), 2.84 (m, 8H), 1.71 (m, 8H), 1.42-1.28 (m, 88H), 0.88 (t, 12H)

BTTT-14 ^{13}C NMR (500MHz, $CDCl_3$, δ) 140.97, 140.32, 139.27, 139.12, 137.89, 137.24, 135.33, 130.71, 130.10, 129.92, 126.67, 124.41, 118.01, 117.82, 31.94, 30.81, 30.63, 29.72, 29.68, 29.61, 29.56, 29.49, 29.38, 29.25, 22.71, 14.14

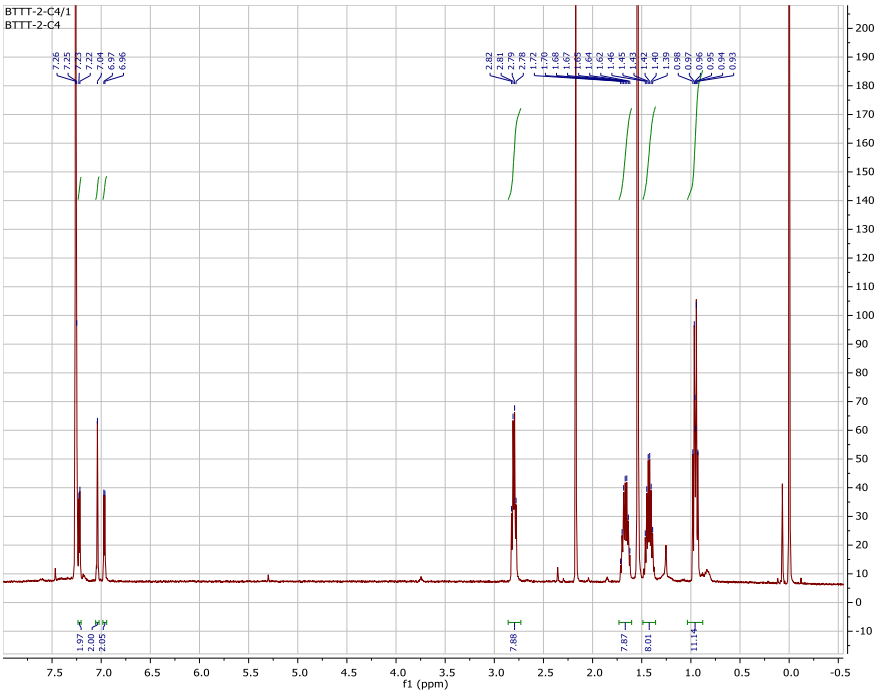

Figure 67. **BTTT-4** ^{1}H NMR (500 MHz, $CDCl_3$)

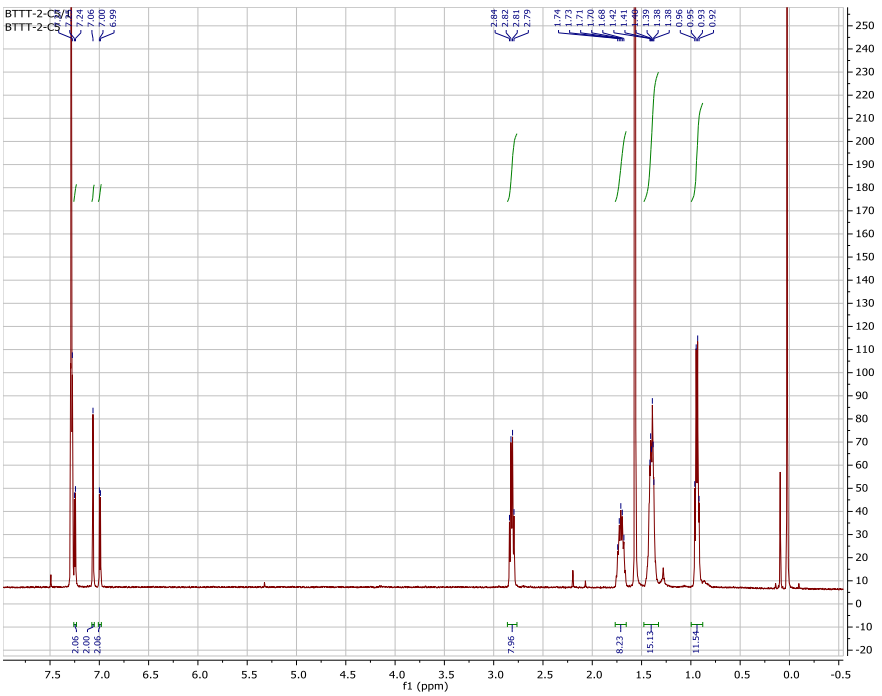

Figure 68. BTTT-5 ^{1}H NMR (500 MHz, $CDCl_3$)

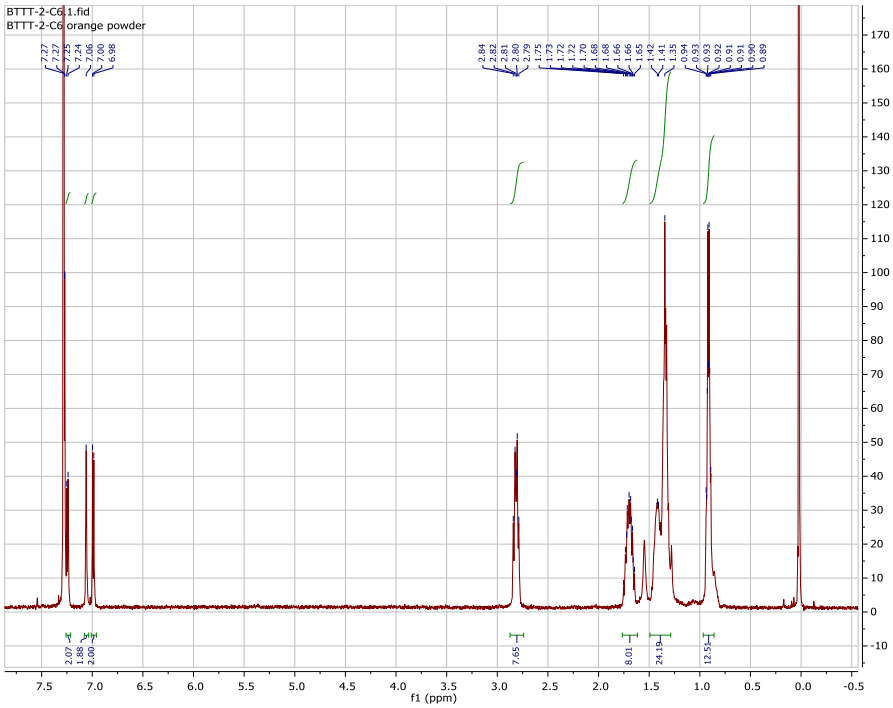

Figure 69. **BTTT-6** ^{1}H NMR (500 MHz, $CDCl_3$)

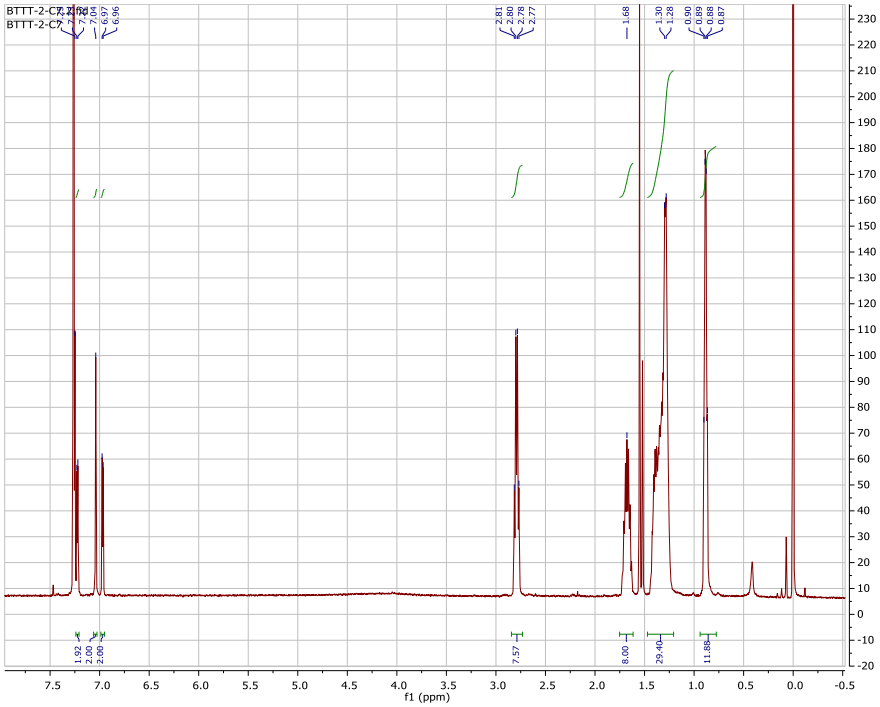

Figure 70. **BTTT-7** ^{1}H NMR (500 MHz, $CDCl_3$)

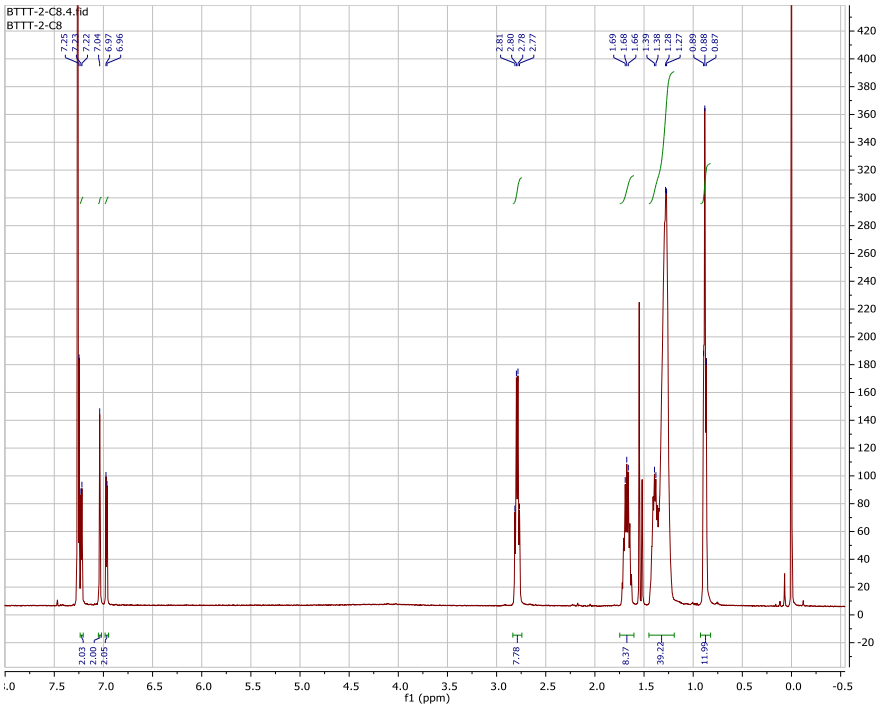

Figure 71. BTTT-8 ^{1}H NMR (500 MHz, $CDCl_3$)

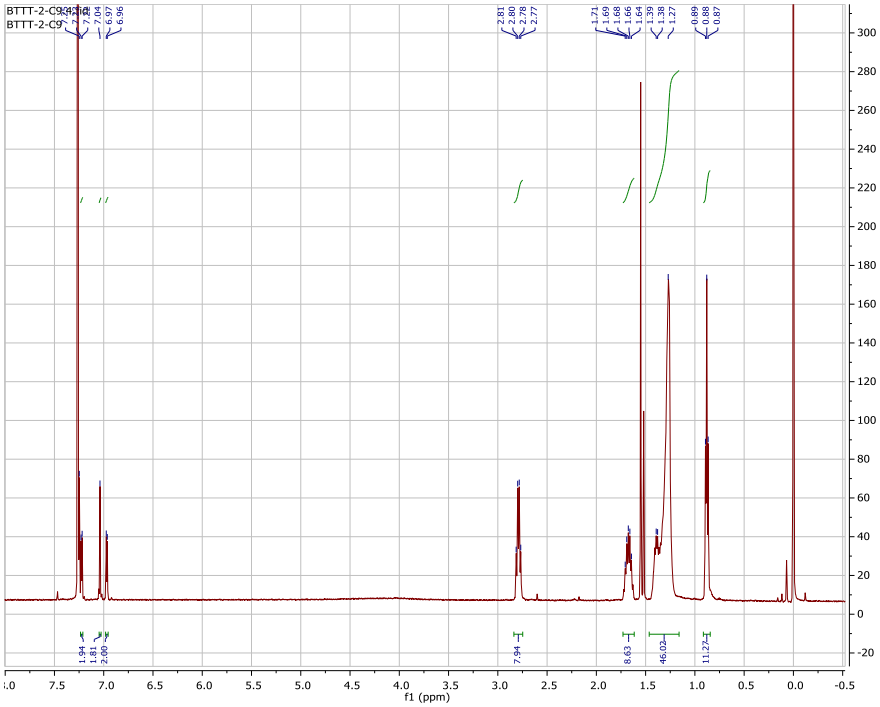

Figure 72. **BTTT-9** ^{1}H NMR (500 MHz, $CDCl_3$)

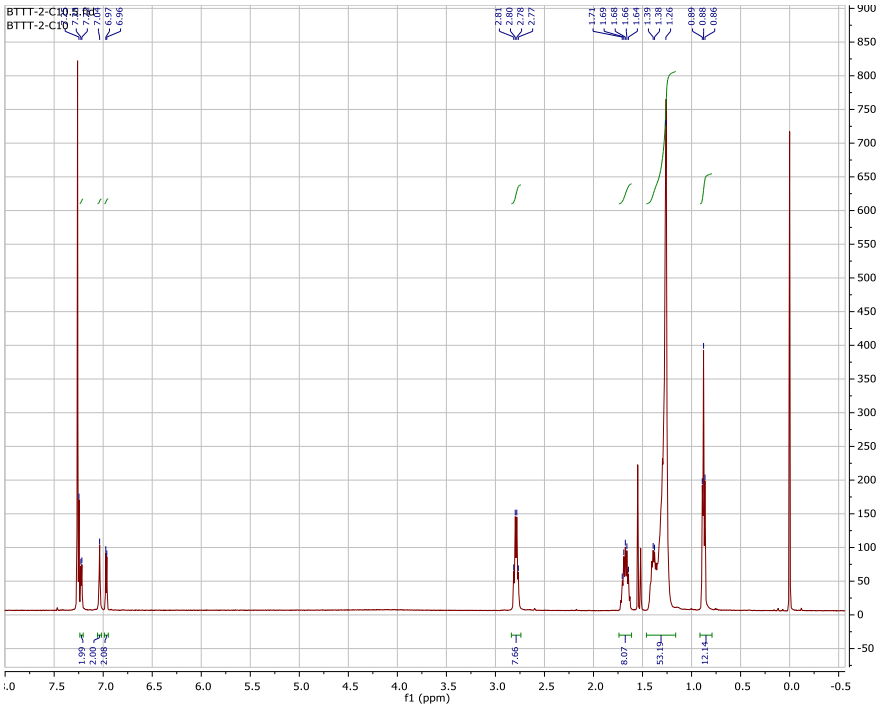

Figure 73. **BTTT-10** ^{1}H NMR (500 MHz, $CDCl_3$)

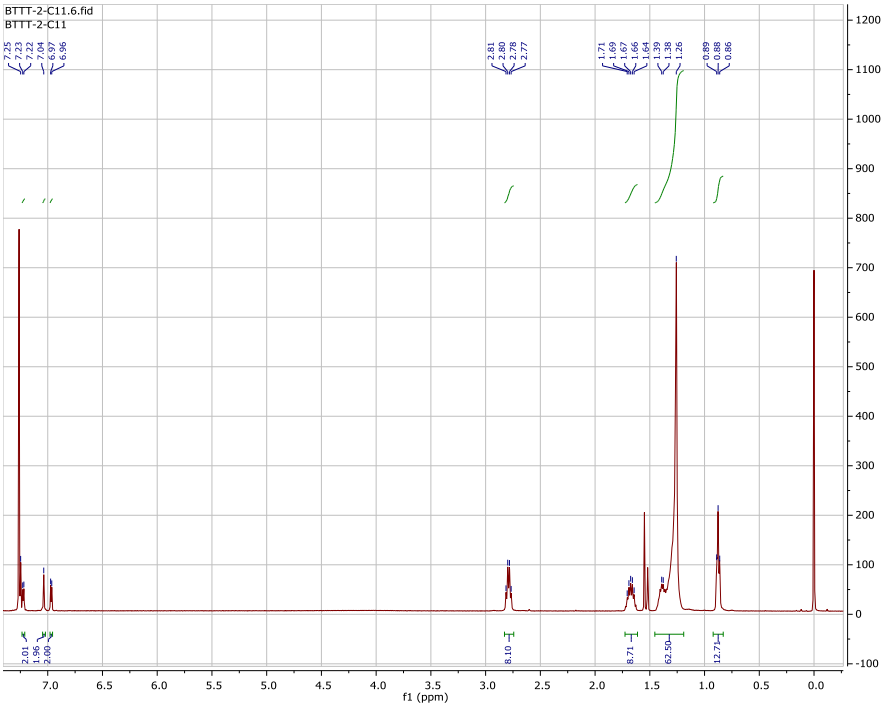

Figure 74. BTTT-11 ^{1}H NMR (500 MHz, $CDCl_3$)

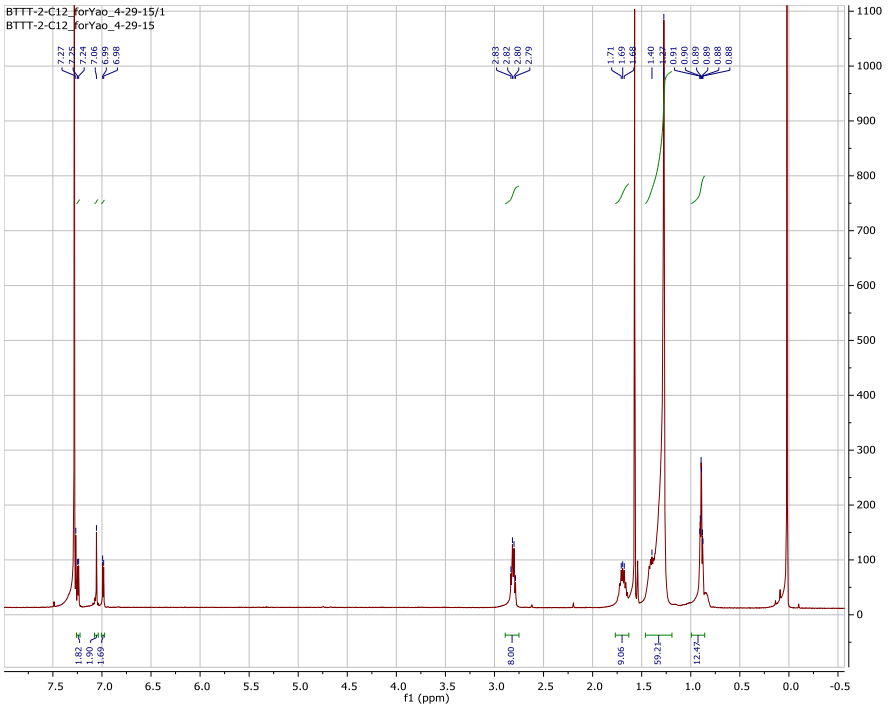

Figure 75. BTTT-12 ^{1}H NMR (500 MHz, $CDCl_3$)

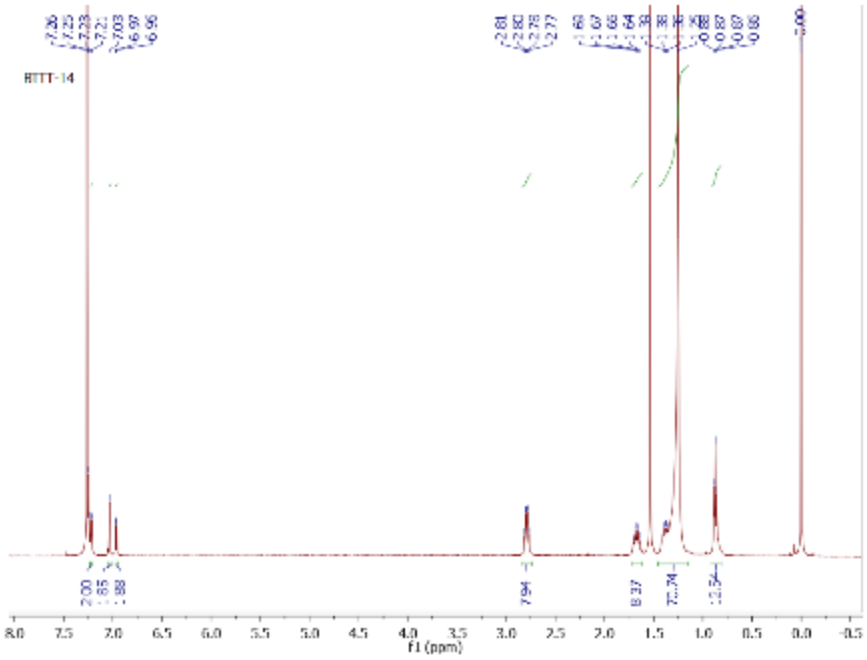

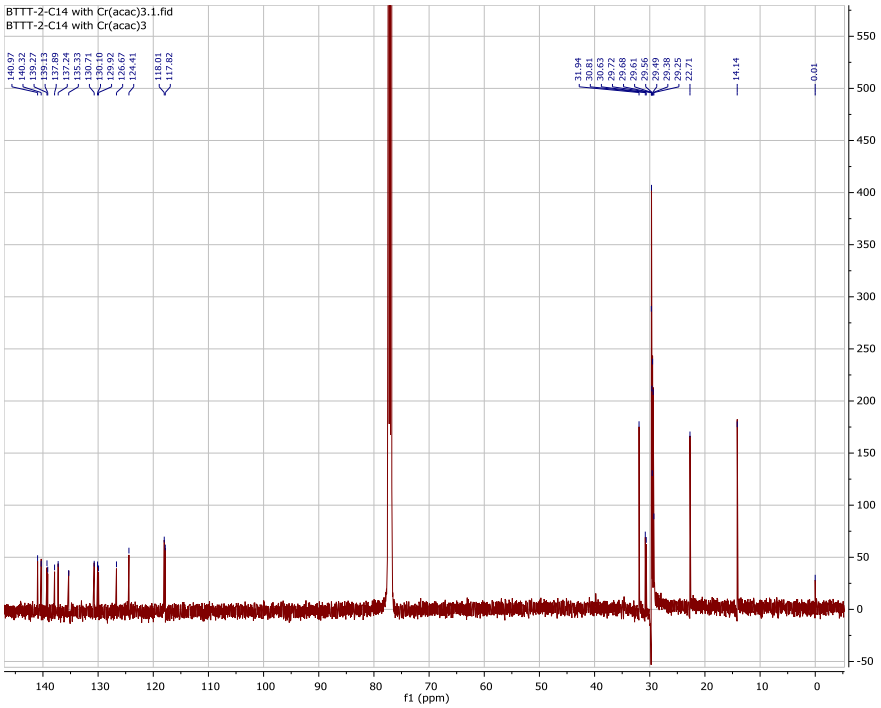

Figure 76. **BTTT-14** ^{13}C NMR (500 MHz, $CDCl_3$)

Crystallography:

Single crystals of all materials were grown in solution by slow evaporation of hexanes. X-ray diffraction data were collected on either a Bruker-Nonius X8 Proteum or D8 Venture diffractometers with graded-multilayer focused CuK(alpha) x-rays. Raw data were integrated, scaled, merged and corrected for Lorentz-polarization effects using either the APEX2/3 packages.[213] Corrections for absorption were applied using SADABS.[214] The structure was solved by direct methods (SHELXT)[215] and refined against F^2 by weighted full-matrix least-squares (SHELXL)[216]. Hydrogen atoms were found in difference maps but subsequently placed at calculated positions and refined using a riding model. Non-hydrogen atoms were refined with anisotropic displacement parameters. The final structure models were checked using an R-tensor[217] and by Platon/checkCIF[218]. Atomic scattering factors were taken from the International Tables for Crystallography.[219]

Dimers BTTT-7 to BTTT-14 all pack in ostensibly the same manner.

BTTT-2--6 , -5, and -4 have different packing. BTTT-2-C6 single crystal file has been previously reported and does not follow the packing trend in the of oligomers with larger alkyl chains.[170] The terminal thiophenes in BTTT-2-C6 adopt a different rotational conformation which facilitates larger backbones interactions. Crystals capable of diffraction for BTTT-2-C5 and C4 could not be grown.

UV-Vis:

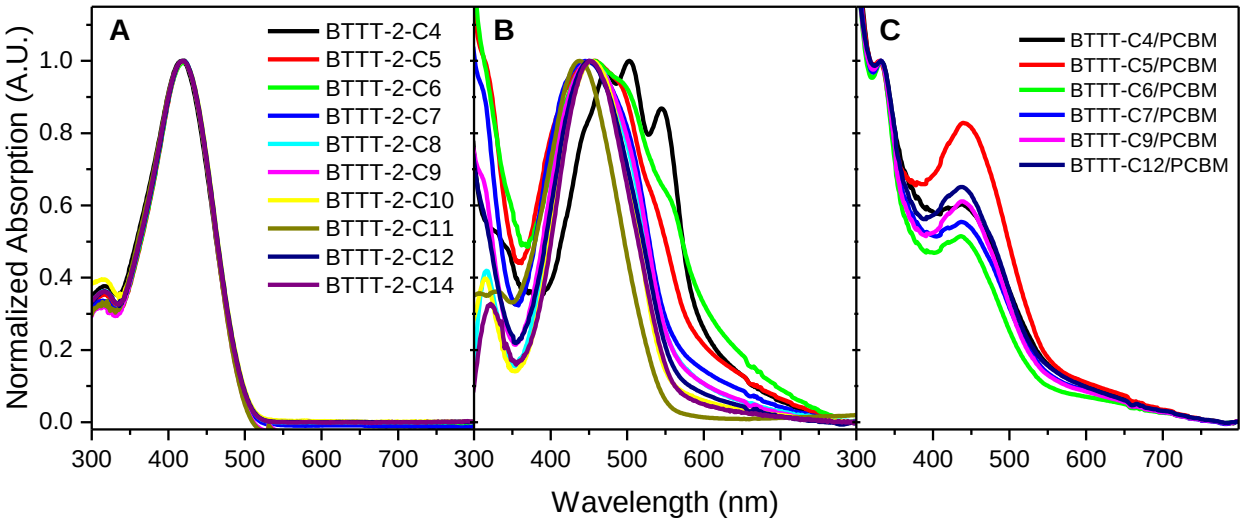

UV-Vis characterization of neat dimers in solution, film, and in blended films with $PC_{61}BM$ are shown in **Error! Reference source not found.** a, b, c respectively. All dimers in solution (chloroform) show identical absorption spectra with a maximum absorption at 418 nm. Since the dimer series has no chemical modification to the backbone, we expect no changes to solution absorption. On the other hand, dimers in casted films exhibit some variation in absorption spectra. BTTT-14 to -7 are broad and redshifted as compared to the solution spectra with an absorption maxima ~450 nm. Films of BTTT-6, -5, and -4 show additional redshifting and the onset of new vibronic peaks. The new spectral shape corroborates well with the GIXD of the neat films which indicates a different thin film packing than is observed in the smaller side chain dimers (C4-C6). In the blended films, no major differences in spectra shape, intensity, or position are noticeable in the full range of blended dimers.

Grazing Incidence X-ray Diffraction:

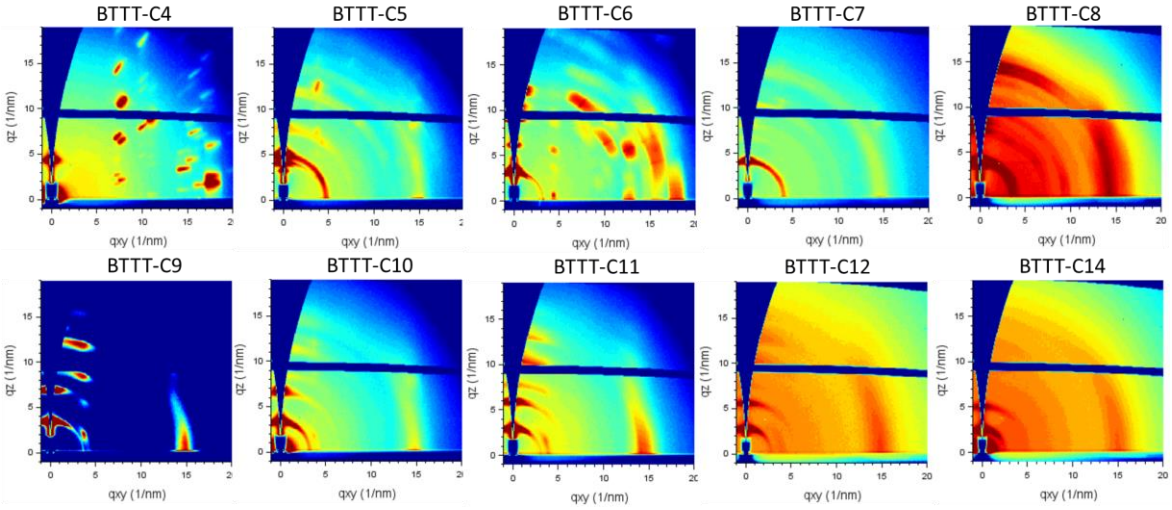

Figure 77. GIXD Diffractograms of **neat dimer** films spin cast from 10mg/ml chloroform solution on Si substrates.

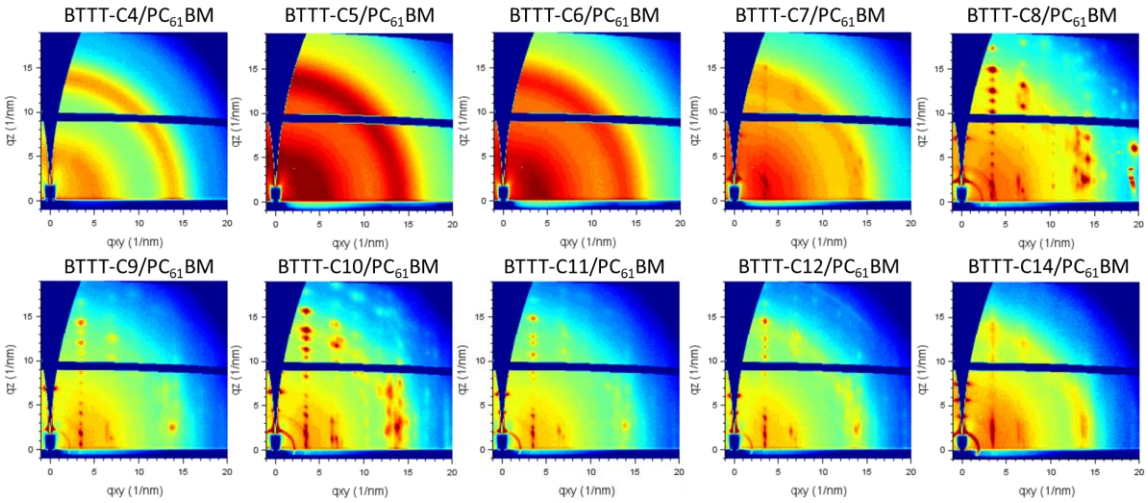

Figure 78. GIXD Diffractograms of 50:50 wt% **dimer:$PC_{61}BM$** films spin cast from 10mg/ml chloroform solution on Si substrates.

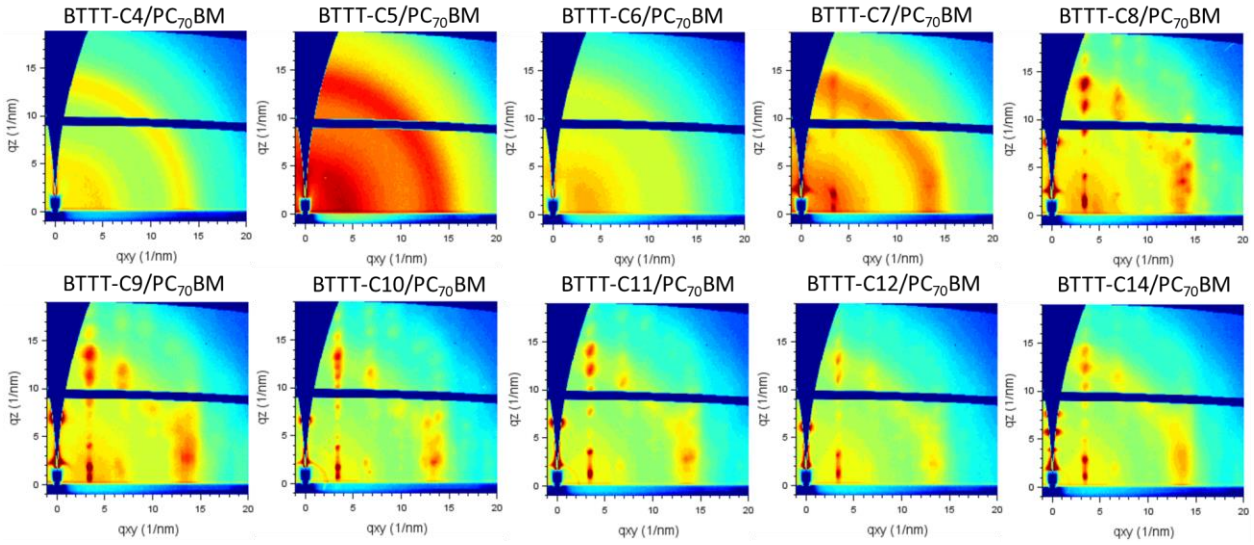

Figure 79. GIXD Diffractograms of 50:50 wt% **dimer:$PC_{71}BM$** films spin cast from 10mg/ml chloroform solution on Si substrates.

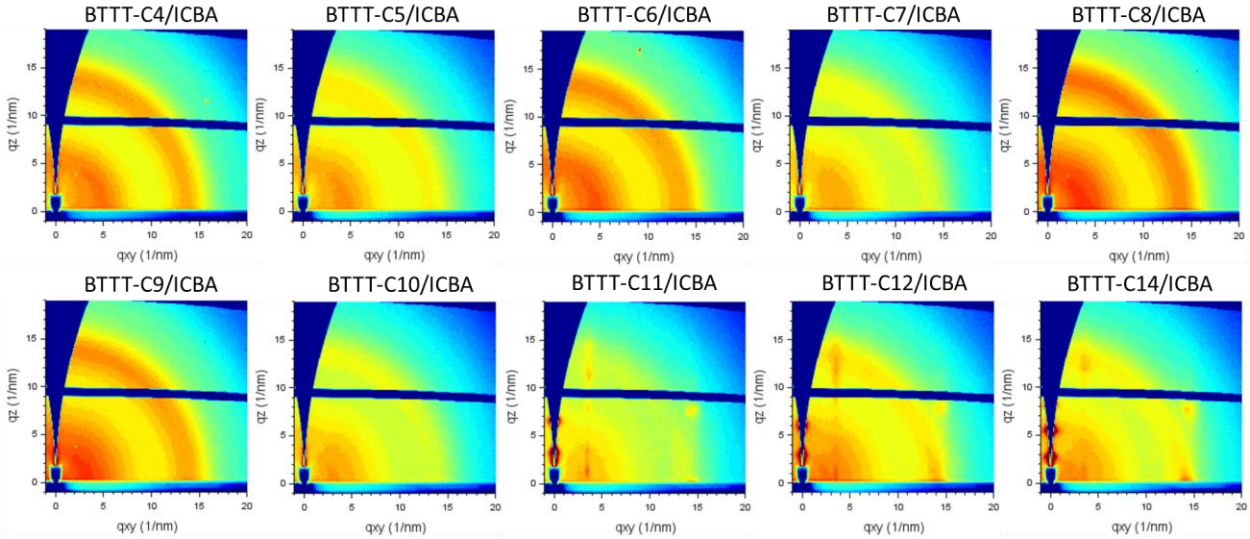

Figure 80. GIXD Diffractograms of 50:50 wt% **dimer:ICBA** films spin cast from 10mg/ml chloroform solution on Si substrates.

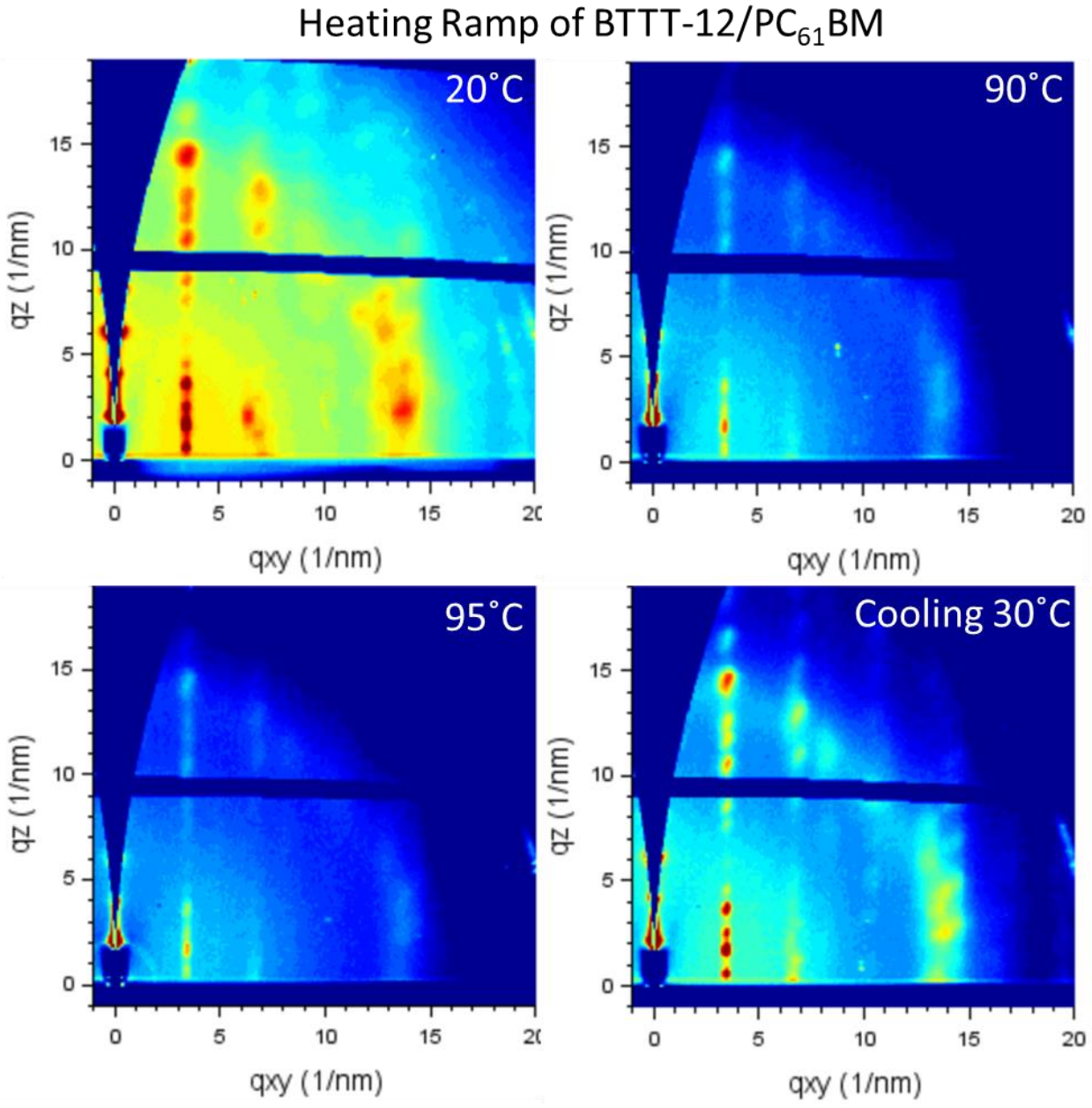

Figure 81. GIXD in-situ heating of BTTT-12/PC61BM.

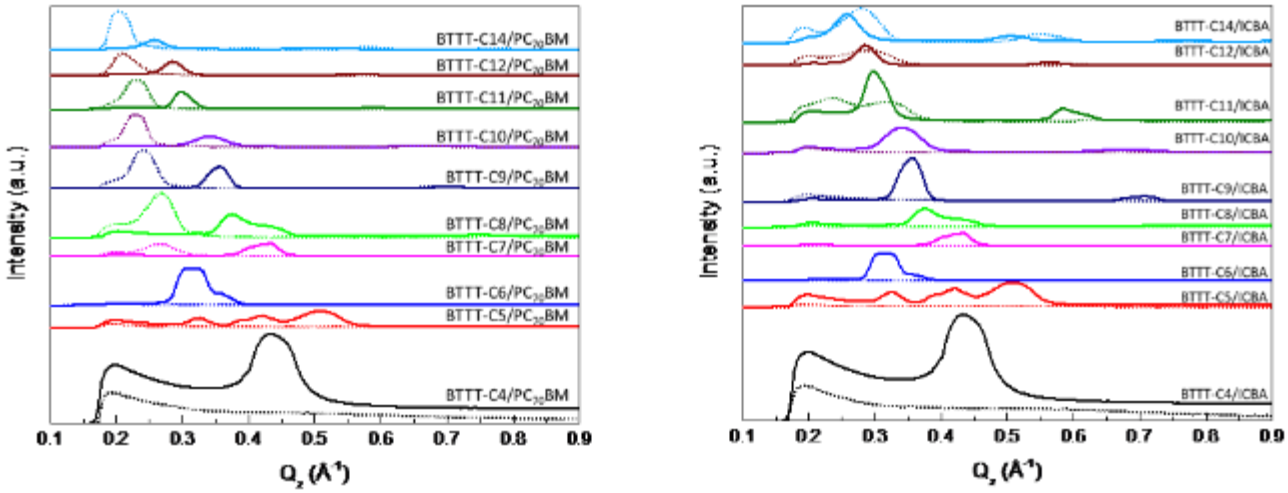

Figure 82. GIXD Q_z linecuts from **$PC_{71}BM$** blends (left) and **ICBA** Blends (right).

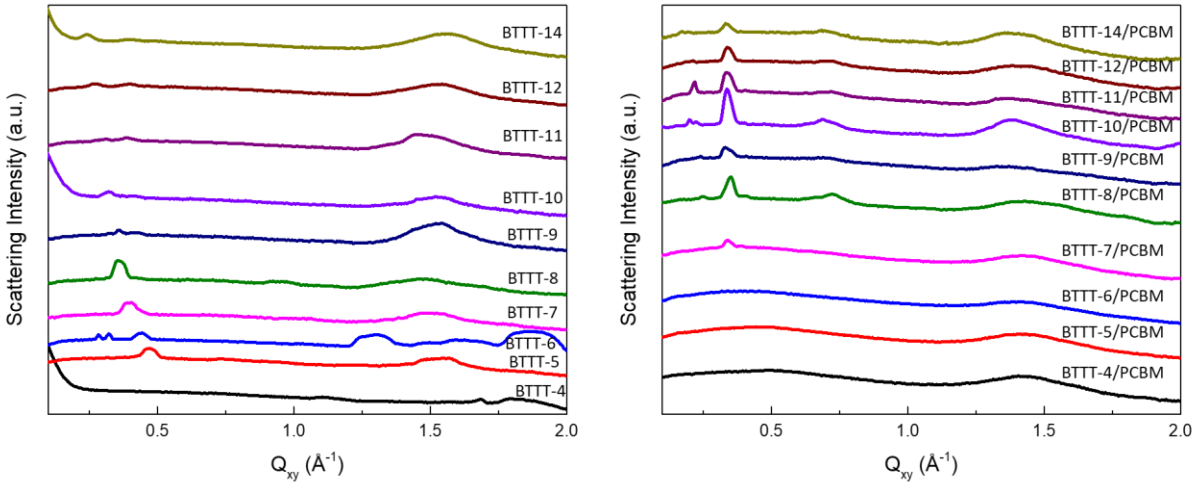

Figure 83. GIXD Q_{xy} linecuts from neat **Dimers** (left) and **PC61BM** Blends (right).

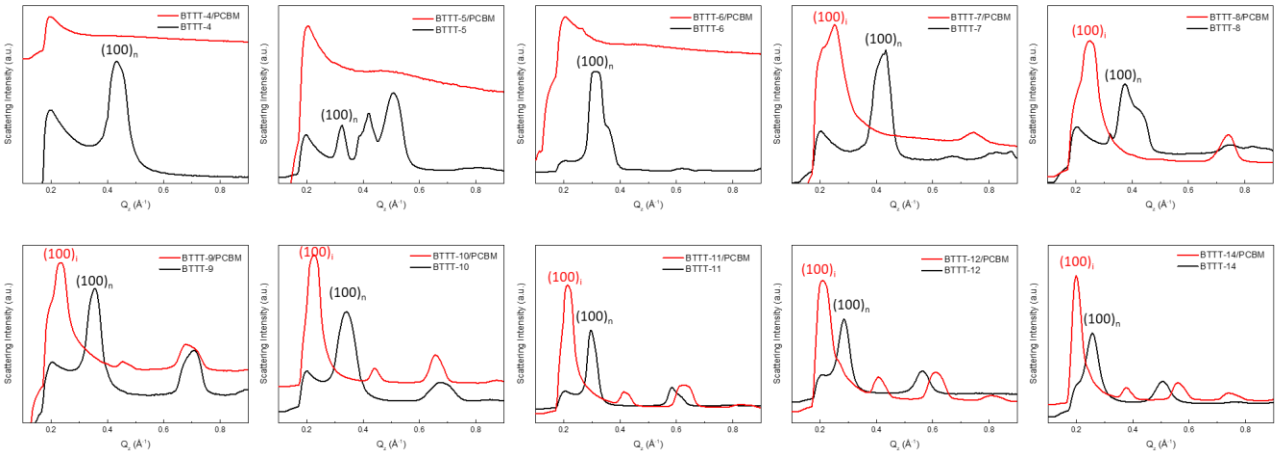

Figure 84. Separated Qz linecuts from neat (black) and PC61BM blended (red) films.

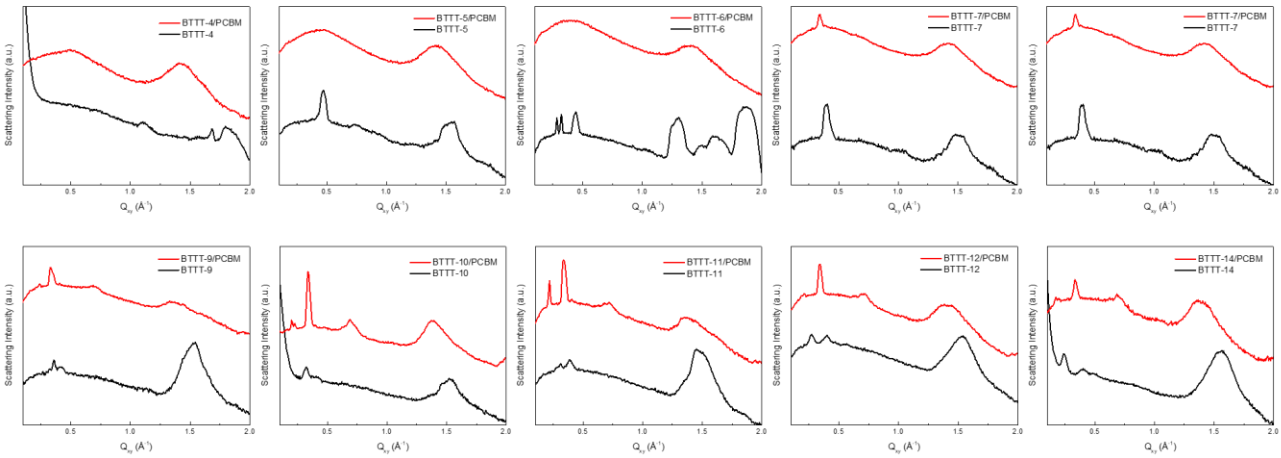

Figure 85. Separated Qxy linecuts from neat (black) and PC61BM blended (red) films.

Differential Scanning Calorimetry:

DSC of Dimer Powders:

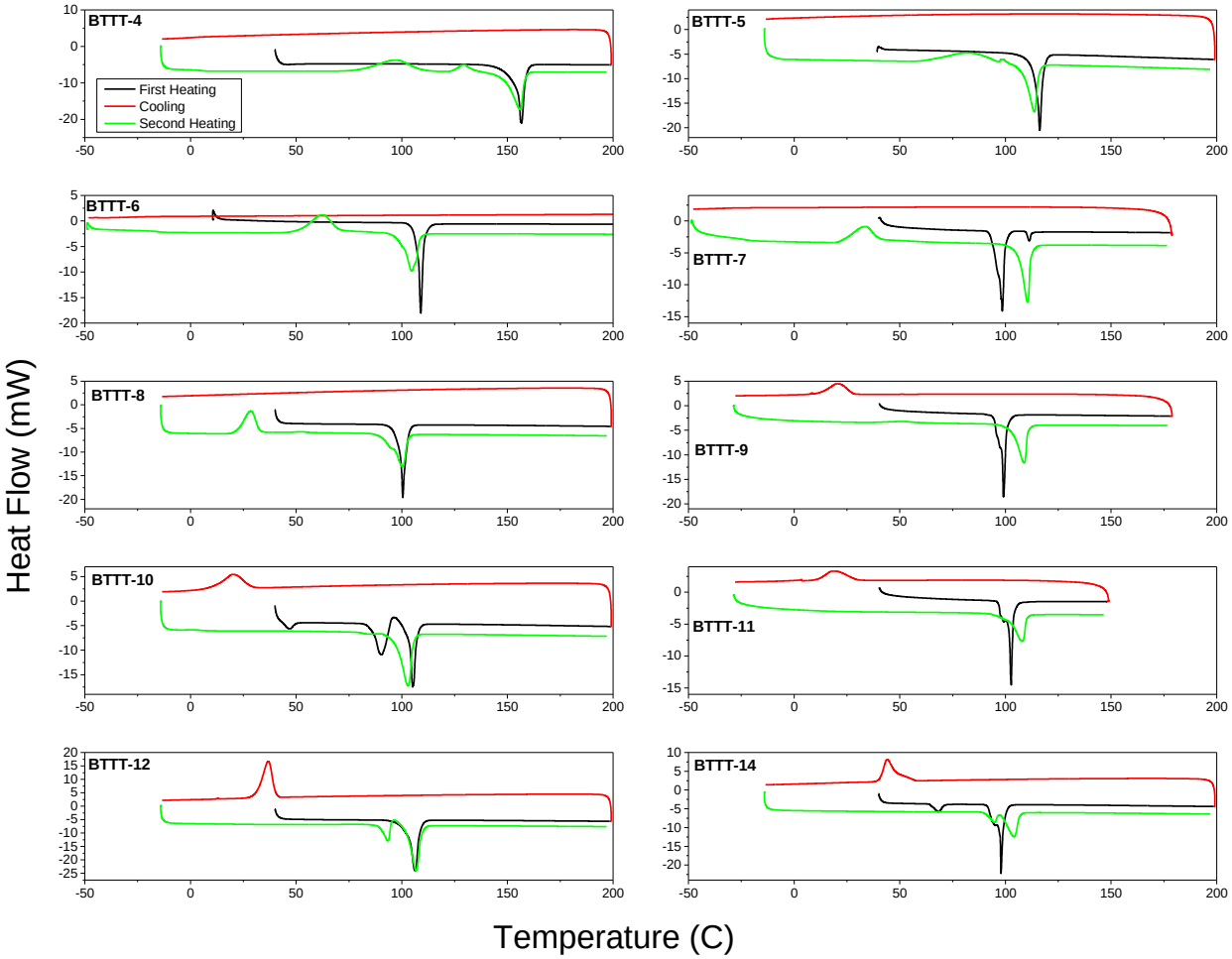

DSC of Drop cast films

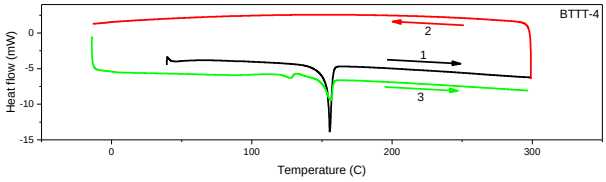

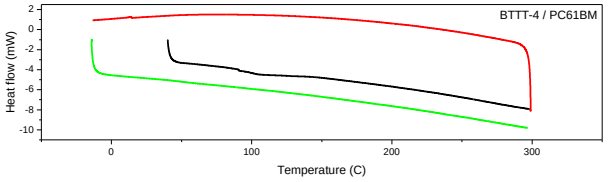

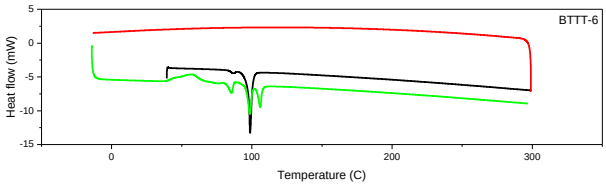

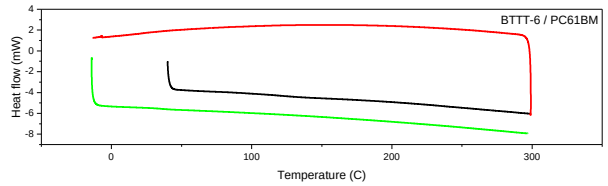

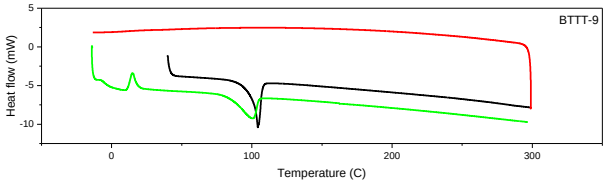

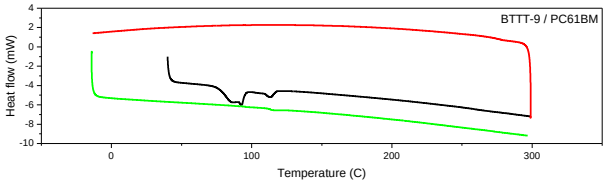

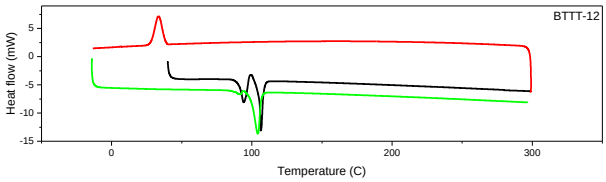

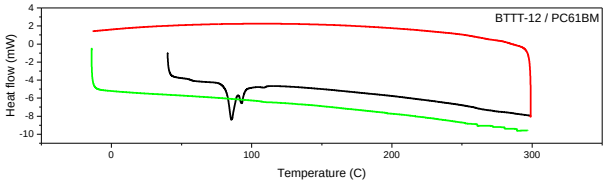

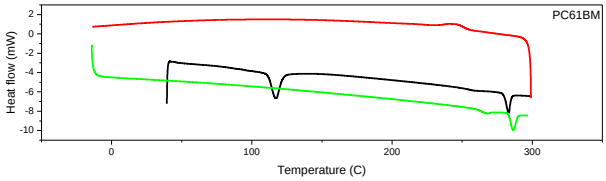

First Heating (10 C/min)
Cooling (10 C/min)
Second Heating (10 C/min)

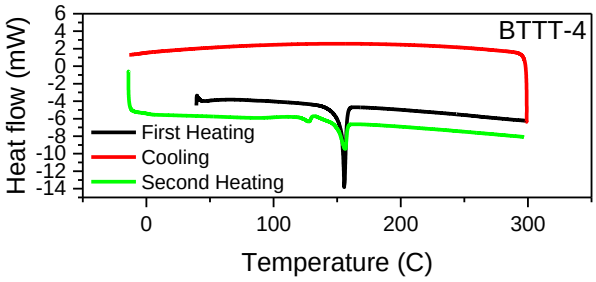
BTTT-4
Heat flow (mW)
6
4
2
0
-2
-4
-6
-8
-10
-12
-14
First Heating
Cooling
Second Heating
0
100
200
300
Temperature (C)

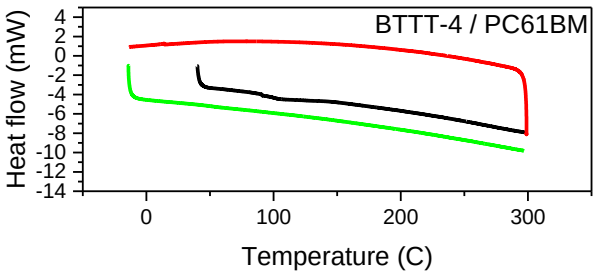
BTTT-4 / PC61BM
Heat flow (mW)
4
2
0
-2
-4
-6
-8
-10
-12
-14
0
100
200
300
Temperature (C)

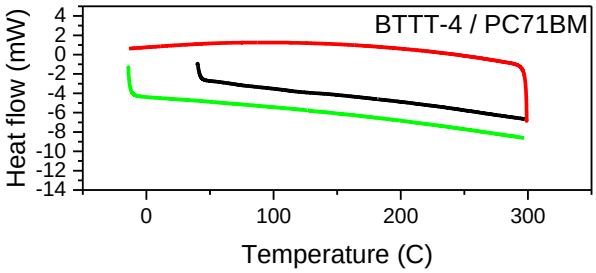
BTTT-4 / PC71BM
Heat flow (mW)
4
2
0
-2
-4
-6
-8
-10
-12
-14
0
100
200
300
Temperature (C)

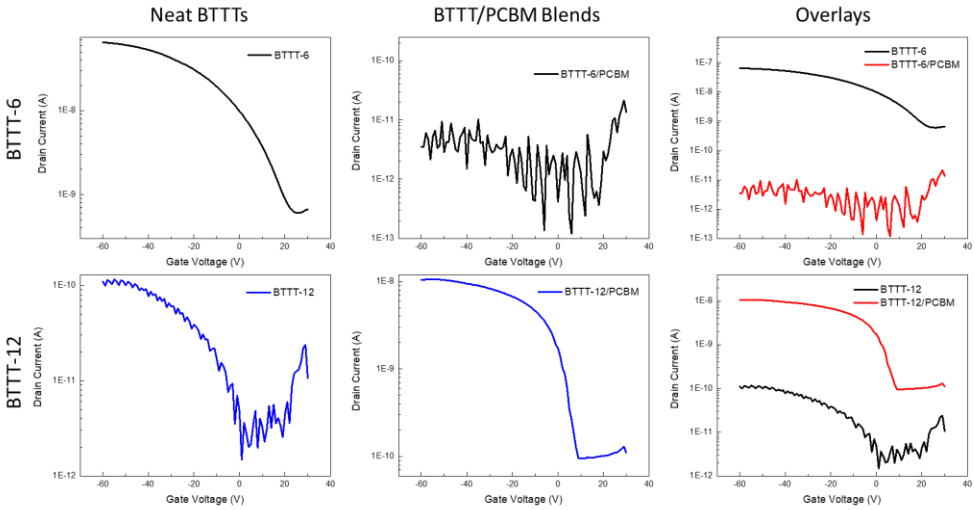

Figure 86. OFET transfer curves.

APPENDIX B

VARIABLE SIDE CHAIN BTTT DIMER SYNTHESIS

B.1. Schematic of Synthesis Pathway for Variably-Substituted Oligothiophenes

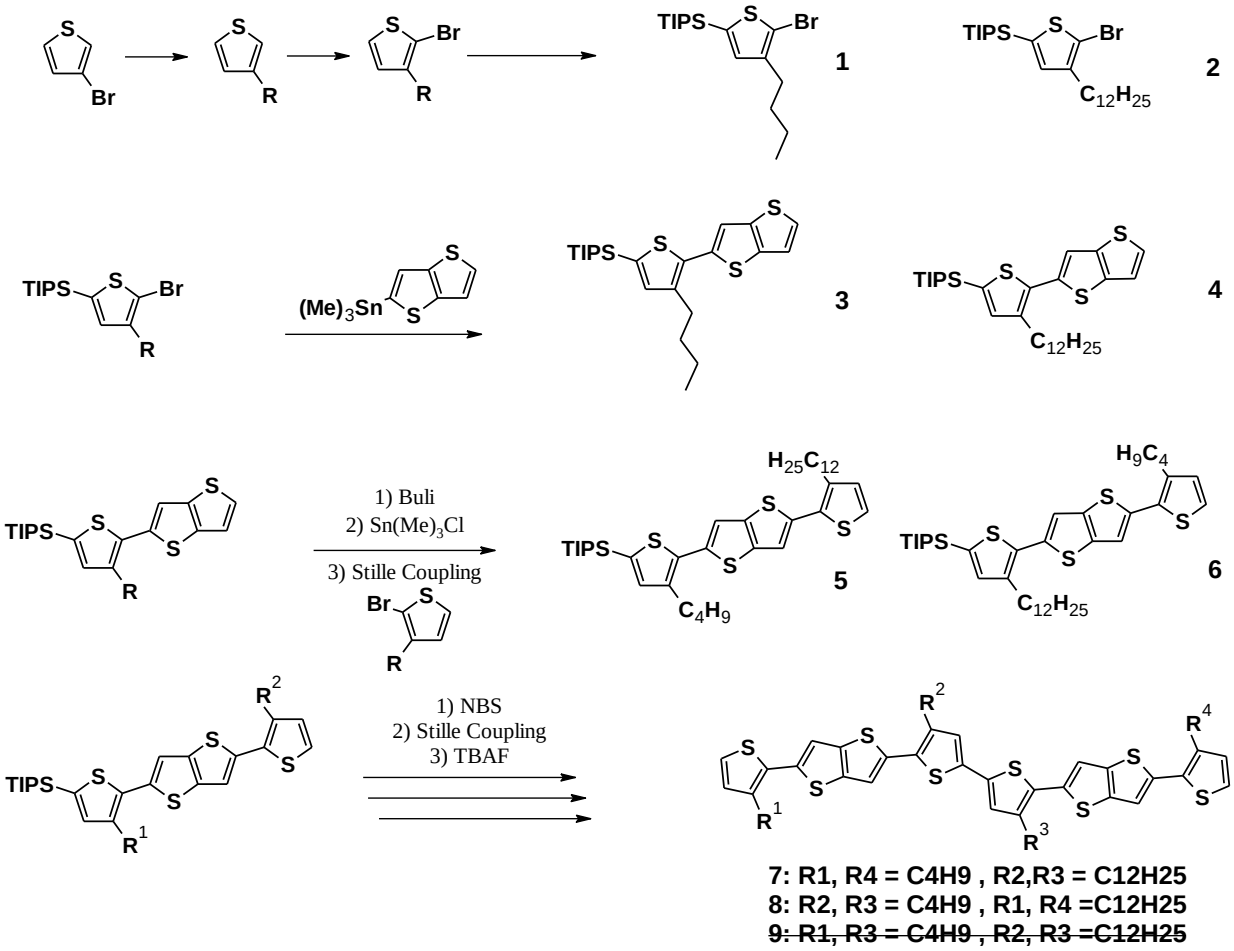

Scheme 2 Synthesis of selected variable-substituted BTTT dimers. Molecule 9 could not be synthesized with the attempted pathway.

General Synthesis of Synthesis of **1**, **2**, **3**, **4**, **5**, and **6** are previously described.
^{1}H NMR, Maldi, reported here:
(3) TIPS-T4-TT: ^{1}H NMR (500 MHz, $CDCL_3$, δ) 7.38 (d, 1H), 7.32 (d, 1H), 7.27 (d, 1H), 7.09 (s, 1H), 2.80 (t, 2H), 1.68 (m, 2H), 1.42 (m, 2H), 1.34 (m, 3H) 1.15 (d,18H), 0.96 (t, 3H)

(4) TIPS-T12-TT: ^{1}H NMR (500 MHz, $CDCL_3$, δ) 7.38 (d, 1H), 7.32 (d, 1H), 7.27 (d, 1H), 7.09 (s, 1H), 2.80 (t, 2H), 1.68 (m, 2H), 1.42-1.25 (m, 21H), 1.15 (d,18H), 0.96 (t, 3H)

(5) TIPS-T4-TT-T12: ^{1}H NMR (500 MHz, $CDCL_3$, δ) 7.29 (s, 1H), 7.26 (s, 1H) 7.24 (d, 1H), 7.09 (s, 1H), 6.99 (d, 1H), 2.82 (dt, 4H), 1.68 (m, 4H), 1.5-1.22 (m, 26H), 1.15 (d, 18H), 0.97 (t, 3H), 0.90 (t, 3H) MALDI: M/Z 684, Calc 684 g/mol

(6) TIPS-T12-TT-T4: ^{1}H NMR (500 MHz, $CDCL_3$, δ) 7.29 (s, 1H), 7.26 (s, 1H) 7.24 (d, 1H), 7.09 (s, 1H), 6.99 (d, 1H), 2.82 (m, 4H), 1.68 (m, 4H), 1.5-1.22 (m, 26H), 1.15 (d, 18H), 0.97 (t, 3H), 0.90 (t, 3H) MALDI: M/Z 684, Calc 684 g/mol

Purification challenges of 5

Note, despite several columns (silica gel, hexanes), purification of **5** could not be accomplished. The starting material (**3**) could not be separated from the desired product. After several columns without good separation, the material was moved to the next reactions where either bromination or deprotection would hopefully provide an acceptable separation of the starting material impurity. As is described below, this did not provide the necessary separation needed to purify **5** or its derivatives. **6** was easily separated and purified away from the starting materials.

General procedure for synthesis of 7 and 8 (BTTT-4-12-12-4 and BTTT-12-4-4-12, respectively).

The monoprotected asymmetric monomer (**5** or **6**) is brominated with NBS via electrophilic aromatic substitution of the thiophene α-hydrogen. **5** or **6** (1 eqv.) is added to a stirring mixture of chloroform:glacial acetic acid (50:50 vol) at room temperature. NBS is then added (1.05 eqv.) and the reaction is covered to prevent light from forming radical bromine species. The reaction is left covered to stir overnight. The reaction mixture is then extracted with hexanes/water and the organic layer is collected to dry in vacuo. Care must be taken to remove all the acetic acid, and may require additional

extraction. The concentrated organic layer is then purified via column chromatography (silica, hexanes) to yield a bright-yellow solid at 90% yield. Note, despite bromination of **5**, the starting material (now brominated as well, **3-Br**) was still inseparable. **5-Br** was purified as much as possible with column chromatography and collected for the to the next reaction. Stille coupling of impure materials is particular detrimental to final product purification; coupling can occur between the various active species generating multiple impurities in significant yield as illustrated in Scheme 3. Thus, starting material purity is of particular importance for Stille coupling reactions.

(5-Br) TIPS-T4-TT-T12-Br: ^{1}H NMR (500 MHz, $CDCL_3$, δ) 7.28 (s, 1H), 7.21 (s, 1H), 7.09 (s, 1H), 6.94 (s, 1H), 2.86 (t, 2H), 2.75 (t, 2H), 1.65 (m, 4H), 1.5-1.22 (m, 26H), 1.15 (d, 18H), 0.97 (t, 3H), 0.90 (t, 3H) MALDI: M/Z 764, Calc 764 g/mol
(6-Br) TIPS-T12-TT-T4-Br: ^{1}H NMR (500 MHz, $CDCL_3$, δ) 7.28 (s, 1H), 7.21 (s, 1H), 7.09 (s, 1H), 6.94 (s, 1H), 2.86 (t, 2H), 2.75 (t, 2H), 1.65 (m, 4H), 1.5-1.22 (m, 26H), 1.15 (d, 18H), 0.97 (t, 3H), 0.90 (t, 3H)

After bromination, **5-Br** or **6-Br** is homocoupled with hexamethylditin by Stille coupling in the same manner reported in Chapters 2, 3 and 5. Purification by column chromatography (silica gel, hexanes) yielded the TIPS-protected dimers **7-Tips** and **8-Tips**, respectively. Finally, dimers **7** and **8** were synthesized by deprotection of **7-Tips** and **8-Tips** (1 eqv.) in a stirring THF solution with tetra-n-butylamonnium floride (TBAF, 1 M in THF) (~8 eqv.) for 4 hours. Final product was extracted with hexanes/water and purified in a short column (silica gel, hexanes). Note, the final product **7-Tips** was separable despite a dirty stille coupling from impure **5-Br** and any other cross coupling impurities as illustrated in part by Scheme 3. I also attempted deprotection of **5-Br** prior to dimerization

to see if this improve separation however, the deprotected **5-Br** and **3-Br** were also inseparable.

(7-Tips) TIPS-T4-TT-T12-T12-TT-T4-TIPS: ^{1}H NMR (500 MHz, $CDCL_3$, δ) 7.30 (s, 2H), 7.28 (s, 2H), 7.10 (s, 2H), 7.06 (s, 2H), 2.84 (m, 8H), 1.71 (m, 8H), 1.45 (m, 4H), 1.45-1.22 (m, 48H), 1.17 (d, 32H), 0.99 (t, 6H), 0.90 (t, 6H)

(8-Tips) TIPS-T12-TT-T4-T4-TT-T12-TIPS: ^{1}H NMR (500 MHz, $CDCL_3$, δ) 7.30 (s, 2H), 7.28 (s, 2H), 7.10 (s, 2H), 7.06 (s, 2H), 2.84 (m, 8H), 1.71 (m, 8H), 1.5-1.22 (m, 52H), 1.17 (d, 32H), 0.99 (t, 6H), 0.90 (t, 6H) MALDI: M/z 1366, Actual 1368 g/mol

(7) T4-TT-T12-T12-TT-T4: ^{1}H NMR (500 MHz, $CDCL_3$, δ) 7.28 (s, 2H), 7.27 (s, 2H), 7.25 (s, 2H), 7.06 (s, 2H), 7.00 (s, 2H), 2.82 (m, 8H), 1.70 (m, 8H), 1.43 (m, 8H), 1.4-1.22 (m, 28H), 0.99 (t, 6H), 0.90 (t, 6H) MALDI: M/z 1055, Actual 1056 g/mol

(8) T12-TT-T4-T4-TT-T12: ^{1}H NMR (500 MHz, $CDCL_3$, δ) 7.28 (s, 2H), 7.27 (s, 2H), 7.25 (s, 2H), 7.06 (s, 2H), 7.00 (s, 2H), 2.82 (m, 8H), 1.70 (m, 8H), 1.43 (m, 8H), 1.4-1.22 (m, 28H), 0.99 (t, 6H), 0.90 (t, 6H) MALDI: M/z 1055, Actual 1056 g/mol

Failed synthesis of 9 (BTTT-4-12-4-12), shown in Scheme 3.

The general strategy for synthesis of the asymmetric dimers is shown below in Scheme 3. Synthesis of the protected and brominated asymmetric BTTT monomers (**5** and **6**) enabled the best chance at adapting the synthetic scheme to difficulties encountered in purification. Through this method, I could leverage bromination, deprotection, or lithiation/stannylation to gain additional separation and purification enhancement. Additionally, the protected and brominated **5-Br** and **6-Br** molecules were required for synthesis of **7** (BTTT-**4-12-12-4)** and **8** (BTTT-**12-4-4-12**), so this synthetic approach provided the best flexibility and fewest synthetic steps to produce molecules **7**, **8**, and **9**. As previously mentioned, the starting material, **3** and its brominated or deprotected derivatives were impossible to separate from **5** and its brominated or deprotected

derivatives as illustrated in Scheme 3. Due to this difficulty, and the array of possible side products, **9** could not be purified.

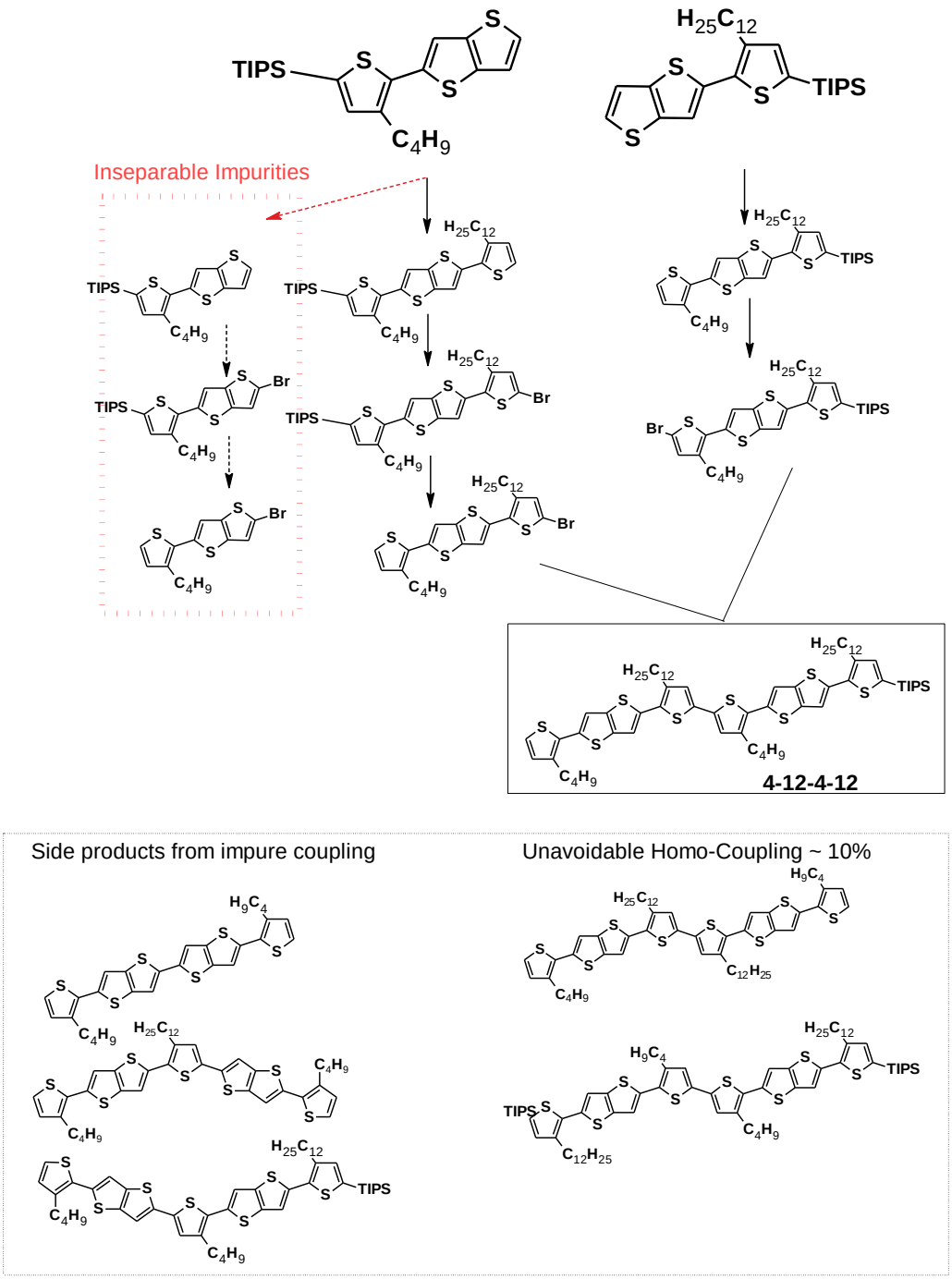

Scheme 3. Strategy for synthesis of molecule 9 (BTTT-4-12-4-12) and failure analysis.

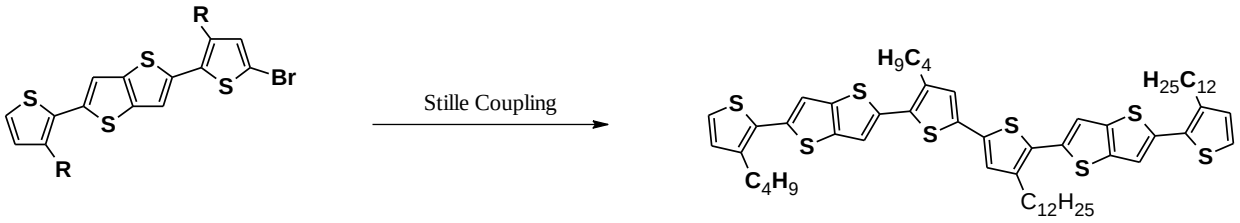

Scheme 4. Synthesis of variably substituted dimer, BTTT-4-4-12-12.
R = C4 or C12

Synthesis of BTTT-4-4-12-12

Synthesis of remaining dimer is described here. BTTT-**4-4-12-12** was synthesized through stille coupling of monobromo BTTT-**1-C4** and monobromo BTTT-**1-C12** with hexamethylditin. Hexamethylditin (1 eqv.), tetrakis(triphenylphosphine) palladium (0) (0.1 eqv.), anhydrous toluene, BTTT-**1-C12-Br** (1 eqv.) and BTTT-**1-C4-Br** (1 eqv.) are added to a dry round bottom flask with a reflux condenser. The reaction is degassed and heated to reflux overnight. After cooling, toluene is mostly removed in vacuo and hexanes is added forming a red precipitate. This mixture is heated, sonicated, and then gravity filtered and washed with hexanes. The red solid (used catalyst) is discarded. Skipping catalyst removal typically results in clogged column and material trapped in the solidified catalyst. The remaining solution is purified in column chromatography (silica, hexanes) and dried to yield an orange solid (bright yellow fluorescence on TLC); 60% yield. Note, homocoupled biproducts BTTT-**2-12** and BTTT-**2-4** are easily separable from the desired BTTT-**4-4-12-12** (middle fraction) in column chromatography.

Characterization: ^{1}H NMR, Bruker 500 MHz:
(8) T4-TT-T4-T12-TT-T12: ^{1}H NMR (500 MHz, $CDCL_3$, δ) 7.28 (s, 2H), 7.27 (s, 2H), 7.25 (s, 2H), 7.06 (s, 2H), 7.00 (s, 2H), 2.82 (m, 8H), 1.70 (m, 8H), 1.43 (m, 8H), 1.4-1.22 (m, 28H), 0.99 (t, 6H), 0.90 (t, 6H) MALDI: M/z 1055, Actual 1056 g/mol

APPENDIX C

BTTT-C12/DOPANT GIXD PATTERNS

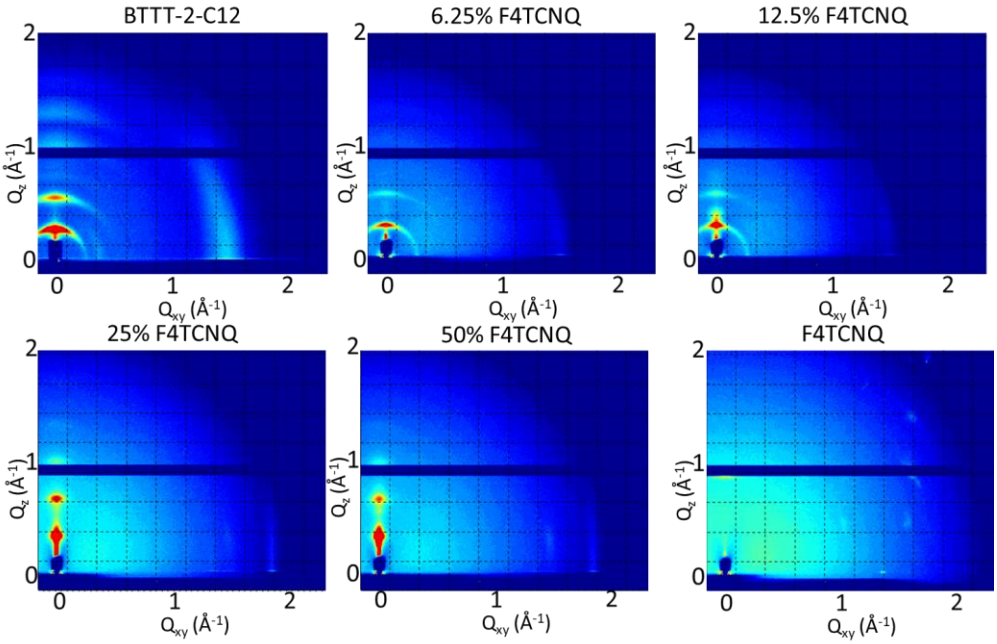

Figure 87 GIXD patterns of BTTT-C12 with increasing ratio of F4TCNQ dopant.

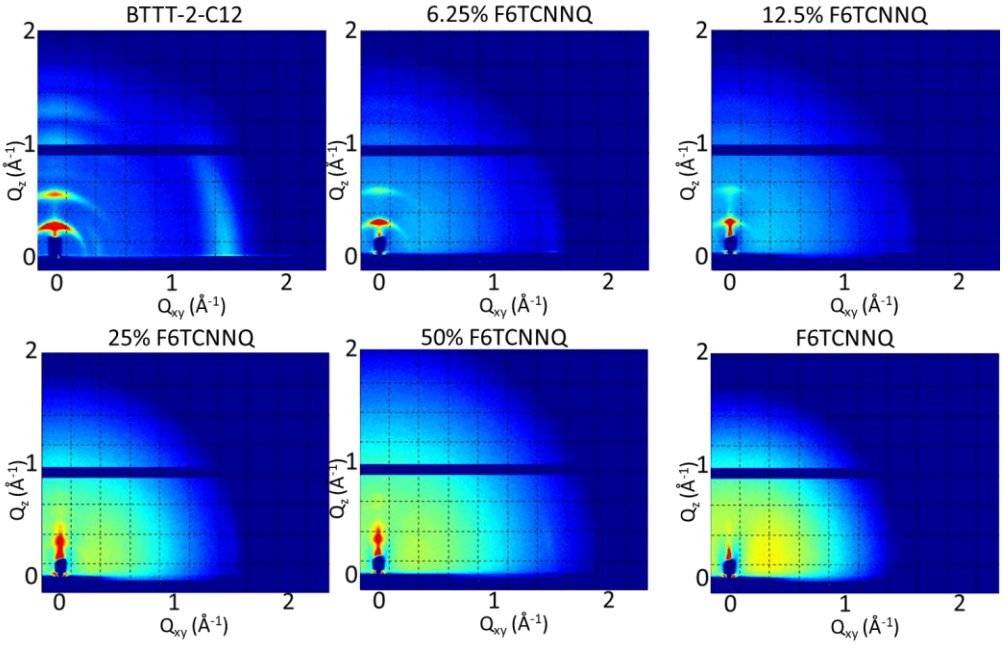

Figure 88 GIXD patterns of BTTT-C12 with increasing ratio of F6TCNNQ dopant.

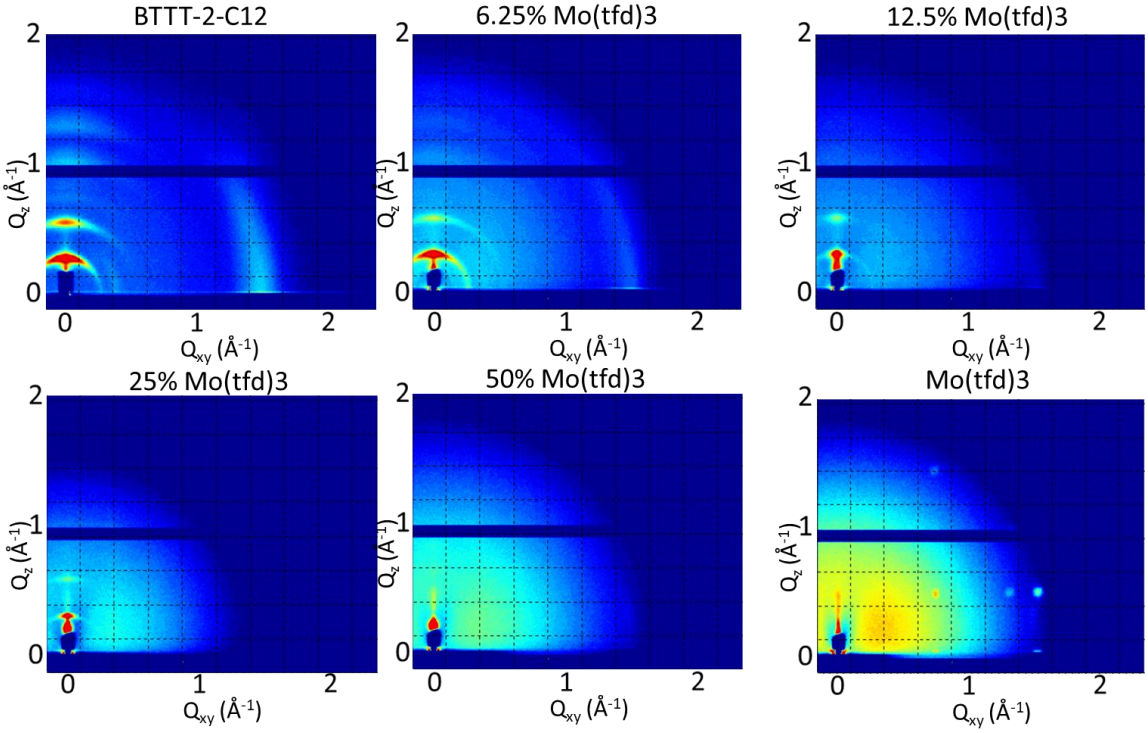

Figure 89 . GIXD patterns of BTTT-C12 with increasing ratio of $Mo(tfd)_3$ dopant.

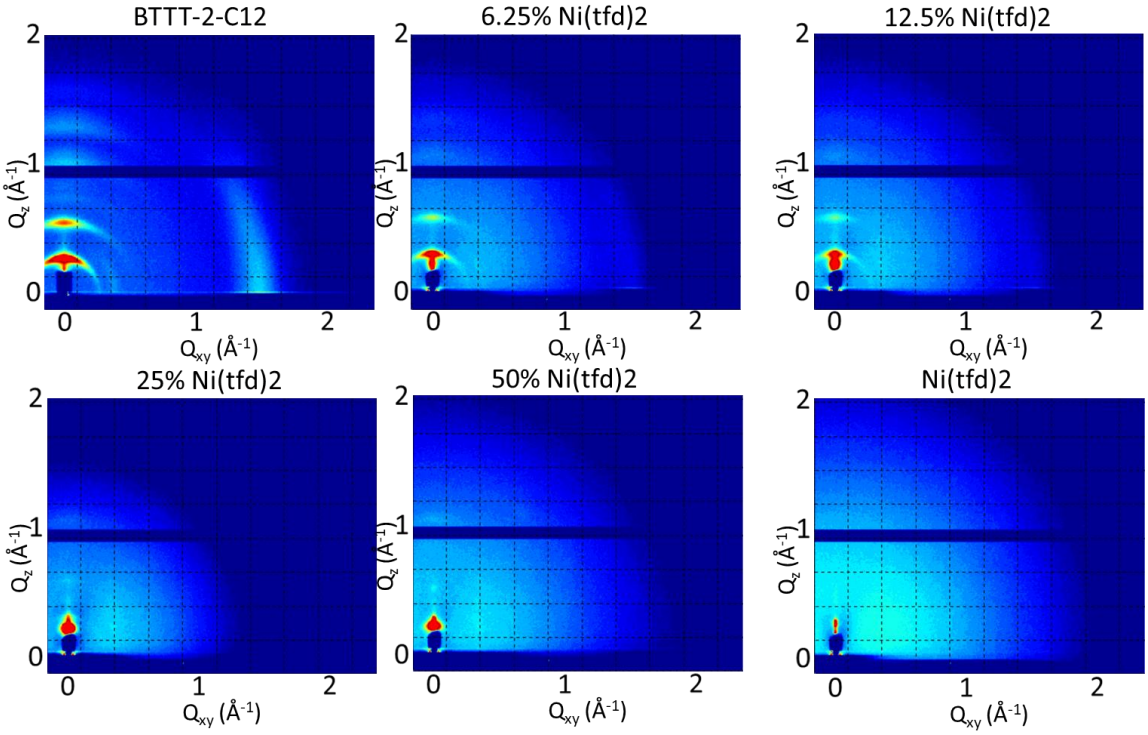

Figure 90 GIXD patterns of BTTT-C12 with increasing ratio of $Ni(tfd)_2$ dopant.

BIBLIOGRAPHY

1 Geffroy, B., Le Roy, P. & Prat, C. Organic light-emitting diode (OLED) technology: materials, devices and display technologies. *Polym. Int.* **55**, 572-582 (2006).

2 Dimitrakopoulos, C. D. in *Advanced Semiconductor and Organic Nano-Techniques* 191-240 (Elsevier, 2003).

3 Sirringhaus, H. Device physics of solution-processed organic field-effect transistors. *Adv. Mater.* **17**, 2411-2425 (2005).

4 Horowitz, G. Organic field-effect transistors. *Adv. Mater.* **10**, 365-377 (1998).

5 Günes, S., Neugebauer, H. & Sariciftci, N. S. Conjugated polymer-based organic solar cells. *Chem. Rev.* **107**, 1324-1338 (2007).

6 Thompson, B. C. & Fréchet, J. M. Polymer–fullerene composite solar cells. *Angew. Chem. Int. Ed.* **47**, 58-77 (2008).

7 Cao, W. & Xue, J. Recent progress in organic photovoltaics: device architecture and optical design. *Energy Environ. Sci.* **7**, 2123-2144 (2014).

8 Someya, T., Dodabalapur, A., Huang, J., See, K. C. & Katz, H. E. Chemical and physical sensing by organic field-effect transistors and related devices. *Adv. Mater.* **22**, 3799-3811 (2010).

9 Subramanian, V. *et al.* Progress toward development of all-printed RFID tags: materials, processes, and devices. *Proc. IEEE* **93**, 1330-1338 (2005).

10 Brédas, J.-L., Calbert, J. P., da Silva Filho, D. & Cornil, J. Organic semiconductors: A theoretical characterization of the basic parameters governing charge transport. *Proceedings of the National Academy of Sciences* **99**, 5804-5809 (2002).

11 Brédas, J.-L., Beljonne, D., Coropceanu, V. & Cornil, J. Charge-transfer and energy-transfer processes in π-conjugated oligomers and polymers: a molecular picture. *Chem. Rev.* **104**, 4971-5004 (2004).

12 Coropceanu, V. *et al.* Charge transport in organic semiconductors. *Chem. Rev.* **107**, 926-952 (2007).

13 Scott, J. C. & Malliaras, G. G. Charge injection and recombination at the metal–organic interface. *Chem. Phys. Lett.* **299**, 115-119 (1999).

14 Scott, J. C. Metal–organic interface and charge injection in organic electronic devices. *Journal of Vacuum Science & Technology A: Vacuum, Surfaces, and Films* **21**, 521-531 (2003).

15 Lemaur, V., Steel, M., Beljonne, D., Brédas, J.-L. & Cornil, J. Photoinduced charge generation and recombination dynamics in model donor/acceptor pairs for organic solar cell applications: a full quantum-chemical treatment. *J. Am. Chem. Soc.* **127**, 6077-6086 (2005).

16 Clarke, T. M. & Durrant, J. R. Charge photogeneration in organic solar cells. *Chem. Rev.* **110**, 6736-6767 (2010).

17 Liu, J. *et al.* Fast charge separation in a non-fullerene organic solar cell with a small driving force. *Nature Energy* **1**, 16089 (2016).

18 Bakulin, A. A. *et al.* The role of driving energy and delocalized states for charge separation in organic semiconductors. *Science* **335**, 1340-1344 (2012).

19 Holstein, T. Studies of polaron motion: Part I. The molecular-crystal model. *Annals of physics* **8**, 325-342 (1959).

20 Holstein, T. Studies of polaron motion: Part II. The “small” polaron. *Annals of physics* **8**, 343-389 (1959).

21 Marcus, R. A. Electron transfer reactions in chemistry. Theory and experiment. *Rev. Mod. Phys.* **65**, 599 (1993).

22 Warta, W. & Karl, N. Hot holes in naphthalene: High, electric-field-dependent mobilities. *Physical Review B* **32**, 1172 (1985).

23 Podzorov, V. *et al.* Intrinsic charge transport on the surface of organic semiconductors. *Phys. Rev. Lett.* **93**, 086602 (2004).

24 Podzorov, V., Menard, E., Rogers, J. & Gershenson, M. Hall effect in the accumulation layers on the surface of organic semiconductors. *Phys. Rev. Lett.* **95**, 226601 (2005).

25 Sirringhaus, H. *et al.* Two-dimensional charge transport in self-organized, high-mobility conjugated polymers. *Nature* **401**, 685 (1999).

26 Blom, P., De Jong, M. & Van Munster, M. Electric-field and temperature dependence of the hole mobility in poly (p-phenylene vinylene). *Physical Review B* **55**, R656 (1997).

27 Geng, H. *et al.* Toward quantitative prediction of charge mobility in organic semiconductors: tunneling enabled hopping model. *Adv. Mater.* **24**, 3568-3572 (2012).

28 Fratini, S., Mayou, D. & Ciuchi, S. The transient localization scenario for charge transport in crystalline organic materials. *Adv. Funct. Mater.* **26**, 2292-2315 (2016).

29 Chung, H. & Diao, Y. Polymorphism as an emerging design strategy for high performance organic electronics. *J. Mater. Chem. C.* **4**, 3915-3933, doi:10.1039/c5tc04390e (2016).

30 Sze, S. M. *Semiconductor devices: physics and technology*. (John Wiley & Sons, 2008).
31 Dodabalapur, A., Torsi, L. & Katz, H. Organic transistors: two-dimensional transport and improved electrical characteristics. *Science* **268**, 270-271 (1995).

32 Masetti, G., Severi, M. & Solmi, S. Modeling of carrier mobility against carrier concentration in arsenic-, phosphorus-, and boron-doped silicon. *IEEE Trans. Electron Devices* **30**, 764-769 (1983).

33 Spear, W. & Le Comber, P. Substitutional doping of amorphous silicon. *Solid State Commun.* **17**, 1193-1196 (1975).

34 Yamamoto, Y., Yoshino, K. & Inuishi, Y. Electrical properties of phthalocyanine-halogen complexes. *J. Phys. Soc. Jpn.* **47**, 1887-1891 (1979).

35 Parthasarathy, G., Shen, C., Kahn, A. & Forrest, S. Lithium doping of semiconducting organic charge transport materials. *J. Appl. Phys.* **89**, 4986-4992 (2001).

36 Kido, J. & Matsumoto, T. Bright organic electroluminescent devices having a metal-doped electron-injecting layer. *Appl. Phys. Lett.* **73**, 2866-2868 (1998).

37 Walzer, K., Maennig, B., Pfeiffer, M. & Leo, K. Highly efficient organic devices based on electrically doped transport layers. *Chem. Rev.* **107**, 1233-1271 (2007).

38 Lüssem, B., Riede, M. & Leo, K. Doping of organic semiconductors. *physica status solidi (a)* **210**, 9-43 (2013).

39 Salzmann, I., Heimel, G., Oehzelt, M., Winkler, S. & Koch, N. Molecular electrical doping of organic semiconductors: fundamental mechanisms and emerging dopant design rules. *Acc. Chem. Res.* **49**, 370-378 (2016).

40 Jacobs, I. E. & Moulé, A. J. Controlling Molecular Doping in Organic Semiconductors. *Adv. Mater.* (2017).

41 Pingel, P. & Neher, D. Comprehensive picture of p-type doping of P3HT with the molecular acceptor F 4 TCNQ. *Physical Review B* **87**, 115209 (2013).

42 Duong, D. T., Wang, C., Antono, E., Toney, M. F. & Salleo, A. The chemical and structural origin of efficient p-type doping in P3HT. *Org. Electron.* **14**, 1330-1336 (2013).

43 Gao, W. & Kahn, A. Controlled p doping of the hole-transport molecular material N, N'-diphenyl-N, N'-bis (1-naphthyl)-1, 1'-biphenyl-4, 4'-diamine with tetrafluorotetracyanoquinodimethane. *J. Appl. Phys.* **94**, 359-366 (2003).

44 Pingel, P. *et al.* Charge-transfer localization in molecularly doped thiophene-based donor polymers. *The Journal of Physical Chemistry Letters* **1**, 2037-2041 (2010).

45 Karpov, Y. *et al.* High Conductivity in Molecularly p-Doped Diketopyrrolopyrrole-Based Polymer: The Impact of a High Dopant Strength and Good Structural Order. *Adv. Mater.* **28**, 6003-6010 (2016).

46 Zhang, F. & Kahn, A. Investigation of the High Electron Affinity Molecular Dopant F6-TCNNQ for Hole-Transport Materials. *Adv. Funct. Mater.* **28** (2018).

47 Yim, K. H. *et al.* Controlling Electrical Properties of Conjugated Polymers via a Solution-Based p-Type Doping. *Adv. Mater.* **20**, 3319-3324 (2008).

48 Salzmann, I. & Heimel, G. Toward a comprehensive understanding of molecular doping organic semiconductors. *J. Electron. Spectrosc. Relat. Phenom.* **204**, 208-222 (2015).

49 Méndez, H. *et al.* Charge-transfer crystallites as molecular electrical dopants. *Nat. Commun.* **6**, 8560 (2015).

50 Salzmann, I. *et al.* Intermolecular hybridization governs molecular electrical doping. *Phys. Rev. Lett.* **108**, 035502 (2012).

51 Méndez, H. *et al.* Doping of organic semiconductors: impact of dopant strength and electronic coupling. *Angew. Chem. Int. Ed.* **52**, 7751-7755 (2013).

52 Yang, J. *et al.* Molecular Structure-Dependent Charge Injection and Doping Efficiencies of Organic Semiconductors: Impact of Side Chain Substitution. *Advanced Materials Interfaces* **1** (2014).

53 Zanon, I. & Pecile, C. Vibronic structure of the near-infrared and visible electronic transitions of 7, 7, 8, 8-tetracyanoquinodimethane radical anion. *The Journal of Physical Chemistry* **87**, 3657-3664 (1983).

54 Meneghetti, M. & Pecile, C. Charge–transfer organic crystals: Molecular vibrations and spectroscopic effects of electron–molecular vibration coupling of the strong electron acceptor TCNQF4. *The Journal of chemical physics* **84**, 4149-4162 (1986).

55 Burnett, E. K. *et al.* Bistetracene Thin Film Polymorphic Control to Unravel the Effect of Molecular Packing on Charge Transport. *Advanced Materials Interfaces* **5**, 1701607 (2018).

56 Burnett, E. K. *et al.* Breaking the Bimolecular Crystal: The Effect of Side-Chain Length on Oligothiophene/Fullerene Intercalation. *Chem. Mater.* **30**, 2550-2556 (2018).

57 Mas-Torrent, M. & Rovira, C. Role of molecular order and solid-state structure in organic field-effect transistors. *Chem. Rev.* **111**, 4833-4856 (2011).

58 Brédas, J.-L., Calbert, J. P., da Silva Filho, D. & Cornil, J. Organic semiconductors: A theoretical characterization of the basic parameters governing charge transport. *Proc. Natl. Acad. Sci. USA* **99**, 5804-5809 (2002).

59 Cornil, J., Calbert, J. P., Beljonne, D., Silbey, R. & Bredas, J. Interchain interactions in π-conjugated oligomers and polymers: a primer. *Synth. Met.* **119**, 1-6 (2001).

60 Sheraw, C. D., Jackson, T. N., Eaton, D. L. & Anthony, J. E. Functionalized pentacene active layer organic thin-film transistors. *Adv. Mater.* **15**, 2009-2011 (2003).

61 Müller, T. J. & Bunz, U. H. *Functional organic materials: syntheses, strategies and applications*. (John Wiley & Sons, 2007).

62 Diao, Y. *et al.* Solution coating of large-area organic semiconductor thin films with aligned single-crystalline domains. *Nat. Mater.* **12**, 665-671, doi:10.1038/nmat3650 (2013).

63 Giri, G. *et al.* One-dimensional self-confinement promotes polymorph selection in large-area organic semiconductor thin films. *Nat. Commun.* **5** (2014).

64 Giri, G. *et al.* Tuning charge transport in solution-sheared organic semiconductors using lattice strain. *Nature* **480**, 504-508 (2011).

65 He, T. *et al.* Single-crystal field-effect transistors of new Cl2-NDI polymorph processed by sublimation in air. *Nat. Commun.* **6** (2015).

66 Matsukawa, T. *et al.* Polymorphs of Rubrene Crystal Grown from Solution. *Jpn. J. Appl. Phys.* **49**, 085502 (2010).

67 Mattheus, C. C. *et al.* Identification of polymorphs of pentacene. *Synth. Met.* **138**, 475-481 (2003).

68 Diao, Y. *et al.* Understanding polymorphism in organic semiconductor thin films through nanoconfinement. *J. Am. Chem. Soc.* **136**, 17046-17057 (2014).

69 Purdum, G. E. *et al.* Understanding Polymorph Transformations in Core-Chlorinated Naphthalene Diimides and their Impact on Thin-Film Transistor Performance. *Adv. Funct. Mater.* **26**, 2357-2364 (2016).

70 Hiszpanski, A. M. *et al.* Tuning Polymorphism and Orientation in Organic Semiconductor Thin Films via Post-deposition Processing. *J. Am. Chem. Soc.* **136**, 15749-15756, doi:10.1021/ja5091035 (2014).

71 Hiszpanski, A. M. & Loo, Y.-L. Directing the film structure of organic semiconductors via post-deposition processing for transistor and solar cell applications. *Energy Environ. Sci.* **7**, 592-608 (2014).

72 Jurchescu, O. D. *et al.* Effects of polymorphism on charge transport in organic semiconductors. *Phys. Rev. B* **80**, 085201 (2009).

73 Fritz, S. E., Martin, S. M., Frisbie, C. D., Ward, M. D. & Toney, M. F. Structural characterization of a pentacene monolayer on an amorphous SiO2 substrate with grazing incidence X-ray diffraction. *J. Am. Chem. Soc.* **126**, 4084-4085 (2004).

74 Mannsfeld, S. C., Virkar, A., Reese, C., Toney, M. F. & Bao, Z. Precise structure of pentacene monolayers on amorphous silicon oxide and relation to charge transport. *Adv. Mater.* **21**, 2294-2298 (2009).

75 Mattheus, C. C., de Wijs, G. A., de Groot, R. A. & Palstra, T. T. Modeling the polymorphism of pentacene. *J. Am. Chem. Soc.* **125**, 6323-6330 (2003).

76 Okamoto, T. *et al.* V-Shaped Organic Semiconductors With Solution Processability, High Mobility, and High Thermal Durability. *Adv. Mater.* **25**, 6392-6397 (2013).

77 Pho, T. V. *et al.* N-alkyldinaphthocarbazoles, azaheptacenes, for solution-processed organic field-effect transistors. *J. Am. Chem. Soc.* **134**, 18185-18188 (2012).

78 Zhang, L. *et al.* Bistetracene: an air-stable, high-mobility organic semiconductor with extended conjugation. *J. Am. Chem. Soc.* **136**, 9248-9251 (2014).

79 Dickey, K. C., Anthony, J. E. & Loo, Y. L. Improving Organic Thin-Film Transistor Performance through Solvent-Vapor Annealing of Solution-Processable Triethylsilylethynyl Anthradithiophene. *Adv. Mater.* **18**, 1721-1726, doi:10.1002/adma.200600188 (2006).

80 Lee, W. H. *et al.* Change of molecular ordering in soluble acenes via solvent annealing and its effect on field-effect mobility. *Appl. Phys. Lett.* **91**, 092105, doi:10.1063/1.2768885 (2007).

81 Ullah Khan, H. *et al.* Solvent Vapor Annealing in the Molecular Regime Drastically Improves Carrier Transport in Small-Molecule Thin-Film Transistors. *ACS Appl. Mater. Interfaces* **5**, 2325-2330, doi:10.1021/am3025195 (2013).

82 Yu, L. *et al.* Programmable and coherent crystallization of semiconductors. *Science Advances* **3**, e1602462 (2017).

83 Mannsfeld, S. C., Tang, M. L. & Bao, Z. Thin film structure of triisopropylsilylethynyl-functionalized pentacene and tetraceno [2, 3-b] thiophene from grazing incidence X-Ray diffraction. *Adv. Mater.* **23**, 127-131 (2011).

84 Amassian, A., Pozdin, V. A., Li, R., Smilgies, D.-M. & Malliaras, G. G. Solvent vapor annealing of an insoluble molecular semiconductor. *J. Mater. Chem.* **20**, 2623-2629, doi:10.1039/b923375j (2010).

85 Ahmed, M. O. *et al.* Thieno [3, 2-b] thiophene oligomers and their applications as p-type organic semiconductors. *J. Mater. Chem.* **19**, 3449-3456 (2009).

86 Lee, W. H. *et al.* Room-Temperature Self-Organizing Characteristics of Soluble Acene Field-Effect Transistors. *Adv. Funct. Mater.* **18**, 560-565 (2008).

87 Kim, J. Y., Yasuda, T., Yang, Y. S., Matsumoto, N. & Adachi, C. Polymorphism in 9, 9-diarylfluorene-based organic semiconductors: influence on optoelectronic functions. *Chem. Commun.* **50**, 1523-1526 (2014).

88 Lee, H. *et al.* Rubicene: a molecular fragment of C 70 for use in organic field-effect transistors. *J. Mater. Chem. C.* **2**, 3361-3366 (2014).

89 Rivnay, J. *et al.* Large modulation of carrier transport by grain-boundary molecular packing and microstructure in organic thin films. *Nat. Mater.* **8**, 952-958 (2009).

90 Sundar, V. C. *et al.* Elastomeric transistor stamps: reversible probing of charge transport in organic crystals. *Science* **303**, 1644-1646 (2004).

91 Sele, C. W. *et al.* Controlled deposition of highly ordered soluble acene thin films: effect of morphology and crystal orientation on transistor performance. *Adv. Mater.* **21**, 4926-4931 (2009).

92 Li, R. *et al.* Micrometer-Sized Organic Single Crystals, Anisotropic Transport, and Field-Effect Transistors of a Fused-Ring Thienoacene. *Adv. Mater.* **21**, 4492-4495 (2009).

93 Lee, M. J. *et al.* Anisotropy of Charge Transport in a Uniaxially Aligned and Chain-Extended, High-Mobility, Conjugated Polymer Semiconductor. *Adv. Funct. Mater.* **21**, 932-940 (2011).

94 Reese, C. & Bao, Z. High-Resolution Measurement of the Anisotropy of Charge Transport in Single Crystals. *Adv. Mater.* **19**, 4535-4538 (2007).

95 Jimison, L. H., Toney, M. F., McCulloch, I., Heeney, M. & Salleo, A. Charge-Transport Anisotropy Due to Grain Boundaries in Directionally Crystallized Thin Films of Regioregular Poly (3-hexylthiophene). *Adv. Mater.* **21**, 1568-1572 (2009).

96 Headrick, R. L., Wo, S., Sansoz, F. & Anthony, J. E. Anisotropic mobility in large grain size solution processed organic semiconductor thin films. *Appl. Phys. Lett.* **92**, 063302, doi:10.1063/1.2839394 (2008).

97 Yu, L. *et al.* Solution-processed small molecule transistors with low operating voltages and high grain-boundary anisotropy. *J. Mater. Chem.* **22**, 9458-9461 (2012).

98 Wade, J. *et al.* Charge mobility anisotropy of functionalized pentacenes in organic field effect transistors fabricated by solution processing. *J. Mater. Chem. C.* **2**, 10110-10115 (2014).

99 Sirringhaus, H., Sakanoue, T. & Chang, J.-F. Charge-transport physics of high-mobility molecular semiconductors. *Phys. Status Solidi B* **249**, 1655-1676, doi:10.1002/pssb.201248143 (2012).

100 Meneau, A. Y. *et al.* Temperature Dependence of Charge Localization in High-Mobility, Solution-Crystallized Small Molecule Semiconductors Studied by Charge Modulation Spectroscopy. *Adv. Funct. Mater.* (2015).

101 Chirvase, D. *et al.* Temperature dependent characteristics of poly (3 hexylthiophene)-fullerene based heterojunction organic solar cells. *J. Appl. Phys.* **93**, 3376-3383 (2003).

102 Terao, S. *et al.* Temperature-dependent carrier mobility and threshold voltage of field-effect transistors with tetracene single crystals. *J. Appl. Phys.* **108**, 124511 (2010).

103 Minder, N. A., Ono, S., Chen, Z., Facchetti, A. & Morpurgo, A. F. Band-Like Electron Transport in Organic Transistors and Implication of the Molecular Structure for Performance Optimization. *Adv. Mater.* **24**, 503-508 (2012).

104 Pfattner, R. *et al.* High-Performance Single Crystal Organic Field-Effect Transistors Based on Two Dithiophene-Tetrathiafulvalene (DT-TTF) Polymorphs. *Adv. Mater.* **22**, 4198-4203 (2010).

105 Sakanoue, T. & Sirringhaus, H. Band-like temperature dependence of mobility in a solution-processed organic semiconductor. *Nat. Mater.* **9**, 736-740 (2010).

106 Xu, X. *et al.* Electron Mobility Exceeding 10 cm2 V− 1 s− 1 and Band-Like Charge Transport in Solution-Processed n-Channel Organic Thin-Film Transistors. *Adv. Mater.* **28**, 5276-5283 (2016).

107 Yamashita, Y. *et al.* Mobility Exceeding 10 cm2/(V· s) in Donor–Acceptor Polymer Transistors with Band-like Charge Transport. *Chem. Mater.* **28**, 420-424 (2016).

108 Paterson, A. F. *et al.* Small molecule/polymer blend organic transistors with hole mobility exceeding 13 cm2 V− 1 s− 1. *Adv. Mater.* **28**, 7791-7798 (2016).

109 Zhou, H. *et al.* Polymer homo-tandem solar cells with best efficiency of 11.3%. *Adv. Mater.* **27**, 1767-1773 (2015).

110 Zhao, W. *et al.* Molecular optimization enables over 13% efficiency in organic solar cells. *J. Am. Chem. Soc.* **139**, 7148-7151 (2017).

111 Bin, H. *et al.* 11.4% Efficiency non-fullerene polymer solar cells with trialkylsilyl substituted 2D-conjugated polymer as donor. *Nat. Commun.* **7**, 13651 (2016).

112 Yang, Y. *et al.* Side-chain isomerization on an n-type organic semiconductor ITIC acceptor makes 11.77% high efficiency polymer solar cells. *J. Am. Chem. Soc.* **138**, 15011-15018 (2016).

113 Mei, J. & Bao, Z. Side chain engineering in solution-processable conjugated polymers. *Chem. Mater.* **26**, 604-615 (2013).

114 Zhou, Y. *et al.* High performance all-polymer solar cell via polymer side-chain engineering. *Adv. Mater.* **26**, 3767-3772 (2014).

115 Fang, L. *et al.* Side-chain engineering of isoindigo-containing conjugated polymers using polystyrene for high-performance bulk heterojunction solar cells. *Chem. Mater.* **25**, 4874-4880 (2013).

116 Mei, J., Kim, D. H., Ayzner, A. L., Toney, M. F. & Bao, Z. Siloxane-terminated solubilizing side chains: bringing conjugated polymer backbones closer and boosting hole mobilities in thin-film transistors. *J. Am. Chem. Soc.* **133**, 20130-20133 (2011).

117 Park, Y. D. *et al.* Effect of side chain length on molecular ordering and field-effect mobility in poly (3-alkylthiophene) transistors. *Org. Electron.* **7**, 514-520 (2006).

118 Gadisa, A. *et al.* Effect of Alkyl Side-Chain Length on Photovoltaic Properties of Poly (3-alkylthiophene)/PCBM Bulk Heterojunctions. *Adv. Funct. Mater.* **19**, 3300-3306 (2009).

119 Chu, T. Y. *et al.* Effects of the molecular weight and the side-chain length on the photovoltaic performance of dithienosilole/thienopyrrolodione copolymers. *Adv. Funct. Mater.* **22**, 2345-2351 (2012).

120 Zhang, L., Colella, N. S., Cherniawski, B. P., Mannsfeld, S. C. & Briseno, A. L. Oligothiophene semiconductors: synthesis, characterization, and applications for organic devices. *ACS Appl. Mater. Interfaces* **6**, 5327-5343 (2014).

121 Murphy, A. R. & Frechet, J. M. Organic semiconducting oligomers for use in thin film transistors. *Chem. Rev.* **107**, 1066-1096 (2007).

122 Mishra, A., Ma, C.-Q. & Bauerle, P. Functional oligothiophenes: molecular design for multidimensional nanoarchitectures and their applications. *Chem. Rev.* **109**, 1141-1276 (2009).

123 Mena-Osteritz, E. *et al.* Two-Dimensional Crystals of Poly (3-Alkyl-thiophene) s: Direct Visualization of Polymer Folds in Submolecular Resolution. *Angew. Chem.* **112**, 2791-2796 (2000).

124 Izumi, T., Kobashi, S., Takimiya, K., Aso, Y. & Otsubo, T. Synthesis and spectroscopic properties of a series of β-blocked long oligothiophenes up to the 96-mer: Revaluation of effective conjugation length. *J. Am. Chem. Soc.* **125**, 5286-5287 (2003).

125 Zhang, L. *et al.* Synthesis, electronic structure, molecular packing/morphology evolution, and carrier mobilities of pure oligo-/poly (alkylthiophenes). *J. Am. Chem. Soc.* **135**, 844-854 (2012).

126 Zhang, L. *et al.* The good host: formation of discrete one-dimensional fullerene "channels" in well-ordered Poly (2, 5-bis (3-alkylthiophen-2-yl) thieno [3, 2-b] thiophene) oligomers. *J. Am. Chem. Soc.* **136**, 18120-18130 (2014).

127 Cherniawski, B. P. *et al.* The effect of hexyl side chains on molecular conformations, crystal packing, and charge transport of oligothiophenes. *J. Mater. Chem. C.* **5**, 582-588 (2017).

128 Boese, R., Weiss, H. C. & Bläser, D. The Melting point alternation in the short-chain n-alkanes: single-crystal x-ray analyses of propane at 30 K and of n-butane to n-nonane at 90 K. *Angew. Chem. Int. Ed.* **38**, 988-992 (1999).

129 Thalladi, V. R., Nüsse, M. & Boese, R. The melting point alternation in α, ω-alkanedicarboxylic acids. *J. Am. Chem. Soc.* **122**, 9227-9236 (2000).

130 Thalladi, V. R., Boese, R. & Weiss, H. C. The Melting Point Alternation in α, ω-Alkanediols and α, ω-Alkanediamines: Interplay between Hydrogen Bonding and Hydrophobic Interactions. *Angew. Chem. Int. Ed.* **39**, 918-922 (2000).

131 Vishweshwar, P., Nangia, A. & Lynch, V. M. Molecular complexes of homologous alkanedicarboxylic acids with isonicotinamide: X-ray crystal structures, hydrogen bond synthons, and melting point alternation. *Crystal growth & design* **3**, 783-790 (2003).

132 Bond, A. D. On the crystal structures and melting point alternation of the n-alkyl carboxylic acids. *New J. Chem.* **28**, 104-114 (2004).

133 Thalladi, V. R., Boese, R. & Weiss, H.-C. The melting point alternation in α, ω-alkanedithiols. *J. Am. Chem. Soc.* **122**, 1186-1190 (2000).

134 Tao, F. & Bernasek, S. L. Understanding odd− even effects in organic self-assembled monolayers. *Chem. Rev.* **107**, 1408-1453 (2007).

135 Heister, K. *et al.* Odd− Even Effects at the S-Metal Interface and in the Aromatic Matrix of Biphenyl-Substituted Alkanethiol Self-Assembled Monolayers. *The Journal of Physical Chemistry B* **105**, 6888-6894 (2001).

136 Thuo, M. M. *et al.* Odd− even effects in charge transport across self-assembled monolayers. *J. Am. Chem. Soc.* **133**, 2962-2975 (2011).

137 Stoliar, P. *et al.* Charge injection across self-assembly monolayers in organic field-effect transistors: Odd− even effects. *J. Am. Chem. Soc.* **129**, 6477-6484 (2007).

138 Akkerman, H. B. *et al.* Effects of Odd–Even Side Chain Length of Alkyl-Substituted Diphenylbithiophenes on First Monolayer Thin Film Packing Structure. *J. Am. Chem. Soc.* **135**, 11006-11014 (2013).

139 de la Rama, L. P., Hu, L., Ye, Z., Efremov, M. Y. & Allen, L. H. Size Effect and Odd–Even Alternation in the Melting of Single and Stacked AgSC n Layers: Synthesis and Nanocalorimetry Measurements. *J. Am. Chem. Soc.* **135**, 14286-14298 (2013).

140 Ebata, H. *et al.* Highly soluble [1] benzothieno [3, 2-b] benzothiophene (BTBT) derivatives for high-performance, solution-processed organic field-effect transistors. *J. Am. Chem. Soc.* **129**, 15732-15733 (2007).

141 Lee, B. & Richards, F. M. The interpretation of protein structures: estimation of static accessibility. *J. Mol. Biol.* **55**, 379-IN374 (1971).

142 Hanson, R. M. Jmol–a paradigm shift in crystallographic visualization. *J. Appl. Crystallogr.* **43**, 1250-1260 (2010).

143 Hoppe, H. & Sariciftci, N. S. Morphology of polymer/fullerene bulk heterojunction solar cells. *J. Mater. Chem.* **16**, 45-61 (2006).

144 Liu, Y. *et al.* Aggregation and morphology control enables multiple cases of high-efficiency polymer solar cells. *Nat. Commun.* **5** (2014).

145 Chen, L. M., Hong, Z., Li, G. & Yang, Y. Recent progress in polymer solar cells: manipulation of polymer: fullerene morphology and the formation of efficient inverted polymer solar cells. *Adv. Mater.* **21**, 1434-1449 (2009).

146 Benanti, T. L. & Venkataraman, D. Organic solar cells: An overview focusing on active layer morphology. *Photosynth. Res.* **87**, 73-81 (2006).

147 Collins, B. A. *et al.* Absolute measurement of domain composition and nanoscale size distribution explains performance in PTB7: PC71BM solar cells. *Advanced Energy Materials* **3**, 65-74 (2013).

148 Yan, H. *et al.* Correlating the efficiency and nanomorphology of polymer blend solar cells utilizing resonant soft X-ray scattering. *Acs Nano* **6**, 677-688 (2011).

149 Yu, G., Gao, J., Hummelen, J. C., Wudl, F. & Heeger, A. J. Polymer photovoltiac cells: Enhanced efficiencies via a network of internal donor-acceptor heterojunctions. *Science* **270**, 1789 (1995).

150 Dennler, G., Scharber, M. C. & Brabec, C. J. Polymer-Fullerene bulk-heterojunction solar cells. *Adv. Mater.* **21**, 1323-1338 (2009).

151 Kozub, D. R. *et al.* Polymer crystallization of partially miscible polythiophene/fullerene mixtures controls morphology. *Macromolecules* **44**, 5722-5726 (2011).

152 Collins, B. A. *et al.* Molecular miscibility of polymer− fullerene blends. *The Journal of Physical Chemistry Letters* **1**, 3160-3166 (2010).

153 Yin, W. & Dadmun, M. A new model for the morphology of P3HT/PCBM organic photovoltaics from small-angle neutron scattering: rivers and streams. *Acs Nano* **5**, 4756-4768 (2011).

154 Treat, N. D. *et al.* Interdiffusion of PCBM and P3HT reveals miscibility in a photovoltaically active blend. *Advanced Energy Materials* **1**, 82-89 (2011).

155 Chen, D., Nakahara, A., Wei, D., Nordlund, D. & Russell, T. P. P3HT/PCBM bulk heterojunction organic photovoltaics: correlating efficiency and morphology. *Nano Lett.* **11**, 561-567 (2010).

156 Mayer, A. *et al.* Bimolecular crystals of fullerenes in conjugated polymers and the implications of molecular mixing for solar cells. *Adv. Funct. Mater.* **19**, 1173-1179 (2009).

157 Cates, N. C. *et al.* Tuning the properties of polymer bulk heterojunction solar cells by adjusting fullerene size to control intercalation. *Nano Lett.* (2009).

158 Cates, N. C., Gysel, R., Dahl, J. E., Sellinger, A. & McGehee, M. D. Effects of intercalation on the hole mobility of amorphous semiconducting polymer blends. *Chem. Mater.* **22**, 3543-3548 (2010).

159 Miller, N. C. *et al.* Factors governing intercalation of fullerenes and other small molecules between the side chains of semiconducting polymers used in solar cells. *Advanced Energy Materials* **2**, 1208-1217 (2012).

160 Miller, N. C. *et al.* Use of X-Ray Diffraction, Molecular Simulations, and Spectroscopy to Determine the Molecular Packing in a Polymer-Fullerene Bimolecular Crystal. *Adv. Mater.* **24**, 6071-6079 (2012).

161 Miller, N. C. *et al.* The phase behavior of a polymer-fullerene bulk heterojunction system that contains bimolecular crystals. *J. Polym. Sci., Part B: Polym. Phys.* **49**, 499-503 (2011).

162 Miller, N. C. *et al.* Molecular packing and solar cell performance in blends of polymers with a bisadduct fullerene. *Nano Lett.* **12**, 1566-1570 (2012).

163 Rance, W. L. *et al.* Photoinduced carrier generation and decay dynamics in intercalated and non-intercalated polymer: fullerene bulk heterojunctions. *Acs Nano* **5**, 5635-5646 (2011).

164 Savenije, T. J. *et al.* Photoinduced charge carrier generation in blends of poly (thienothiophene) derivatives and [6, 6]-phenyl-C61-butyric acid methyl ester: phase segregation versus intercalation. *The Journal of Physical Chemistry C* **114**, 15116-15120 (2010).

165 Scarongella, M. *et al.* A close look at charge generation in polymer: fullerene blends with microstructure control. *J. Am. Chem. Soc.* **137**, 2908-2918 (2015).

166 Buchaca-Domingo, E. *et al.* Additive-assisted supramolecular manipulation of polymer: fullerene blend phase morphologies and its influence on photophysical processes. *Materials Horizons* **1**, 270-279 (2014).

167 Buchaca-Domingo, E. *et al.* Direct correlation of charge transfer absorption with molecular donor: acceptor interfacial area via photothermal deflection spectroscopy. *J. Am. Chem. Soc.* **137**, 5256-5259 (2015).

168 De Jonghe-Risse, J. *et al.* The fate of electron–hole pairs in polymer: fullerene blends for organic photovoltaics. *Nat. Commun.* **7**, 12556 (2016).

169 Kang, K. *et al.* 2D coherent charge transport in highly ordered conducting polymers doped by solid state diffusion. *Nat. Mater.* (2016).

170 Cherniawski, B. P. *et al.* The effect of hexyl side chains on molecular conformations, crystal packing, and charge transport of oligothiophenes. *J. Mater. Chem. C.* (2017).

171 Chabinyc, M. L., Toney, M. F., Kline, R. J., McCulloch, I. & Heeney, M. X-ray scattering study of thin films of poly (2, 5-bis (3-alkylthiophen-2-yl) thieno [3, 2-b] thiophene). *J. Am. Chem. Soc.* **129**, 3226-3237 (2007).

172 McCulloch, I. *et al.* Liquid-crystalline semiconducting polymers with high charge-carrier mobility. *Nat. Mater.* **5**, 328-333 (2006).

173 Koppe, M. *et al.* Polyterthiophenes as donors for polymer solar cells. *Adv. Funct. Mater.* **17**, 1371-1376 (2007).

174 Hoppe, H. *et al.* Nanoscale morphology of conjugated polymer/fullerene-based bulk-heterojunction solar cells. *Adv. Funct. Mater.* **14**, 1005-1011 (2004).

175 Yu, G. & Heeger, A. J. Charge separation and photovoltaic conversion in polymer composites with internal donor/acceptor heterojunctions. *J. Appl. Phys.* **78**, 4510-4515 (1995).

176 Marsh, H. S. & Jayaraman, A. Effect of side chain length on the morphology of blends of 2, 5-bis (3-alkylthiophen-2-yl) thieno [3, 2-b] thiophene oligomers and fullerene derivatives. *J. Polym. Sci., Part B: Polym. Phys.* **54**, 89-97 (2016).

177 Baran, D. *et al.* Reduced voltage losses yield 10% efficient fullerene free organic solar cells with> 1 V open circuit voltages. *Energy Environ. Sci.* **9**, 3783-3793 (2016).

178 Gao, X. & Zhao, Z. High mobility organic semiconductors for field-effect transistors. *Science China Chemistry* **58**, 947-968 (2015).

179 Sun, B., Hong, W., Yan, Z., Aziz, H. & Li, Y. Record high electron mobility of 6.3 cm2V− 1s− 1 achieved for polymer semiconductors using a new building block. *Adv. Mater.* **26**, 2636-2642 (2014).

180 Tseng, H. R. *et al.* High-Mobility Field-Effect Transistors Fabricated with Macroscopic Aligned Semiconducting Polymers. *Adv. Mater.* **26**, 2993-2998 (2014).

181 Uoyama, H., Goushi, K., Shizu, K., Nomura, H. & Adachi, C. Highly efficient organic light-emitting diodes from delayed fluorescence. *Nature* **492**, 234 (2012).

182 Han, T.-H. *et al.* Extremely efficient flexible organic light-emitting diodes with modified graphene anode. *Nature Photonics* **6**, 105 (2012).

183 Zhang, Q. *et al.* Efficient blue organic light-emitting diodes employing thermally activated delayed fluorescence. *Nature Photonics* **8**, 326 (2014).

184 Diao, Y., Shaw, L., Bao, Z. & Mannsfeld, S. C. Morphology control strategies for solution-processed organic semiconductor thin films. *Energy Environ. Sci.* **7**, 2145-2159 (2014).

185 Tsao, H. N. & Müllen, K. Improving polymer transistor performance via morphology control. *Chem. Soc. Rev.* **39**, 2372-2386 (2010).

186 Liu, Y. *et al.* Aggregation and morphology control enables multiple cases of high-efficiency polymer solar cells. *Nat. Commun.* **5**, 5293 (2014).

187 Liu, T. *et al.* Alkyl Side-Chain Engineering in Wide-Bandgap Copolymers Leading to Power Conversion Efficiencies over 10%. *Adv. Mater.* **29** (2017).

188 Zhang, Z.-G. & Li, Y. Side-chain engineering of high-efficiency conjugated polymer photovoltaic materials. *Science China Chemistry* **58**, 192-209 (2015).

189 Li, Z. *et al.* Side-Chain Engineering for Enhancing the Thermal Stability of Polymer Solar Cells. *Adv. Mater.* **27**, 6999-7003 (2015).

190 Cates, N. C. *et al.* Tuning the properties of polymer bulk heterojunction solar cells by adjusting fullerene size to control intercalation. *Nano Lett.*, 4153-4157 (2009).

191 Paterno, G., Skoda, M., Dalgliesh, R., Cacialli, F. & Sakai, V. G. Tuning Fullerene Intercalation in a Poly (thiophene) derivative by Controlling the Polymer Degree of Self-Organisation. *Sci. Rep.* **6**, 34609 (2016).

192 Zhang, W. *et al.* Correlation between morphology and device performance of pBTTT: PC 71 BM solar cells. *Sol. Energy Mater. Sol. Cells* **155**, 387-396 (2016).

193 Schlitz, R. A. *et al.* Solubility-Limited Extrinsic n-Type Doping of a High Electron Mobility Polymer for Thermoelectric Applications. *Adv. Mater.* **26**, 2825-2830 (2014).

194 Wei, P., Oh, J. H., Dong, G. & Bao, Z. Use of a 1 H-benzoimidazole derivative as an n-type dopant and to enable air-stable solution-processed n-channel organic thin-film transistors. *J. Am. Chem. Soc.* **132**, 8852-8853 (2010).

195 Wei, P. *et al.* 2-(2-Methoxyphenyl)-1, 3-dimethyl-1 H-benzoimidazol-3-ium iodide as a new air-stable n-type dopant for vacuum-processed organic semiconductor thin films. *J. Am. Chem. Soc.* **134**, 3999-4002 (2012).

196 Rossbauer, S., Müller, C. & Anthopoulos, T. D. Comparative Study of the N-Type Doping Efficiency in Solution-processed Fullerenes and Fullerene Derivatives. *Adv. Funct. Mater.* **24**, 7116-7124 (2014).

197 Glaudell, A. M., Cochran, J. E., Patel, S. N. & Chabinyc, M. L. Impact of the doping method on conductivity and thermopower in semiconducting polythiophenes. *Advanced Energy Materials* **5** (2015).

198 Cochran, J. E. *et al.* Molecular interactions and ordering in electrically doped polymers: blends of PBTTT and F4TCNQ. *Macromolecules* **47**, 6836-6846 (2014).

199 Jacobs, I. E. *et al.* Comparison of solution-mixed and sequentially processed P3HT: F4TCNQ films: effect of doping-induced aggregation on film morphology. *J. Mater. Chem. C.* **4**, 3454-3466 (2016).

200 Gao, J. *et al.* The effect of 2, 3, 5, 6-tetrafluoro-7, 7, 8, 8-tetracyanoquinodimethane charge transfer dopants on the conformation and aggregation of poly (3-hexylthiophene). *J. Mater. Chem. C.* **1**, 5638-5646 (2013).

201 Li, J. *et al.* The effect of thermal annealing on dopant site choice in conjugated polymers. *Org. Electron.* **33**, 23-31 (2016).

202 Scholes, D. T. *et al.* Overcoming film quality issues for conjugated polymers doped with F4TCNQ by solution sequential processing: Hall effect, structural, and optical measurements. *The Journal of Physical Chemistry Letters* **6**, 4786-4793 (2015).

203 Hynynen, J. *et al.* Enhanced Electrical Conductivity of Molecularly p-Doped Poly (3-hexylthiophene) through Understanding the Correlation with Solid-State Order. *Macromolecules* **50**, 8140-8148 (2017).

204 Kroon, R. *et al.* Polar Side Chains Enhance Processability, Electrical Conductivity, and Thermal Stability of a Molecularly p-Doped Polythiophene. *Adv. Mater.* **29** (2017).

205 Liu, J. *et al.* Enhancing Molecular n-Type Doping of Donor–Acceptor Copolymers by Tailoring Side Chains. *Adv. Mater.* (2018).

206 Kiefer, D. *et al.* Enhanced n-Doping Efficiency of a Naphthalenediimide-Based Copolymer through Polar Side Chains for Organic Thermoelectrics. *ACS Energy Letters* **3**, 278-285 (2018).

207 Liu, J. *et al.* N-Type Organic Thermoelectrics: Improved Power Factor by Tailoring Host–Dopant Miscibility. *Adv. Mater.* **29** (2017).

208 Li, H. *et al.* Modification of the Poly (bisdodecylquaterthiophene) Structure for High and Predominantly Nonionic Conductivity with Matched Dopants. *J. Am. Chem. Soc.* **139**, 11149-11157 (2017).

209 Qi, Y. *et al.* Use of a high electron-affinity molybdenum dithiolene complex to p-dope hole-transport layers. *J. Am. Chem. Soc.* **131**, 12530-12531 (2009).

210 Qi, Y. *et al.* A molybdenum dithiolene complex as p-dopant for hole-transport materials: a multitechnique experimental and theoretical investigation. *Chem. Mater.* **22**, 524-531 (2009).

211 Dai, A. *et al.* Enhanced charge-carrier injection and collection via lamination of doped polymer layers p-doped with a solution-processible molybdenum complex. *Adv. Funct. Mater.* **24**, 2197-2204 (2014).

212 Cheng, X. *et al.* Transition between triangular and square tiling patterns in liquid-crystalline honeycombs formed by tetrathiophene-based bolaamphiphiles. *Chemical Science* **4**, 3317-3331, doi:10.1039/c3sc50664a (2013).

213 Bruker, A. APEX2-Software Suite for Crystallographic Programs. *Bruker AXS Inc., Madison* (2009).

214 Krause, L., Herbst-Irmer, R., Sheldrick, G. M. & Stalke, D. Comparison of silver and molybdenum microfocus X-ray sources for single-crystal structure determination. *Journal of Applied Crystallography* **48**, 3-10, doi:doi:10.1107/S1600576714022985 (2015).

215 Sheldrick, G. M. SHELXT: Integrating space group determination and structure solution. *Acta Crystallogr. Sect. A* **70**, C1437 (2014).

216 Sheldrick, G. M. Crystal structure refinement with SHELXL. *Acta Crystallographica Section C: Structural Chemistry* **71**, 3-8 (2015).

217 Parkin, S. Expansion of scalar validation criteria to three dimensions: the R tensor. *Acta Crystallographica Section A: Foundations of Crystallography* **56**, 157-162 (2000).

218 Spek, A. L. Structure validation in chemical crystallography. *Acta Crystallographica Section D: Biological Crystallography* **65**, 148-155 (2009).

219 Kopsky, V. & Litvin, D. B. *International tables for crystallography*. (John Wiley, 2010).